Didem TEKGÜN

A Ph.D. Thesis

AGU 2022

SYSTEMATIC DESIGN OPTIMIZATION AND IMPLEMENTATION OF LINE START SYNCHRONOUS RELUCTANCE MACHINE FOR DOWN HOLE SUBMERSIBLE WATER PUMP APPLICATIONS

A THESIS
SUBMITTED TO THE DEPARTMENT OF ELECTRICAL AND COMPUTER ENGINEERING
AND THE GRADUATE SCHOOL OF ENGINEERING AND SCIENCE OF ABDULLAH GUL UNIVERSITY
IN PARTIAL FULFILLMENT OF THE REQUIREMENTS
FOR THE DEGREE OF
DOCTOR OF PHILOSOPHY

By
Didem TEKGÜN
November 2022

SYSTEMATIC DESIGN OPTIMIZATION AND IMPLEMENTATION OF LINE START SYNCHRONOUS RELUCTANCE MACHINE FOR DOWN HOLE SUBMERSIBLE WATER PUMP APPLICATIONS

A THESIS
SUBMITTED TO THE DEPARTMENT OF ELECTRICAL AND COMPUTER ENGINEERING
AND THE GRADUATE SCHOOL OF ENGINEERING AND SCIENCE OF
ABDULLAH GUL UNIVERSITY
IN PARTIAL FULFILLMENT OF THE REQUIREMENTS
FOR THE DEGREE OF
DOCTOR OF PHILOSOPHY

By
Didem TEKGÜN
November 2022

SCIENTIFIC ETHICS COMPLIANCE

I hereby declare that all information in this document has been obtained in accordance with academic rules and ethical conduct. I also declare that, as required by these rules and conduct, I have fully cited and referenced all materials and results that are not original to this work.

Name-Surname: Didem TEKGÜN
Signature :

REGULATORY COMPLIANCE

Ph.D. thesis titled ‘Systematic Design Optimization and Implementation of Line Start Synchronous Reluctance Machines for Down Hole Submersible Water Pump Applications’ has been prepared in accordance with the Thesis Writing Guidelines of the Abdullah Gül University, Graduate School of Engineering & Science.

Prepared By	Advisor
Didem TEKGÜN	Prof. Dr. İrfan ALAN
Signature	Signature

Head of the Electrical and Computer Engineering Program

Assoc. Prof. Zafer AYDIN

Signature

ACCEPTANCE AND APPROVAL

Ph.D. thesis titled Systematic Design Optimization and Implementation of Line Start Synchronous Reluctance Machines for Down Hole Submersible Water Pump Applications and prepared by Didem TEKGÜN has been accepted by the jury in the Electrical and Computer Engineering Graduate Program at Abdullah Gül University, Graduate School of Engineering & Science.

22/12/2022

(Thesis Defense Exam Date)

JURY:

Advisor : Prof. İrfan ALAN………………………………………………………………

Member : Prof. Erkan MEŞE…………………………………………………………….

Member : Doç. Dr. Günyaz ABLAY……………………………………………...........

Member : Prof. Dr. Murat BARUT………………………………………………………

Member : Dr. Öğr. Üyesi Selçuk GÖREN..

APPROVAL:

The acceptance of this Ph.D. thesis has been approved by the decision of the Abdullah Gül University, Graduate School of Engineering & Science, Executive Board dated ….. /….. / 2022 and numbered …………..……. .

……….. /……….. / ………..

(Date)

Graduate School Dean
Prof. Dr. İrfan ALAN

ABSTRACT

SYSTEMATIC DESIGN OPTIMIZATION AND IMPLEMENTATION OF LINE START SYNCHRONOUS RELUCTANCE MACHINE FOR DOWN HOLE SUBMERSIBLE WATER PUMP APPLICATIONS

Didem TEKGÜN
Ph.D. in Electrical and Computer Engineering
Advisor: Prof. Dr. İrfan ALAN

November 2022

Considering the electric drive systems constitute roughly 40% of global energy production, improving electric machine efficiencies provides important nationwide and global scale advantages. Among the electric motors used in the industry, a major portion of them is pump motors used for pumping underground waters and petroleum products. Especially the motors for submersible pump applications run at very low-efficiency levels because of motor design issues and the wrong selection of motor-pump configurations. Due to the features like robustness, low cost, and line start capability, induction machines (IM) are generally the first choice for pump applications. However, IMs work with low efficiency, especially at low and medium power levels. Line start synchronous reluctance machines (LS-SynRM) come to the scene as a reasonable alternative by having the line start capability and not having rare earth permanent magnets as well. The working principle of these machines is a combination of a reluctance machine and an IM. In LS-SynRM, a rotor cage is inserted in the rotor for the machine to start with the line voltage, but the rotor copper losses become zero when the machine operates at synchronous speed. Moreover, SynRMs have higher power and torque density. In this thesis study, it is aimed to reduce the overall cost of the submersible water pump system by designing and optimizing an LS-SynRM as a submersible pump motor with higher efficiency compared to conventional IMs. Increasing the efficiency of the pump motor used in industry will improve the overall system performance. Accordingly, it lowers energy and maintenance costs, and easy process control will be achieved. This way, while reducing energy consumption nationwide significantly, not only the natural resources will be protected, but also huge amounts of money will be saved.

Keywords: Submersible pump motor, synchronous reluctance motor, differential evolution, line start

ÖZET

SU ALTI DALGIÇ POMPA UYGULAMALARI İÇİN DOĞRUDAN YOL VERMELİ RELÜKTANS MOTORUNUN SİSTEMATİK OLARAK TASARIM OPTİMİZASYONU VE GERÇEKLEMESİ

Didem TEKGÜN
Elektrik ve Bilgisayar Mühendisliği Ana Bilim Dalı Doktora
Tez Yöneticisi: Prof. Dr. İrfan ALAN

Kasım-2022

Elektrik tahrik sistemlerinin küresel enerji tüketiminin yaklaşık %40’ını oluşturduğu düşünüldüğünde elektrik makinalarının verimlerinin artırılması ile sağlanacak avantajların hem ülke bazında hem de evrensel olarak büyük bir öneme sahip olduğu görülmektedir. Uygulama odaklı olarak bakıldığında yer altından su, petrol vb. çıkarmakta kullanılan pompa motorlarının endüstride kullanılmakta olan motorlar arasında oldukça büyük bir paya sahip olduğu görülmektedir. Özellikle dalgıç pompa uygulamalarında kullanılmakta olan pompa motorları motor tasarımı sırasında oluşan hatalar nedeniyle çok düşük verimlerle çalışmaktadır. Sağlamlık, ucuzluk ve doğrudan yol verme gibi özelliklerinden dolayı pompa uygulamalarında genellikle indüksiyon motorları (İM) tercih edilmektedir. Fakat İM’lerin en büyük sorunu özellikle küçük ve orta güçte düşük enerji verimi ile çalışmalarıdır. Bu doğrultuda hem doğrudan yol verme özelliği hem de mıknatıs içermeyen yapısı ile doğrudan yol vermeli senkron relüktans motorlar (DY-SenRM) İM’lere uygun bir alternatif olarak karşımıza çıkmaktadır. DY-SenRM’de makinanın rotoruna gömülen rotor barları ile doğrudan yol verme özelliği kazandırılırken, İM’lerin aksine rotor bakır kayıpları sürekli rejimde sıfıra indirilmektedir. Dahası yüksek güç ve moment yoğunluğuna sahiptir. Bu tez çalışmasında, dalgıç pompa motorları için verimi İM’lere kıyasla daha yüksek bir DY-SenRM tasarımı ve optimizasyonu yapılarak toplam sistem maliyetinin büyük oranda azaltılması amaçlanmıştır. Endüstride sıklıkla kullanılan bu pompa motorlarının verimindeki artış pompa sisteminin performansını önemli ölçüde artırarak, enerji maliyetini ve bakım masrafalarını düşürerek kolay bir kontrol sağlayacaktır. Böylece, ulusal çapta enerji tüketimi azaltılacak ve nadir mıknatıslar gibi doğal kaynaklarının korunması sağlanıyorken aynı zamanda maliyet ciddi oranda azalacaktır.

Anahtar kelimeler: Dalgıç pompa motoru, senkron relüktans motoru, diferansiyel evrim optimizasyonu, doğrudan yol verme

Acknowledgments

I wish to express my sincere gratitude to my adviser, Prof. Dr. İrfan Alan, for his guidance, support, technical help, understanding, and continuous encouragement throughout my doctoral study. His knowledge and managerial skills have been a source of inspiration throughout my research.

I am thankful to my professor and committee member, Prof. Dr. Erkan Meşe for his help and valuable opinions that certainly enriched my research during my studies. I am grateful to my professors and committee members, Assoc. Prof. Dr. Günyaz Ablay, Prof. Dr. Murat Barut, Assoc. Prof. Dr. Ahmet Önen and Asst. Prof. Dr. Selçuk Gören for their valuable comments and suggestions to improve the quality of the dissertation.

I would like to thank the Higher Education Board (YÖK) and The Scientific and Technological Research Council of Türkiye (TUBİTAK) since I have been supported financially as a government-funded researcher in renewable energy area by YÖK under the 100/2000 program and supported by TUBİTAK under 2211-C Ph.D. scholarship program as a distinguished researcher during my thesis study. I also thank AGÜ administration for providing qualified research infrastructure.

I also give my thanks to companies; YASA Teknoloji, Fimsa Makina, Ser Elektrikli Ev Aletleri, and Mutlusu Submersible Pumps & Motors for their support through the manufacturing process of my thesis study.

I would like to give a special thanks to my dear husband, Asst. Prof. Dr. Burak Tekgün for his great support, valuable suggestions, and endless motivation throughout my graduate studies. His technical and motivational skills have been a source of inspiration and will remain with me for my future career.

I would like to express my deepest love and gratitude to my parents for their faith in me. I owe all my success to my dear mother Zehra and her great orientation and endless support throughout my life.

Finally, and most importantly, I am grateful to my dear children, Selim Mete and Bilge Melis for bringing all the colors and joy to my life. This thesis would not have been possible without their love. They are the ones who motivated me by filling my life with happiness through all stages of my studies. I dedicated my work to them.

TABLE OF CONTENTS

LIST OF FIGURES

LIST OF TABLES

LIST OF ABBREVIATIONS

IM	Induction Machine
SynM	Synchronous Motor
SynRM	Synchronous Reluctance Motor
LS-SynM	Line-start Synchronous Motor
LS-SynRM	Line-start Synchronous Reluctance Motor
PF	Power Factor
LS-PMSM	Line-start Permanent Magnet Synchronous Motor
GA	Genetic Algorithm
MTPA	Maximum Torque Per Ampere
PM	Permanent Magnet
FEA	Finite Element Analysis
SMC	Soft Magnetic Composite
PSO	Particle Swarm Optimization
DE	Differential Evolution
RSA	Response Surface Analysis
MODE	Multi-Objective Differential Evolution
IPF	Internal Power Factor
MMF	Magneto-Motive Force
CFD	Computational Fluid Dynamics
PVC	Polyvinyl Chloride
1NF	First Natural Frequency
THD	Total Harmonic Distortion
FSCWs	Fractional-Slot Concentrated Windings
ML	Multi-Layer
EWS	End Winding Scores

To my family

Chapter 1

Introduction

All around the world, reducing energy consumption is the common goal for both protecting natural resources and saving a considerable amount of money. Due to global warming, sustainable and green motor technologies should be consumed consciously. Electrical motors and drive systems` energy consumption corresponds to between 35% and 40% of electrical energy production globally [1,2]. The demands of energy saving direct the machine designers' attention to finding compact and robust motors with high efficiency for constant speed applications, especially in the low and middle power ranges. Motors in this power range are mainly used for industrial, domestic, and irrigation water pumping systems. Induction machines (IMs) are the most used motor type in industrial applications due to their robustness and low cost. However, they suffer from very low-efficiency levels which will result in a waste of energy and natural resources [3]. Most specifically, the motors used for deep bore-well submersible pumps, which extract water from the ground, are in the range of low and middle power range. IMs are usually preferred as the submersible water pump's motor due to their line start capability and ruggedness besides the advantages given above. However, their efficiency is very low, especially in the submersible version.

Line-start Synchronous Motor (LS-SynM) is a strong alternative to traditional induction machines since they can start without any drive due to the addition of the cage inserted into the rotor core. Furthermore, rotor copper losses will be eliminated since the absence of rotor windings will lead to a significant reduction in the copper loss of the motor. Therefore, LS-SynMs can compete with the IMs in terms of low price and ruggedness while having higher efficiency [3].

Line-start Permanent Magnet Synchronous Motor (LS-PMSM) with different types of rotor structure is a typical solution to increase the efficiency of the motor compared to the IMs [4,5]. The LS-PMSM combines the advantages of robustness and line-start capability of IMs and high-power factor (PF), torque density, and therefore high efficiency of PM motors. However, PM motors have issues related to the demagnetization of magnets and motor synchronization capability. Furthermore, the use of rare-earth magnets can lead to higher power densities of electrical machines, but they are expensive and non-renewable natural resources, and their mining can lead to severe ecological damages if the required precautions are not properly taken [6]. Such drawbacks have oriented the attraction of researchers to consider magnet-free motor solutions.

A hybrid technology called Line-start Synchronous Reluctance Motor (LS-SynRM) combines the features of squirrel cage IM and synchronous reluctance motor (SynRM). LS-SynRM starts up with asynchronous torque from the rotor conductor bars and runs with the reluctance torque due to the flux barrier in synchronization. In synchronous operation, the induced current in rotor conductor bars is zero, and there is no conductor bar loss in the rotor which increase the overall performance. Furthermore, rotor copper losses will be eliminated since the absence of rotor windings will lead to a significant reduction in the copper loss of the motor. Therefore, compared to high-cost PMSM and low-efficiency IM, LS-SynRM is a reliable, highly efficient, and low-cost solution. However, it is a critical process that needs to be considered carefully both for asynchronous starting and steady-state performance. The possible problems such as the inability to synchronize, torque sag, and crawling effect are needed to be taken into consideration.

1.1 Problem Statement and Hypothesis

Research Question: What is the ideal submersible machine type, which is line start, lower loss, lower cost, lighter weight, higher torque, higher efficiency, more robust, more reliable, less rare earth magnet, and import-dependent?

Problem Statement: IM is usually preferred as the submersible pump motor due to its robustness, reliability, low cost, and line start capability. However, the efficiency of the IM is very low, especially in the submersible version. High torque, high efficiency, line start, PMSM solutions are available, but they lead to high cost and rare earth magnet dependency, besides the degradation of rare earth magnets might require magnet renewal or re-magnetizing.

Hypothesis: LS-SynRM is a strong alternative to the traditional induction machines since they have the capability to start without any drive due to the addition of the cage inserted into the rotor core, besides the rotor copper losses will be eliminated due to the absence of rotor windings which will lead to a significant reduction in the copper losses of the motor. Therefore, LS-SynRMs can compete with the IMs in terms of low price, ruggedness, and reliability while having higher efficiency. Additionally, LS-SynRMs get rid of high-cost and rare earth magnet dependency requirements and the degradation of rare earth magnets.

1.2 Research Motivation and Contributions

In most industries, since centrifugal pumps are the largest consumers of electric motor energy, the overall pump system has great potential for saving electrical energy [7]. Furthermore, a pump becomes a destructive force when it is considered that every watt of power is wasted by oversized or over-throttled pump sets which reduce overall pump performance and ruggedness. Achieving the triple benefit of low energy costs, low maintenance costs, and improved process control is possible by optimizing the pump motor.

Department of Energy (DOE) is stated that more than 13.5 million electric motors are used for industrial applications in the U.S. and more than $33 billion worth of electricity is dedicated to electric motors and drive systems annually. Improving the efficiency of existing motor systems will lead to significant nationwide cost savings since almost 70% of all electricity used in industry is consumed by some type of motor and drive system. Therefore, improvements in motor systems, as well as management of the process, can lead to significant energy savings of up to 42 % [7].

Although the IM is usually preferred as the submersible pump motor due to its robustness, reliability, low cost, and line start capability, it has very low efficiency, especially in the submersible version [3]. In addition to the poor efficiency of the motor, inappropriate usage of the pump set such as an oversized motor for the low and middle-range energy system, the wasted energy, and the cost of energy increase dramatically. According to studies in the literature, LS-PMSM is a viable solution to improve the efficiency of IMs used in industrial applications. However, they have problems such as demagnetization, synchronization disability, high cost, and import dependency due to rare-earth magnets. LS-SynRM is a strong alternative to the traditional induction machines since they have the capability to start without any drive due to the addition of the cage inserted into the rotor core, besides the rotor copper losses will be eliminated due to the absence of rotor windings which will lead to a significant reduction in the copper losses of the motor. Therefore, LS-SynRMs can compete with the IMs in terms of low price and ruggedness while having higher efficiency.

In this study, it is aimed to reduce the overall cost of the submersible water pump system by designing and optimizing a LS-SynRM as a submersible pump motor with higher efficiency compared to conventional IMs. Increasing the efficiency of the pump motor used in industry will improve the overall system performance. Accordingly, it will reduce energy and maintenance costs. This way, while reducing energy consumption nationwide significantly, not only the natural resources will be protected, but also an important amount of money will be saved. This is a crucial strategy for any facilities management that wants to improve the sustainability, productivity, and cost management of the facilities.

Chapter 2

Literature Review

2.1 Introduction

Today, reducing energy losses has become a common goal worldwide for preserving natural sources and reducing energy costs. Considering that electric drive systems constitute between 43% and 46% of the global energy consumption, improving electric machine efficiencies provides important nationwide and global scale advantages [8]. Among the electric motors used in the industry, a major portion belongs to pump motors used for pumping underground waters and petroleum products. Generally, the motors used in submersible pump applications run at very low-efficiency levels because of cost considerations, motor design issues, and wrong selection of motor-pump configurations. Due to the features like robustness, low cost, and line start capability, Induction Machines (IM) are generally the first choice for pump applications. However, the IMs operate with low efficiency, especially at low and medium power levels [9]. Permanent magnet synchronous machines (PMSM) are powerful rivals to the IM as they have higher power density and better efficiency compared to IM. However, their cost is several times higher than the same size IM and they require power electronics drives to operate. Although PMSM with drive systems are not preferred in submersible pump applications due to their cost, Line Start PMSM (LS-PMSM) can be found commercially as their initial cost is relatively lower due to the elimination of the drive cost. Nonetheless, problems like demagnetization during start-up through line voltage and having high costs and external dependence on rare earth elements lead researchers to find new alternatives to these motors.

Synchronous Reluctance Motors (SynRM) can also reach high-efficiency levels and they are another strong alternative to the IM. Yet they require a power electronic drive similar to the PMSM. Therefore, a hybrid technology called Line Start SynRM (LS-SynRM) that combines the features of squirrel cage IM and SynRM comes to the scene as a reasonable alternative to the IMs by having the line start capability and not having rare earth permanent magnets as well.

LS-SynRM starts as an IM due to the conductor bar structure inserted into the rotor. After reaching the synchronous speed, it runs as a SynRM merely relying on saliency torque that is due to the flux barriers on the rotor. While operating at synchronous speed, there would be no induced currents in rotor bars leading to zero loss at conductor bars. Besides, SynRMs have higher power and torque density compared to IMs [10]. Therefore, LS-SynRM is a very attractive alternative that is reliable, efficient, and low-cost compared to high-cost PMSM and low-efficiency IM. However, it is a fact that running the machine both in asynchronous and synchronous modes is a tedious process. The possible problems such as the inability to synchronize and crawling have to be investigated carefully.

2.2 Line Start Permanent Magnet Synchronous Motors

Line-start Permanent Magnet Synchronous Motor (LS-PMSM) with different types of rotor structure is a typical solution to increase the efficiency of the motor compared to the IMs [4,5]. The LS-PMSM combines the advantages of robustness and line-start capability of IMs and high-power factor (PF), torque density, and therefore high efficiency of PM motor. A 4-pole LS-PMSM is proposed for submersible water pumping applications in [11]. Since the rare-earth permanent magnet material is inserted into the rotor, the overall cost of the machine is increased. A high-performance, LS-PMSM is proposed for pumping application in [12]. It uses a 2-pole rotor geometry and the rotor cage is designed to find a minimum starting current. In [13], the curved shape PM with powder hybrid rotor is proposed and the analysis concluded that this rotor configuration has better efficiency and PF which is a good alternative for high-duty applications like fans, pumps, and compressors instead of IMs. In [14], a 2-pole LS-PMSM using NdFeB arc-shaped magnets is proposed. Two different rotor pole configurations; salient and non-salient poles are investigated and compared. It is shown that the reluctance torque obtained from the flux barriers is used to reduce the permanent magnet volume effectively and, the salient pole LS-PMSM can achieve both higher efficiency and PF in the steady-state operation. In [15], different rotor structures with various magnet configurations such as spoke type, V-magnets, W-magnets, U-magnets, radial magnets, and Swastik magnets are investigated. The spoke-type magnet rotor has better performance when compared with the other magnet configurations in terms of overall efficiency. Then in [16], magnets in different geometries such as arc magnet, rectangle magnet, and parallelogram magnet are integrated into the spoke-type magnet rotor for high power density. It is shown that the spoke-arc magnet rotor structure offers better power density compared to other combinations. In [17], a shaded-pole line-start PM synchronous motor as illustrated in Figure 2.1a is optimized using genetic algorithm (GA) method to improve starting capability, PF and efficiency and therefore reduce the cost of the machine. This study showed that shaded-pole LS-PMSM rotor losses is 34% less than the shaded-pole IM.

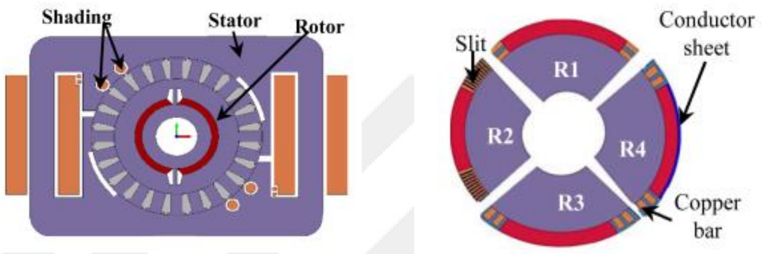

(a) **(b)**

Figure 2.1 (a) Shaded pole structure [3,17], (b) Copper bar, slit, and conductor sheet rotors [3,18]

In [18], starting capability and operation at a synchronous speed of a surface-mounted LS-PMSM with a slit structure are studied. Here, four different types of rotor configurations are analyzed shown in Figure 2.1b. Two pieces of copper bars are placed on each side of PMs at the first configuration. The second rotor design has one copper bar with several slits at each side of the PMs. In the third one, two parallel copper bars on each side of PMs are placed. The last design includes two parallel copper bars on each side of PMs with a conductor sheet on the surface of the PMs. The analysis results showed that the first three of them have synchronization problems whereas the last design with conductor sheet has both line start capability and runs at synchronous speed. Single-phase high-efficiency PM motors' advancements are introduced in [19]. Here, 2-pole rotor geometry is used and various factors that affect the performance of the single-phase interior PM motor drive systems are covered. A slotted solid rotor structure as in Figure 2.2a is studied and optimized for better start-up torque and capability of synchronization in [20]. The effect of rotor slots width and length of slotted rotor LS-PMSM are investigated for better torque development. A V-shaped magnet rotor (Figure 2.2b) that utilizes less active material to achieve an efficiency class of IE4 was proposed in [21] and it concluded that the starting performance of the proposed rotor design is close to NEMA standard design B.

(a) **(b)**

Figure 2.2 (a) The proposed motor with axial rotor slots [20], (b) V-shaped magnet with less active material [3,21]

Two different rotor configurations as in Figure 2.3a and 2.3b with magnets located near the squirrel cage to protect magnets from demagnetization and V-shape magnets rotor are proposed in [22]. The results confirmed that the inductance difference of the V-shaped magnet rotor configuration is larger which offers higher torque density.

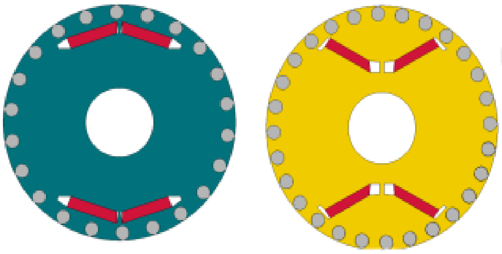

(a) **(b)**

Figure 2.3 (a) Magnet placed close to the cage, (b) V-shaped magnet [3,22]

In [23], a study carried out with three different rotor configurations of LS-PMSM as shown in Figures 2.4a, 2.4b, and 2.4c for efficiency improvement: First, two magnets are placed on the surface of the rotor in a radial direction, second in addition to the first one, two short magnets are included and in the last design, the magnets are introduced on the surface of the rotor teeth to reduce the magnetic flux leakage.

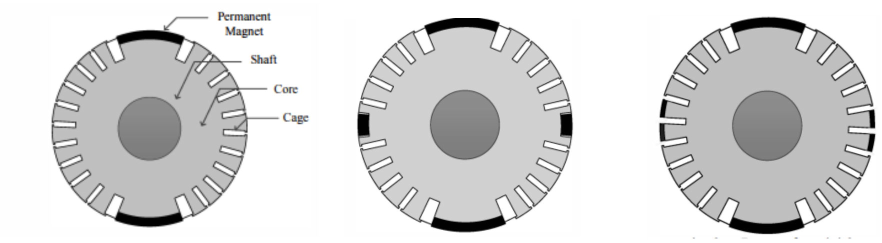

(a) **(b)** **(c)**

Figure 2.4 (a) Self-start PMSM rotor model 1, (b) model 2, (c) model 3 [23]

It is concluded that the second one is better than the first one and the third configuration has better performance in terms of output torque and efficiencies. A solid-rotor-based axial-flux LS-PMSM has been designed with a solid rotor structure in [24]. This structure offers auto-starting just like the induction machine through rotor rings. 6/8 pole changing LS-PMSM as shown in Figure 2.5 is proposed in [25] and it is concluded that the braking and pulsating torque of the developed LS-PMSM can be decreased in terms of fundamental, and the starting capability is improved effectively.

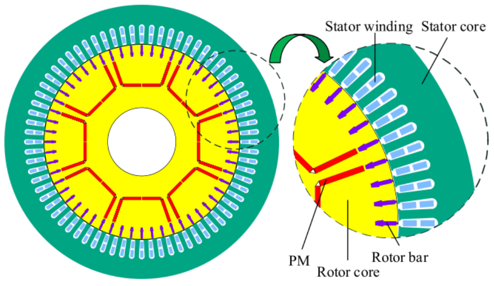

Figure 2.5 Split phase and pole changing rotor (6/8) [25]

In the literature, there exist several studies in terms of performance improvement by using different materials on the stator and rotor. A composite solid rotor design is proposed in [26,27] for improving the line start capability and synchronization of LS-PMSM. Since the rotor is composed of solid steel, a high starting torque is obtained accordingly. Aiming to improve the starting and synchronous performance of the LS-PMSM two different magnet configurations of the rotor with double cage bars are compared in [28]. The first configuration of the rotor has an inset magnet while the second design uses an induced magnet pole hybrid rotor (circumferentially and radially magnetized magnets) as shown in Figure 2.6a. The double cage inset magnet rotor has better starting capability than the hybrid rotor and the hybrid rotor has higher PF and efficiency with a 10% reduced magnet volume. Induced magnet pole LS-PMSM as shown in Figure 2.6b is presented in [29] which can be a viable alternative for standard LS-PMSM since the usage of PM is reduced to its half of the standard structure.

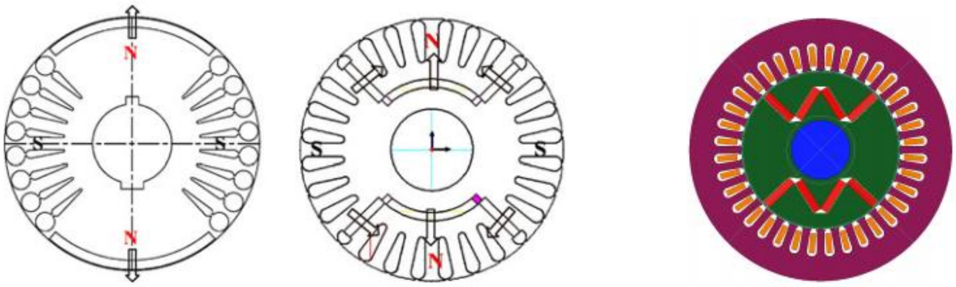

(a) (b)

Figure 2.6 **(a) Inset consequent magnet pole rotor with double cage and hybrid rotor with normal single cage [28], (b) Induced pole structure [29]**

Demagnetization of a single-phase LS-PMSM is investigated in [30] while considering the magnetic field produced by secondary conductor bars. In [31], a single-phase shaded pole LS-PMSM is designed. The design is constructed by keeping the stator the same as the shaded pole IM with the insertion of an alternative magnet. Another LS-PMSMs design is proposed in [4] to meet the high-efficiency class motor requirements. The study showed that the efficiency and PF of the proposed motor are higher compared with induction motors. However, manufacturing and the high cost of rare earth PMs are important drawbacks.

As a result, based on the studies mentioned above superiority of LS-PMSMs compared to IMs in terms of torque density, power factor, and therefore, overall efficiency cannot be underestimated. However, they have issues related to the demagnetization of magnets and motor synchronization capability. Furthermore, the use of rare-earth magnets can lead to higher power densities of electrical machines, but they are expensive and non-renewable natural resources, and their mining can lead to severe ecological damages if the required precautions are not properly taken [6]. Such drawbacks have oriented the attraction of researchers to consider magnet-free motor solutions.

2.3 Line Start Synchronous Reluctance Motors

Although the discovery of SynRM date back to 1923 [32], the first LS-SynRM rotor was designed in [33]. Here, 8 different rotor configurations are investigated and compared with each other and the IM. The rotor conductor bars execute starting torque while the flux barrier on the rotor is responsible for creating reluctance torque. It is concluded that under no load condition, the motor was running with lower efficiency and PF than the IM while under full load selected designs failed during testing. Some of the placement and shape of the conductor bars and flux barriers may cause unbalanced magnetic circuits which result in failed start-up and synchronization. In [34] and [35], starting performance of a single phase LS-SynRM is improved by optimizing the number and the shape of the conductor bars. In [3], a comprehensive review of technological advancements, design concepts, and some optimization techniques of LS-SynRMs are investigated. Here, a case study is carried out for a 4-pole LS-SynRM to decide if it is appropriate for agricultural applications in India instead of traditional IMs. Results showed that the energy consumption of the IM is 8.4% higher compared with LS-SynRM and 12.05% higher compared with LSPMSM. It is concluded that 6–12% of energy could be saved by replacing the higher efficiency and cost-effective LS-SynRM with IMs in the agricultural sector. Rotor design with round bars of a 4 pole 4-kW LS-SynRMs is introduced in [36] for high-efficiency industry applications, especially for constant-speed drives such as fan and pump applications. Additionally, rotor bar material/resistance and the stator resistance influence on the performance of the motor are studied using copper and aluminum cages. A benchmark study is carried out using the same sized (same stator) 4-kW IM. The number of the flux barrier is selected as 4 since this structure achieves a reasonable balance between the steady-state efficiency and the torque ripple. Flux barriers' shape is optimized using parametric sweep like optimization and the shape of hyperbolic function, as shown in Figure 2.7a, is selected as best fit to achieve the high efficiency. Two additional mechanical bridges for each flux barrier are inserted in the rotor's center (Figure 2.7b) to increase the mechanical strength.

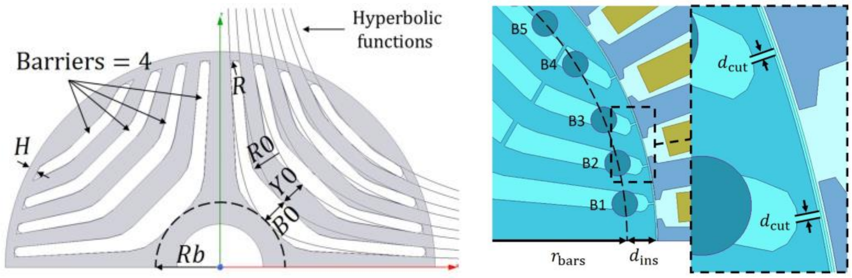

(a) **(b)**

Figure 2.7 (a) Rotor model, (b) Rotor bars and cutoff width in the end barrier region [36]

Further, the influence of the rotor bar’s diameter and their placements on overall motor losses and synchronization capability under different load conditions are investigated and for the selected bars, a cutoff at the end of each air barrier is introduced. The rotor losses, the stator leakage, and the eddy current losses in the bars are decreased with cutoffs. This study concludes that with an optimized hyperbolic flux barrier rotor design using copper rotor cage bars, efficiency, PF, and synchronization capability of the LS-SynRM are improved. The efficiency of the IM is increased from 89.3% to 93.0% using the proposed LS-SynRM while rotor loss is reduced by 28% of it. However, starting capability of IM is way better than the proposed machine. Therefore, the proposed LS-SynRM is suitable for some of the applications where the machines can be started under low load conditions such as conveyer belt fans and pump applications.

In [37], the influence of the design and optimization of rotor conductor bars on the parameters of a 2 pole 1.5 kW LS-SynRM is investigated. Additionally, the distribution of rotor conductor bars’ impact on the maximum torque and start-up torque of the motor is studied. The rotor bars distribution is analyzed and optimized to reduce the d-axis inductance weakening effect of the conductor bars. Performance comparison of the proposed design is done by using the same size and power IM. As a result, compared to the squirrel cage IM, the rated efficiency of the proposed LS-SynRM improved by 2.2%. Further, the simulation results are also verified experimentally and the test results showed that the proposed LS-SynRM’s efficiency is 2.3% higher than the conventional IM. A 2-pole, 5 HP multi-barrier LS-SynRM is proposed for a 6-inch bore-well submersible water pump [38]. Here, two different types of rotor structures are designed to have a high saliency ratio, therefore, reasonable current density. The flux barriers of both rotors are filled with Aluminum which acts as cage bars. Rotor-B has three flux barriers like the

Rotor-A with an additional cage inserted into the d-axis of the Rotor-B as shown in Figure 2.8. The analysis results showed that both rotor structures are capable of achieving a high saliency ratio. Since the additional cage inserted Rotor-B can be synchronized under five times the rotor inertia, the overload capacity of the machine is improved at the steady state, accordingly, the geometry of Rotor-B is appropriate for submersible water pump application.

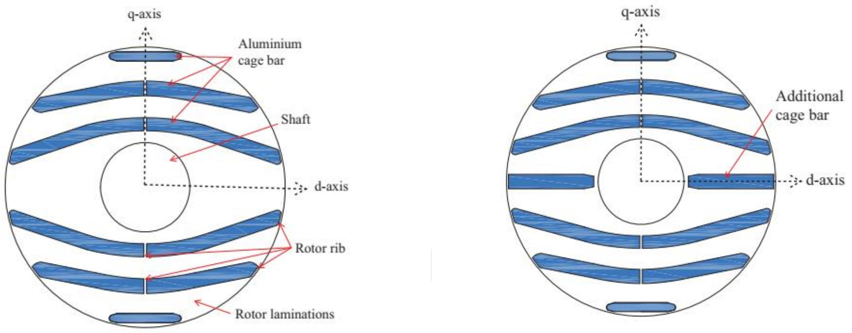

(a) **(b)**

Figure 2.8 (a) Rotor model A, (b) Rotor model B [38]

A 2 pole, 3 kW LS-SynRM with two different rotor flux barrier designs is proposed in [39] for fan and pump applications. In this study, the transient and steady-state performance of the 3 and 4 flux barrier rotor configurations are discussed and Finite Element Analysis (FEA) linked with an optimization algorithm showed that the 4-flux barrier rotor design has slightly better performance. Die-cast aluminum is used to fill some of the flux barriers as shown in Figure 2.9 to perform the line start feature. Further, the performance of the LS-SynRM with the selected design is compared with the same size and power IM. Analysis showed that the IE2 class IM with 85.9% efficiency is upgraded to IE4 class with 89.5% efficient LS-SynRM. In [40], a 2 pole, 3.7 kW multi-barrier line-start ferrite assisted synchronous reluctance motor is proposed for a 6 inches bore-well submersible water pump application. Similar to the studies mentioned above, the aim was a solution to replace an improved and efficient motor design instead of poor efficiency IMs. Here, it is stated that the magnetic saliency does not improve noticeably for the number of flux barriers greater than four. Hence, a four arc-shaped flux barrier ferrite-assisted rotor design as shown in Figure 2.10 is employed and a study that works on torque ripple minimization while maximizing the toque per ampere is proposed.

Figure 2.9 Cross section of the motor [39]

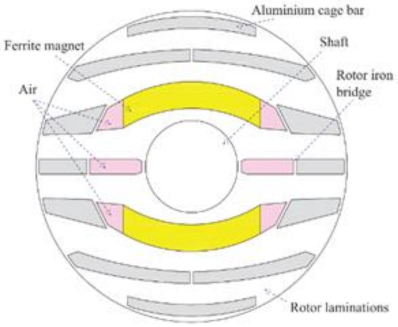

Figure 2.10 Cross section of the motor [40]

The reluctance torque is considered the main torque producer due to the flux barrier and the aim to use the ferrite magnets is to improve the PF with minimum magnet volume. The proposed motor is optimized using 2-D FE analysis in OptiNet software and the selected geometry of the rotor is optimized for reduced torque ripple and maximum torque per ampere (MTPA). Results showed that the motor efficiency is improved to IE4 standards. Shape and direction of rotor conductor bars' effect on parameters of a 2 pole 2 kW LS-SynRM while maximizing inductance difference (L_d-L_q) is proposed in [41]. Here, the conductor bars located at the q-axis are densely distributed to reduce the *q*-axis inductance (Figure 2.11a). Analysis results showed that the d-axis inductance is larger than the *q*-axis inductance of the LS-SynRM in this way. Then the model is improved to increase the inductance difference L_d-L_q by replacing the conductor as shown in Figure 2.11b.

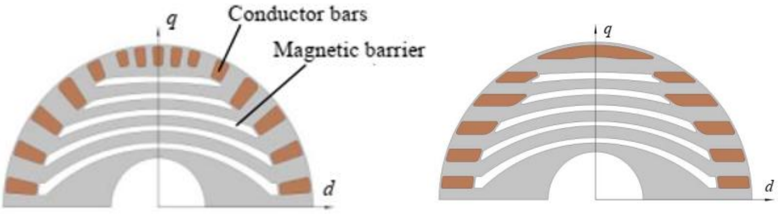

(a) **(b)**

Figure 2.11 (a) Traditional rotor model, (b) Improved rotor model [41]

The results show that the inductance difference between L_d and L_q of the improved LS-SynRM is increased by 1.4%, and the improved LS-SynRM has better start-up and overload capacity. It is concluded that the improved model's efficiency is better than IM by 1.82% with the same stator structure and power as the proposed LS-SynRM. In [42], a 4 pole 2.2 kW LS-SynRM with 3 different rotor configurations is proposed. These 3 concepts are analyzed and compared in terms of starting performance and synchronization capability. Then, the selected design is optimized using a parametric sweep and compared with the IM. The simulation and the test results under unloaded conditions showed that the higher torque ripple and lower power factor are obtained from the optimized LS-SynRM while its efficiency of it is slightly better than the IM. Due to an underestimation of the load inertia, the motor test under the full load has failed in synchronization, hence, no comparison is available for the full load condition. Another study of a single-phase LS-SynRM rotor design and optimization is presented in [2] to make a higher saliency ratio with a proper synchronizing ability. Here, three different rotor configurations as shown in Figure 2.12 are introduced and compared.

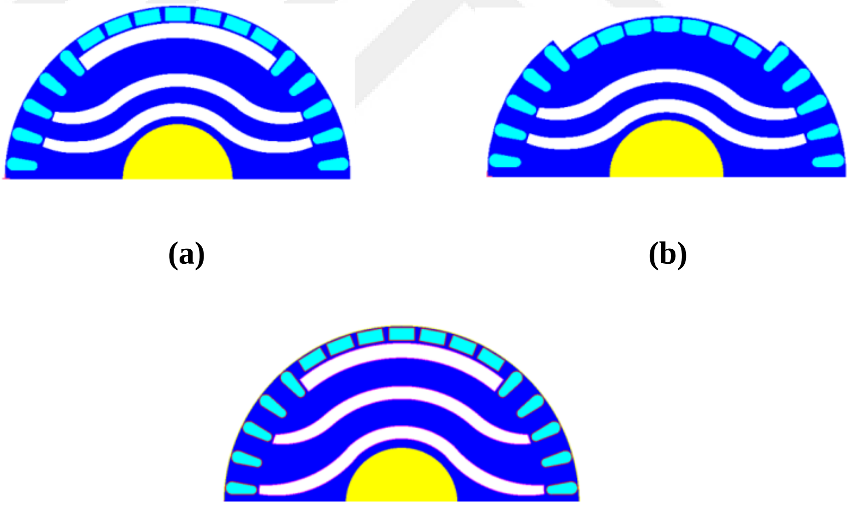

(a) (b)

(c)

Figure 2.12 (a) Initial rotor model, (b) Improved rotor model B, (c) Improved rotor model C [2]

Analysis results showed that the average magnetic flux density of the improved rotor model C is smaller which results in the increase of the d-axis inductance. On the other hand, the rotor tooth magnetic flux density is considerably high which has a negative effect on the d-axis inductance. Although the wider rotor tooth increases the inductance of the motor, it also decreases the rotor slot area and a smaller rotor slot area causes poor synchronization. Hence, the trade-off between saliency ratio and synchronization is considered, and accordingly, tooth width is optimized. The results showed that the improved rotor model C has a dramatically bigger saliency ratio and higher efficiency. A 4 pole, 90 kW LS-SynRM start-up transient and sub-transient and steady-state torque from different machine parts is analyzed using magnetic field decomposition in [43]. Additionally, cutting and punching damage affect the efficiency of LS-SynRM, and bubbles and blisters' impact on its synchronization ability is studied and discussed in [44,45]. It is concluded that reducing the bubbles/blisters effect can increase efficiency by 7 to 10%. Various conducting materials such as copper, aluminum, and graphene filled inside the flux barriers of an LS-SynRM with different configurations as seen in Figure 2.13 is proposed in [46] for pump applications. Here, the LS-SynRM with a die-casted aluminum cage inside the rotor flux barrier delivers both starting torque and reluctance torque. Then, two different rotor configurations; the first one partially filled with aluminum rotor barriers and the second one with a fully filled rotor configuration are presented at [47] as shown in Figures 2.13b and 2.13c. In this study, it is concluded that the starting torque of a fully filled rotor is 2.65% higher than partially filled one and 5.27% more efficient than the IM, and test results showed that the machine with a fully filled rotor has higher reluctance torque and better pull-in feature than the machine with the higher cage torque.

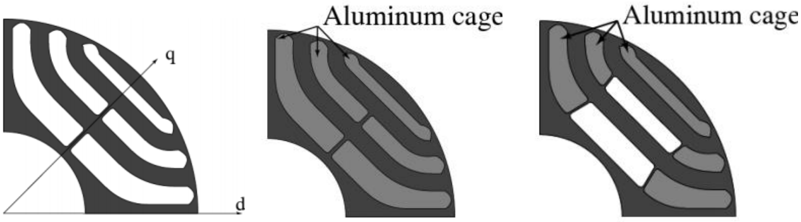

(a) **(b)** **(c)**

Figure 2.13 (a) Initial rotor geometry, (b) Fully filled rotor geometry, (c) Partially filled rotor geometry [46]

In [48], an electromagnetic design procedure for an LS-SynRM using arc-shaped and trapezoidal-shaped flux barrier rotor with constant and non-constant barrier width as shown in Figure 2.14a is presented. According to the analysis results, the study concluded that arc-shaped barriers have 10% greater saliency than trapezoidal barriers due to the reduced q-axis flux in the arc-shaped barrier. Furthermore, some pieces of PMs were inserted into the q-axis as shown in Figure 2.14b to have better steady-state performance such as higher efficiency, power factor, and torque density. Although motor synchronization is improved with the q-axis PM, a high PM flux density causes large braking torque, and accordingly, it brings out difficult start-up and synchronization [49]. As a result, the efficiency is improved by 4.62% by adding PMs on the q-axis. Then, in [50], an automatic and fast estimation optimization algorithm to see the effects of rotor parameters for improving the steady-state performance of the LS-SynRM is developed. Two types of flux barriers; arc-shaped and trapezoidal-shaped, with non-constant width and constant width are investigated. The study brings out that constant width flux barriers' magnetic saliency is larger than non-constant width flux barriers. Further, it is reported that the magnetic saliency is not changed considerably for the number of the flux barrier greater than 4, whereas the arc-shaped flux barrier has a better effect on the performance compared to the trapezoidal-shaped one.

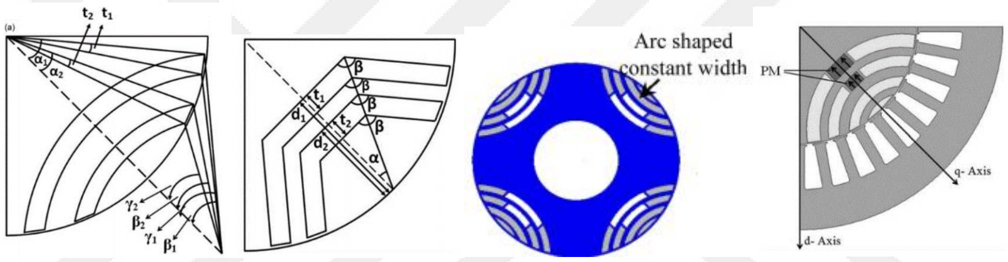

(a) (b) (c)

Figure 2.14 **(a) Constant width arc and trapezoidal rotor geometries, (b) Final constant width arc-shaped rotor geometry, (c) PMs inserted arc-shaped rotor geometry [48,50]**

4 arc-shaped rotor combinations filled with copper and aluminum alternatively in the barrier as shown in Figure 2.15 for 4 poles, 2.2 kW LS-SynRM is proposed in [51]. The first rotor R1 is filled with aluminum in the first barrier from the rotor outer periphery and is vice-versa in R2. Structures of R3 and R4 are divided into two sections with a radial rib. Each section is filled with an aluminum or copper barrier. Analysis results showed that the efficiency of the Rotor R1 is 3.8%, 5%, and 5.1% better than R2, R3, and R4 respectively. Due to the reduced rotor resistance, the PF of R2 is higher than the other competitor. Overall LS-SynRM efficiency with rotor structure R2 is 8.98% higher compared to IM. Therefore, the proposed LS-SynRM with R2 rotor structure is one of the applicable energy-efficient solutions compared to conventional IM.

Figure 2.15 **Different rotor configurations with barriers filled with copper and aluminum alternatively [3,51]**

In [52], a constant speed LS-SynRM for low power applications using a rotor made of soft magnetic material (SMC) which compose of iron powders and organic resins is proposed. The study showed that using the SMC material only in the rotor of the machine improves the efficiency of the LS-SynRM. Accordingly in [53], various rotors of LS-SynRM with different geometries and core materials are designed as seen in Figure 2.16. Here, the rotor made of SMC has reduced transient behavior compared with other types of core materials.

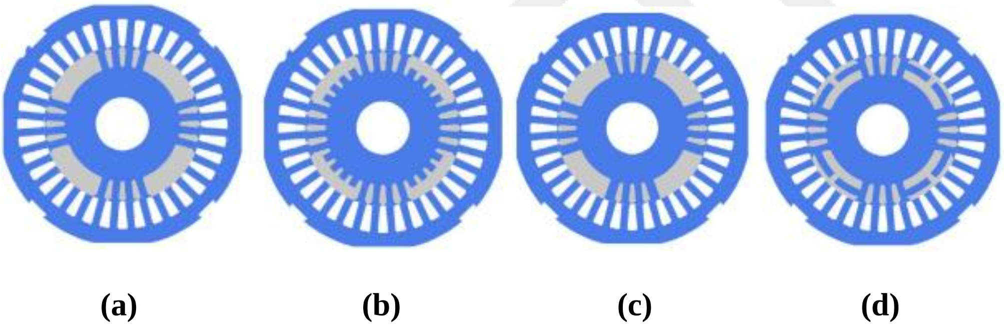

Figure 2.16 **(a) Reference rotor model, b) Rotor with additional small teeth, c) Rotor with wider outer teeth, d) Rotor with additional horizontal teeth [53]**

Recently, two different studies are proposed for submersible water pump motor application; the one with 4 pole and solar PV fed SynRM [54], and the other is 2 pole ferrite magnet assisted LS-SynRM [55]. In [54], a 2.2 kW, 4 poles synchronous reluctance motor is designed using combined analytical and FEA design. Although the design of the rotor is not explained in detail, analytical calculations are presented for designing the stator. Then, a comparison study is given and the results show that losses are eliminated by 40% and the efficiency is improved by 3-4% compared to IMs. [55] proposes a 2 pole, 3.7 kW ferrite-assisted LS-SynRM. Here, the optimum number and width of flux barriers are found by the trial-and-error method. The numbers of flux barriers analyzed are two, three, and four; and the barrier widths vary from 2 to 5.5 mm. According to the results, the highest L_d/L_q ratio is obtained when the number of flux barriers is 3 and the width of each barrier is 4 mm. The geometric optimization is done with a ready-to-use FE optimization software, OptiNet, and a comparison study carried out with and without ferrite magnets. The results showed that the efficiency of the designed LS-SynRM without ferrite magnet is 88.1% while the one with the ferrite magnets inserted is 90.1%.

2.4 Optimizations Techniques

The optimization of an electric machine design is based on adopting different parameters, geometric details, and material characteristics. The simplicity and accuracy of the model depend on the design steps. Preliminary performance estimation to reduce the computational burden in the optimization steps is very important in the machine designing process [56].

Designing a motor manually using only a trial-and-error method will not be satisfactory to determine the most optimum design parameters. Effective algorithms for machine optimization are still the object of research [57–61]. Hence, several design optimization methods such as particle swarm optimization (PSO) [62], genetic algorithm (GA), differential evolution (DE), and response surface analysis (RSA) [63,64] are used for the optimization of the design parameters of the motor. Evolutionary optimization algorithms such as PSO, DE, and GA are the most favored [11,12] among the other evolutionary algorithms. According to comparative studies in the literature [65–67], the DE algorithm has great potential for solving a wide range of difficult problems and offers better performance in terms of convergence speed and quality of the final Pareto solution set compared to the others. Therefore, the Multi-Objective Differential Evolution (MODE) algorithm is used at several stages of this study to find the best candidate design for LS-SynRM.

2.5 Conclusions

In this chapter, a detailed review of existing motor types mainly used as submersible water pump motors is provided. Here, it is observed that LS-SynRM is a strong alternative among the IM since they have higher efficiency and low-cost. Also, LS-SynRM is a better alternative than the LS-PMSM because of its low-cost and rare-earth material-free structure. Besides, since designing a motor manually using only a trial-and-error method will not be satisfactory to determine the most optimum design parameters, several optimization techniques are investigated. Among the other evolutionary algorithms, multi-objective differential evaluation algorithm is appropriate to design a motor, hence, it is used to obtain the best candidate design for LS-SynRM.

Chapter 3

Synchronous Reluctance Motor Theory

3.1 Introduction

The following chapter describes the basic reluctance principle and the utilization of an electrical motor. Then, the behavior of the Line Start SynRM (LS-SynRM is explained. Further, analytical calculations of the electrical parameters of the motor are given.

3.2 Basic Synchronous Reluctance Machine Concept

Switched and synchronous reluctance machines are the most common types of reluctance machines. This thesis study deals with a Synchronous Reluctance Machine (SynRM) concept as a part of an LS-SynRM. The torque generation of SynRM mainly depends on the reluctance of torque production. A rotating magnetic field and an anisotropic rotor shape are required for an electric machine to produce the reluctance torque. Hence a common three-phase IM stator that produces a rotating magnetic field can be utilized and a while rotor of the IM replace with the reluctance machine rotor concept. A 2-D rotor design of a typical 4-pole SynRM is illustrated in Figure 3.1 as an example.

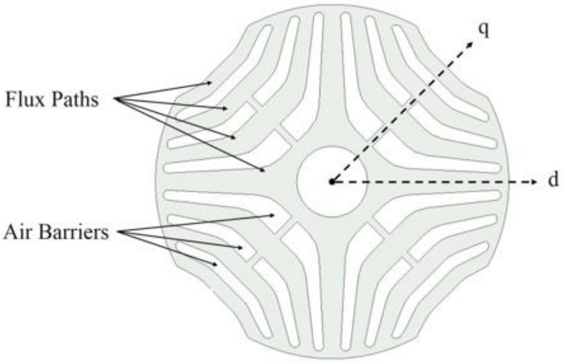

Figure 3.1 Example of a four-pole synchronous reluctance rotor

Flux in the d-axis needs to experience a low reluctance, while q-axis flux is constrained by introduced air barriers to achieving an anisotropic rotor shape. The maximum torque production depends on the inductance difference (L_d-L_q) or the ratio between the inductances (L_d/L_q). Therefore, a high torque can be obtained, while maximizing L_d and minimizing L_q. The ratio between d- and q-axis inductances is called the saliency ratio as seen in (ξ) (3.1) and the input power factor (IPF) can be described as in equation (3.2) [68].

$$\xi = \frac{L_d}{L_q} \tag{3.1}$$

$$IPF_{max} = \cos\emptyset = \frac{\xi - 1}{\xi + 1} \tag{3.2}$$

Here L_d is the d-axis inductance while L_q is the q-axis inductance.

The number and size of flux barriers should be chosen in a manner that a sinusoidal d-axis Magneto-Motive Force (MMF) in the air gap along the segments is achieved. The torque expression (T_e) can be adapted according to the number of pole pairs (n_p) while using a three-phase stator as follows (3.3). Here, i_{ds} and i_{qs} are the d and q axis currents.

$$T_e = \frac{3}{2}\frac{n_p}{2}(L_d - L_q)i_{ds}i_{qs} \tag{3.3}$$

A SynRM cannot be started directly connected to the grid since the rotor needs to be run at the same speed (synchronous speed) to produce a constant torque. The load torque is changing with respect to the angle δ, called torque, load, or current angle, between the stator flux and the d-axis of the rotor.

SynRM efficiency is usually higher than IM efficiency assuming the same outer dimension at the same output power. Rotor copper losses will be eliminated since the absence of rotor windings will lead to a significant reduction in the copper loss of the SynRM. SynRM is able to handle load changes easily at synchronous speed and it can also handle overloading up to a certain load angle. From the mechanical construction point of view, SynRMs are robust and work without any brushes and commutators. The major disadvantage of SynRM is its lower power factor compared to IM. Another drawback is that a SynRM cannot start from the line directly. The equivalent circuit of the SynRM in the *d* and *q*-reference frame and the phasor diagram of the SynRM are given in Figure 3.2 and Figure 3.3, respectively [68].

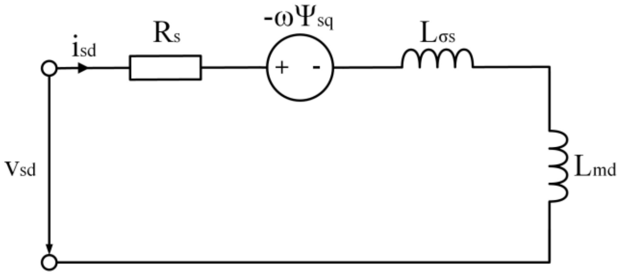

(a) d-reference frame

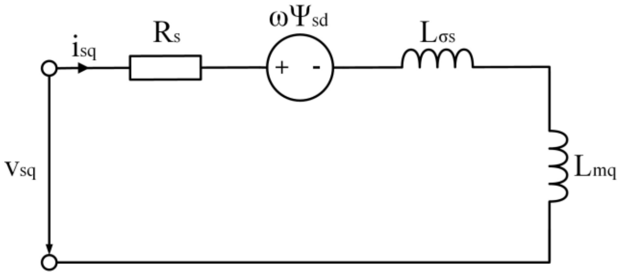

(b) q-reference frame

Figure 3.2 Equivalent circuit of the SynRM in dq-components without iron losses

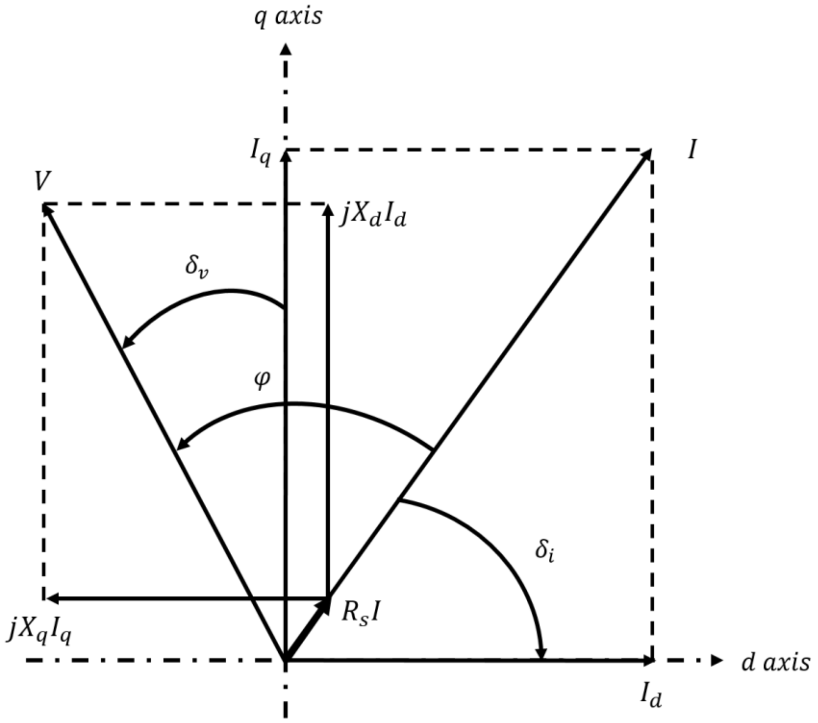

Figure 3.3 Phasor diagram of the SynRM

The stator resistance R_s and leakage inductance L_{ls} are independent of the d-and q-reference. However, the magnetizing inductances L_{md} and L_{mq} differ from each other, resulting also in different d- and q-flux linkages. Also, a cross-coupling effect of the back EMF occurs corresponding to the fluxes in the d- and q-axis. The iron losses are not considered. Equations (3.4) and (3.5) are the main equations that describe the electrical behavior of the SynRMs neglecting saturation. Here, L_{sd} and L_{sq} can be written as $L_{\sigma s}$ + L_{md} and $L_{\sigma s}$ + L_{mq}, respectively.

$$\upsilon_s = R_s i_s + \frac{d\psi s}{dt} + j\omega_s \psi_s \tag{3.4}$$

$$\psi_s = L_{\sigma s} i_s + \begin{bmatrix} L_{md} & 0 \\ 0 & L_{mq} \end{bmatrix} i_s \tag{3.5}$$

A general torque term for a three-phase machine is given in (3.6). The stator flux and current insertion lead to (3.7). When the current excitation is applied then, the torque term can be expressed as in (3.8).

$$T_e = \frac{3n_p}{2} Im\ (\psi_s i_s) \tag{3.6}$$

$$T_e = \frac{3n_p}{2} (\psi_{sd} i_{sq} - \psi_{sq} i_{sd}) = \frac{3n_p}{2} (L_{sd} - L_{sq})\ i_{sd} i_{sq} \tag{3.7}$$

$$T_e = \frac{3n_p}{2} (L_{sd} - L_{sq})\ I\ sin(\delta_i)\ I\ cos(\delta_i) = \frac{3n_p}{4} (L_{sd} - L_{sq})\ I^2\ sin(2\delta_i) \tag{3.8}$$

For the voltage excitation, the currents in (3.7) need to be expressed in terms of the voltage. The dq-quantities of stator flux and voltage can be rewritten to (3.9), (3.10), and (3.11) at a steady state.

$$\psi_{sd} = L_{sd} I_{sd} \tag{3.9}$$

$$\psi_{sq} = L_{sq} I_{sq} \tag{3.10}$$

$$\begin{bmatrix} V_{sd} \\ V_{sq} \end{bmatrix} = \begin{bmatrix} R_s & -\omega L_{sq} \\ \omega L_{sd} & R_s \end{bmatrix} \begin{bmatrix} I_{sd} \\ I_{sq} \end{bmatrix} \tag{3.11}$$

The dq-quantities of the current are obtained as in (3.12) by multiplying both sides of the matrix equation with the admittance matrix of (3.11).

$$\begin{bmatrix} I_{sd} \\ I_{sq} \end{bmatrix} = \frac{1}{X_q X_d + R_s^2} \begin{bmatrix} R_s & -X_d \\ X_q & R_s \end{bmatrix} \begin{bmatrix} V_{sd} \\ V_{sq} \end{bmatrix} \tag{3.12}$$

Here, X_d and X_q are reactances.

The voltage can be expressed in dq-quantities by introducing the voltage angle δ_v as the displacement between the voltage phasor and the q-axis as seen in Figure 3.3 [68]. The voltage of the supply in dq-quantities can be expressed as in (3.13).

$$\begin{aligned} V_{sd} &= -V\, sin(\delta_v) \\ V_{sq} &= +V\, cos(\delta_v) \end{aligned} \tag{3.13}$$

After inserting (3.13) in (3.11) the dq-stator current is obtained and the final torque expression for a voltage excited SynRM can be obtained as in (3.14) by inserting the stator current in the torque equation (3.7).

$$T_e = \frac{3n_p}{2}\,\frac{V^2}{2}\,\frac{(Lsd - Lsq)}{(X_q X_d + R_s^2)^2} \begin{Bmatrix} (X_q X_d - R_s^2)\, sin(2\delta_v) + R_s(X_q - X_d) \\ -R_s(X_q + X_d)\, cos(2\delta_v) \end{Bmatrix} \tag{3.14}$$

3.3 Line Start Synchronous Reluctance Machine

One of the major disadvantages of SynRM is that they cannot start from the line directly and require a power electronic drive to start. A cage as in the IM can be introduced to the rotor of a SynRM to overcome the non-starting ability. For this purpose, the air barriers are usually filled with a conductive material under the die cast process and the terminals of the cage are short-circuited by a ring at each end. Aluminum is mostly used as the conductive cage material. A positive additional torque component is provided during start-up from the cage. Also, the cage inserted into the rotor helps the machine to run into synchronization. After catching the synchronism, there exists no induced voltage in the cage, therefore, the losses will be reduced. The equivalent circuit of the line start SynRM is introduced in Figure 3.4 [46].

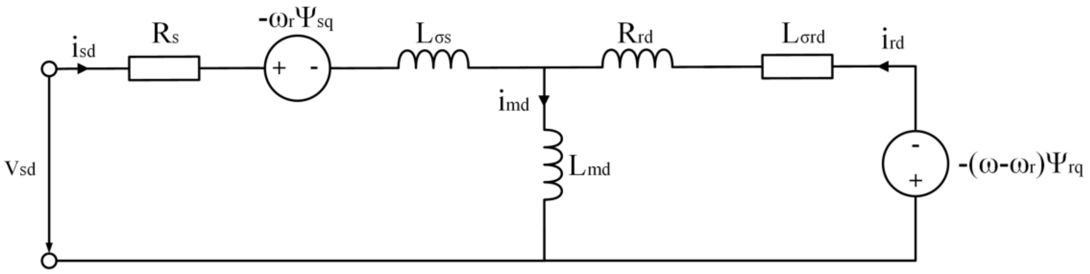

(a) d-frame

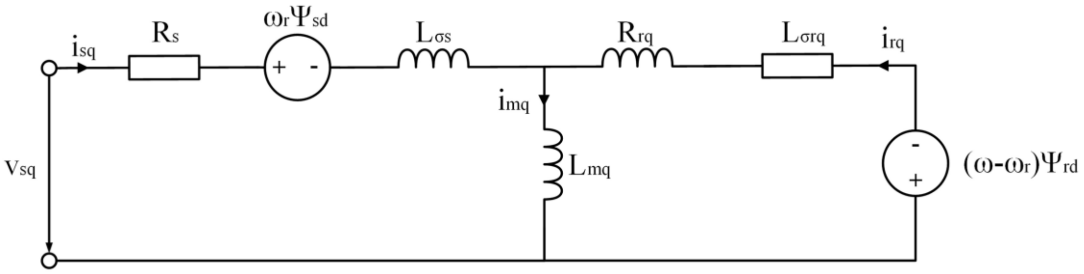

(b) q-frame

Figure 3.4 Equivalent circuit of the line start SynRM in dq-components

LS-SynRM is a hybrid technology that combines the features of squirrel cage IM and SynRM hence, additional rotor equations for the IM part are included in the system equations from (3.15) to (3.19).

$$\upsilon_s = R_s i_s + \frac{d\psi s}{dt} + j\omega_r \psi_s \tag{3.15}$$

$$0 = \begin{bmatrix} R_{rd} & 0 \\ 0 & R_{rq} \end{bmatrix} i_r + \frac{d\psi_r}{dt} + j(\omega\text{-}\omega_r)\psi_r \tag{3.16}$$

$$\psi_s = L_{\sigma s} i_s + \begin{bmatrix} L_{md} & 0 \\ 0 & L_{mq} \end{bmatrix} i_m \tag{3.17}$$

$$\psi r = \begin{bmatrix} L_{\sigma rd} & 0 \\ 0 & L_{\sigma rq} \end{bmatrix} i_r + \begin{bmatrix} L_{md} & 0 \\ 0 & L_{mq} \end{bmatrix} i_m \tag{3.18}$$

$$i_m = i_s + i_r \tag{3.19}$$

Then, the electrical torque expression during the start-up can be expressed as combinations of the cage and the reluctance torque.

$$T_e = T_{cage} + T_{rel} = \frac{3n_p}{2} Im(\psi_s i_s) \tag{3.20}$$

The system equations are expressed as in (3.21) to (3.24) while the machine is running under different slip speeds, s, to determine torque expression. The time derivatives can be replaced by $j(sw)$ in a steady state and the angular velocity of the phasors is sw taking the rotor frame as the reference.

$$V_{sd} = R_s I_{sd} + js\omega\psi_{sd} - \omega_r\psi_{sq} \tag{3.21}$$

$$V_{sq} = R_s I_{sq} + js\omega\psi_{sq} + \omega_r\psi_{sd} \tag{3.22}$$

$$0 = R_e I_{rd} + js\omega\psi_{rd} \tag{3.23}$$

$$0 = R_e I_{rq} + js\omega\psi_{rq} \tag{3.24}$$

After applying the current divider to eliminate the rotor currents, the d and q stator flux can be written as in (3.27) and (3.28) using equations (3.25) and (3.26) as follows.

$$I_{rd} = js\omega L_{md} R_{rd} + js\omega L_{rd} I_{sd} \tag{3.25}$$

$$I_{rq} = js\omega L_{mq} R_{rq} + js\omega L_{rq} I_{sq} \tag{3.26}$$

$$\psi_{sd} = \left(L_{sd} - \frac{js\omega L_{md}^2}{R_{rd} + js\omega L_{rd}}\right) I_{sd} = Z_{pd} I_{sd} \tag{3.27}$$

$$\psi_{sq} = \left(L_{sq} - \frac{js\omega L_{mq}^2}{R_{rq} + js\omega L_{rq}}\right) I_{sq} = Z_{pq} I_{sq} \tag{3.28}$$

Here, Z_{pd} and Z_{pq} are the operational impedances. The matrix which expresses the relation between the voltage and the current is given in (3.29). While multiplying both sides of this matrix with the admittance matrix, the matrix that expresses the stator current can be obtained as follows [46].

$$\begin{bmatrix} V_{sd} \\ V_{sq} \end{bmatrix} = \begin{bmatrix} (R_s + js\omega Z_{pd}) & -(1-s)\omega Z_{pq} \\ (1-s)\omega Z_{pd} & (R_s + js\omega Z_{pq}) \end{bmatrix} \begin{bmatrix} I_{sd} \\ I_{sq} \end{bmatrix} \tag{3.29}$$

The stator voltage can be written as in (3.30). If the slip is not zero, the voltage quantities become rotating phasors in the dq-frame. Hence, the voltage when $s \neq 0$ can be written as (3.33), and δ_v can be neglected.

$$V_{sd} = -V \sin(s\omega t + \delta_v)$$
$$V_{sq} = +V \cos(s\omega t + \delta_v) \tag{3.30}$$

$$V_{sd} = jV$$
$$V_{sq} = V \tag{3.31}$$

$$\begin{bmatrix} I_{sd} \\ I_{sq} \end{bmatrix} = \frac{1}{D_c} \begin{bmatrix} (R_s + js\omega Z_{pq}) & (1-s)\omega Z_{pd} \\ -(1-s)\omega Z_{pq} & (R_s + js\omega Z_{pd}) \end{bmatrix} \begin{bmatrix} jV \\ V \end{bmatrix} \tag{3.32}$$

$$D_c = R_s^2 + js\omega R_s(Z_{pd} + Z_{pq}) + (1 - 2s)\omega^2 Z_{pd} Z_{pq} \tag{3.33}$$

The real and imaginary parts of stator current and flux are substituted by variables, which leads to (3.34), then, is inserted in the torque equation (3.6).

$$I_{sd} = a + jb$$
$$I_{sq} = c + jd$$
$$\psi_{sd} = e + jf$$
$$\psi_{sq} = g + jh \tag{3.34}$$

The cage and reluctance torque can be re-calculated through the equations (3.35) to (3.36) [46]. The cage torque does not depend on the slip, hence it is constant at different slips. The cage is supposed to accelerate the machine's speed to asynchronous speed as close to synchronous speed as possible. On the other side, the reluctance torque contribution is a trigonometric function oscillating with twice the slip frequency.

$$T_e = T_{cage} + T_{rel} \sin(2s\omega t - \alpha) \tag{3.35}$$

$$T_{cage} = \frac{3n_p}{4}(ce + df - ga - bh) \tag{3.36}$$

$$T_{rel} = \frac{3n_p}{4}\sqrt{(ce + bh - df - ga)^2 + (ed + cf - gb - ah)^2} \tag{3.37}$$

$$\alpha = \arctan\left(\frac{gb + ah - ed - cf}{ce + bh - df - ga}\right) \tag{3.38}$$

3.4 Analytical Calculations of the Motor Electrical Parameters

3.4.1 Phase Resistance Calculation

Since phase resistance affects the current flowing through the winding and also the copper loss on that winding, it is very important to calculate. The straightforward phase resistance calculation is given in (3.39) at 25°C. The variation of the phase resistance depends on the resistivity of copper, total wire length, and wire area.

$$R = \rho_{cu} \frac{(N_{coil} \times L_{wire} + L_{con})}{A_{wire}} \tag{3.39}$$

where ρ_{cu} is the resistivity of copper, N_{coil} is the number of coils per phase and L_{wire} is the conductor length in one coil, L_{con} is a conductor used for the connection of coils
and A_{wire} is the area of the conductor.

Resistance of the phase changes with respect to the temperature. Therefore, the phase resistance is needed to be calculated at the working temperature of the motor while it is operating at a steady state. This temperature is given in (3.40) which is obtained when the motor no longer heats up at rated conditions around 150 °C. Calculating the value of this resistance is very important since it affects the nominal values of the machine.

$$R' = R \frac{234.5+T}{234.5+25} \Big|_{T=150^{\circ}\mathrm{C}} \tag{3.40}$$

Here, the slot area, wire diameter, and total wire length have to be determined first to calculate the resistance value.

3.4.1.1 Calculation of Wire Cross Section Area

The wire cross-sectional area can be calculated as in (3.41). Here, k_{fill} is the filling factor and is mainly determined by the manufacturer. After the determination of the fill factor, an appropriate copper can be chosen.

$$A_{wire} = \frac{1}{2} \frac{k_{fill} A_{slot}}{N_{turn}} \tag{3.41}$$

where N_{turn} is the number of turns per coil and A_{slot} is the stator slot area.

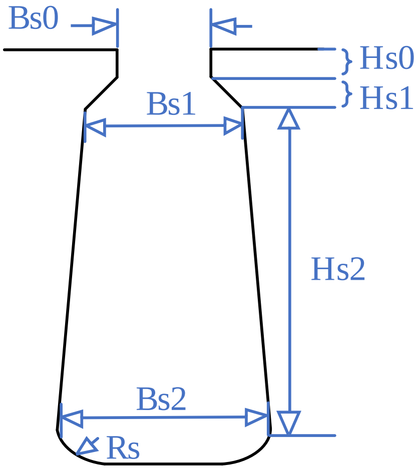

Figure 3.5 Stator slot dimensions

The stator slot type is determined as slot type 3 from the ANSYS Maxwell Software and the dimensions are shown in Figure 3.5. Since it is very similar to a trapezoid, the calculations are done accordingly as in (3.42). The slot type used in the motor is a semi-closed slot that is connected to an air gap with a slot opening and the slot area is calculated geometrically.

$$A_{slot}=\frac{1}{2}(Bs1+Bs2)\,Hs2 \tag{3.42}$$

3.4.1.2 Conductor Length Calculation

The total conductor length in one coil can be calculated while conductors are assumed to be placed in the middle of the slot. The illustration of the conductor parts is given in Figure 3.6.

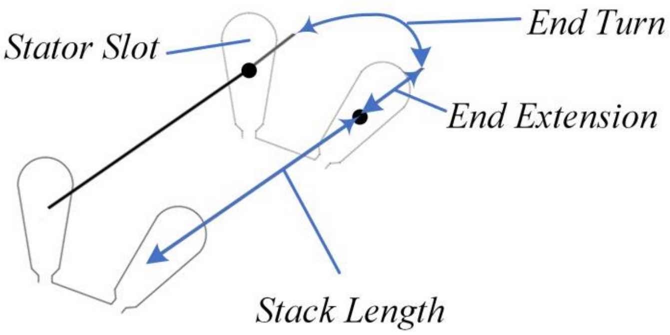

Figure 3.6 Conductor Parts

Here, the conductor in the stator core (stack length) is shown in black, the blue lines represent the external conductor length, and the red part is the arc-shaped conductor between two sides of a coil. Therefore, the total length of the conductor can be expressed as:

$$L_{wire} = 2\,N_{turn}\,[L_{stack} + L_{ext} + (\frac{S_{pitch}}{N_{slot}}\,(D_{si} + h_{slot})\,\pi)] \tag{3.43}$$

where N_{turn} is the number of turns per coil and N_{slot} is the number of slots, L_{stack} is the stack length and L_{ext} is the external length in the radial axis of the motor. S_{pitch} is the stator slot pitch and it is calculated by dividing the number of stator slots by the number of poles. D_{si} is the inner diameter of the stator and h_{slot} is the length of each stator slot.

3.4.2 Stator Leakage Inductance Calculation

The leakage inductance can be calculated with two components of inductance which are slot leakage inductance and end winding leakage inductance. In case that machine has permanent magnets, magnetizing inductance calculations due to placements of the magnets should be included.

3.4.2.1 Calculation of Slot Leakage

The slot leakage inductance calculation is an important element of the electric machine’s design. The slot leakage inductance can be calculated as follows [69].

$$p_{slot} = \mu_0 \left(\frac{Hs0}{Bs0} + 2\,\frac{Hs1}{Bs1 + Bs2} + k_s\,\frac{Hs2}{3 \times Bs1} \right) \tag{3.44}$$

here k_s is a constant coming from slot geometry which can be obtained using (3.45).

$$k_s = 3\,\frac{(4s^2 - s^4(3 - 4\ln(s) - 1))}{(s^2 - 1)^2(s - 1)} \tag{3.45}$$

where s is the ratio of the top width of the slot over the bottom width of the slot (*Hs2/Hs1*). Therefore, the leakage inductance can be calculated using slot leakage permeance as in (3.46).

$$L_{slot} = 3\,\frac{N^2 L}{N_{slot}}\,p_{slot} \tag{3.46}$$

3.4.2.2 Calculation of End Winding Inductance

A leakage exists on end-winding which is the part of the motor lamination. The total length of end-winding has to be calculated to obtain the end winding leakage inductance. The leakage inductance parameter can be derivated by calculation of the length of the distance (w_{c1}) that end winding is located on the radial axis out of the motor's axial axis. L_{1e} is the total end winding length [69].

$$w_{c1} = \pi(D_{si} + h_{slot})\frac{S_{pitch}}{N_{slot}} \tag{3.47}$$

here is assumed that the end winding turns out from a diameter; $D_{si} + h_{slot}$. The total end winding length is given as:

$$L_{1e} = 2\,L_{ext} + w_{c1} \tag{3.48}$$

Also, end winding leakage permeance, p_e, a calculation which is given in (2.51) is necessary to achieve the end winding leakage.

$$p_e = 0.34\,\mu_0\,(1 - \frac{2}{\pi}\frac{w_{c1}}{\mathrm{L1e}})\,\frac{N_{slot}}{N_{phase}N_{pole}} \tag{3.49}$$

where N_{phase} and N_{pole} are the number of phases and number of poles respectively. The end winding leakage derivation can be obtained as in (3.50) using (3.47), (3.48), and (3.49).

$$L_{ew} = 2p_e\,\frac{(N_{coil}N_{turn}k_s)^2}{\frac{N_{pole}}{2}\,\frac{N_{slot}}{N_{phase}N_{pole}}}\;L1_e \tag{3.50}$$

Therefore, the total leakage inductance can be obtained using (3.46) and (3.50).

$$L_{\mathrm{total\_leak}} = L_{\mathrm{slot}} + L_{\mathrm{ew}} \tag{3.51}$$

3.4.3 Losses

Machine losses are one of the key issues that must be calculated precisely to determine the overall machine performance accurately. Moreover, when optimization is going to be carried out the loss prediction or calculation, it becomes more challenging. It is a fact that losses must be considered and modeled carefully to find the optimum design.

In this section, the losses are classified into four groups which are copper, core and friction, and windage loss.

3.4.3.1 Copper Loss

The copper loss was calculated using phase resistance R and rms armature current I. The total winding loss belonging to the stator is calculated as (3.52).

$$P_{cu} = 3I^2R \tag{3.52}$$

It should be noted that since the copper losses depend on the phase resistance and working condition temperature of the machine accordingly, calculations must be updated under different working conditions.

3.4.3.2 Core Loss

Core loss estimation can be obtained using finite element numerical computations. The following equation allows calculating the core loss in two parts: eddy and hysteresis losses.

$$P_{loss} = (k_h f B^2 + k_e f^2 B^2)\ M \tag{3.53}$$

Here, k_h and k_e are the hysteresis and eddy losses constants, respectively. f is the operating electrical frequency, B is the peak of flux density and M is the total weight of the medium where loss is calculated. A more detailed explanation and several different methods for calculating the core losses exist in [70,71].

3.4.3.3 Friction and Windage Losses

Friction and windage losses are assumed to be very small and do not affect the total loss result. However, the windage losses become significant under high-speed operations [72]. The theoretical equation for windage loss estimation of a smooth cylinder rotating within a concentric cylinder is given in [73] as follows.

$$P_w = C_d \rho \pi r^4 \omega^3 L \tag{3.54}$$

where P_w is the damping loss, C_d is the skin friction coefficient, ρ is the density of the fluid (kg/m^3), r is the radius of the rotor (m), ω is the angular velocity (rad/s) and L is the rotor length (m).

Skin friction coefficient C_d is calculated as [73]:

$$\frac{1}{\sqrt{C_d}}=2.04+1.768\ \ln(R_e\sqrt{C_d}) \tag{3.55}$$

where R_e is the Reynold number and can be expressed as [73]:

$$R_e= \omega\ r\,\frac{\rho}{\mu}\varphi \tag{3.56}$$

where μ is the dynamic viscosity of the cooling fluid (Pa.s or N.s/m^2 or kg/(m.s)) and φ is the airgap length (m).

3.5 Conclusions

The basic working principle of SynRM is explained in Chapter 3, before starting the proposed LS-SynRM design steps. Moreover, the basic insight to calculate the electrical parameters and loss mechanism of the reluctance concept is given here.

Chapter 4

Multi-Objective Differential Evolution Optimization Algorithm

4.1 Introduction

Differential evolution (DE) is one of the evolutionary algorithms which is first introduced in [66,74]. DE algorithm is a suitable evolutionary algorithm for solving nonlinear and multi-constrained complex optimization problems. In this chapter, the general workflow of the DE is described.

4.2 Differential Evaluation Optimization Process

In DE, perturbing the vector population is done by using vector differences. DE has similarities with traditional evolutionary algorithms; however, the DE algorithm runs with real numbers rather than operating in binary form as in the genetic algorithm (GA) and it does not use a probability function. Instead, DE performs the mutation-based distribution of the solutions in the current population. In this way, search direction and possible step sizes depend on the location of the individuals selected to calculate mutation values [75].

After specifying the population size, *M,* both upper, x_u, and lower limits, x_l, must be specified for each design variable. Then, the first generation is initialized based on the normal distribution. The crossover probability factor, C_r, and the scaling vector, *F,* should also be defined here. The main DE process includes the procedures of initialization, mutation, crossover, and selection [66,76].

After deciding on the variables to be optimized as,

$$x = \left[K_{rt}, K_{sl}, K_{ry}, S_e, R_e, K_{dsi} \right] \tag{4.1}$$

the initial values of the first generation design variables of the population are formed. The initial values of the j^{th} (j= 1,…, M) design variable of the i^{th} (i= 1,…, N) vector in the first generation can be expressed as:

$$x_{j,\,i,1} = rand_j\left(\left[1, N\right]\right)\left(x_u - x_l\right) + x_l \tag{4.2}$$

where N is the dimension of a solution, and the final value of i, $rand_j\ ([1, N])$ is a $1\mathrm{x}N$ vector while $0 \leq rand_j(1\mathrm{x}N) < 1$.

Then, three different vectors $x_{r1,g}$, $x_{r2,g}$ and $x_{r3,g}$ are randomly selected to generate a mutant vector $v_{i,g}$. This process adds a scaled difference between two randomly selected vectors to a third vector and can be expressed as follows [77,78]:

$$v_{i,g} = F \times \left(x_{r1,g} - x_{r2,g}\right) + x_{r3,g} \tag{4.3}$$

where F is the scaled factor which varies between 0 and 1, and g varies from 1 to G where G is the number of generations.

Trial vector $u_{i,g}$ is generated out of two different vector variables, namely; $x_{i,g}$ and $v_{i,g}$ by crossover procedure which is formulated as follows [76,78]:

$$u_{i,g} = (u_{j,i,g}) \ = \left[u_{j,1,g},\ u_{j,2,g,}u_{j,3,g} \ldots\ u_{j,i,g}\right] \tag{4.4}$$

$$u_{j,i,g} = \begin{cases} v_{j,i,g}, & if\ rand_j\left(0;1\right) \leq Cr \\ x_{j,i,g}, & otherwise \end{cases} \tag{4.5}$$

where the user-defined crossover probability factor changes between $0 \leq C_r \leq 1$. Here, if the random number of the j^{th} variable in the i^{th} vector is less than or equal to C_r, the trial vector $u_{i,g}$ is equal to the mutant vector $v_{i,g}$. Otherwise, the trial variable is copied from vector $x_{i,g}$.

In the selection process of the DE algorithm, the objective cost functions will evaluate the performance of each candidate design. Then, the trial vectors, $u_{\mathrm{i,g}}$, are compared to the target vectors $x_{i,g}$, including the constraints and design objectives in the current generation. It should be noted that the constraints are handled as objectives, which is called Lampinen's selection criterion, and is adopted here as described below:

$$
x_{i,g+1} = \begin{cases} u_{i,g}, & if \begin{cases} \begin{cases} \Gamma_m(u_{i,g}) \le 0 \ and \ \Gamma_m(x_{i,g}) \le 0, \\ f_n(u_{i,g}) \le f_n(x_{i,g}); \end{cases} \\ or \\ \begin{cases} \Gamma_m(u_{i,g}) \le 0, \\ \Gamma_m(x_{i,g}) > 0; \end{cases} \\ or \\ \begin{cases} \Gamma_m(u_{i,g}) > 0 \ , \\ \max\left(\Gamma_m(u_{i,g}),0\right) \le \max\left(\Gamma_m(x_{i,g}),0\right); \end{cases} \end{cases} \\ x_{i,g}, & otherwise \end{cases} \tag{4.6}
$$

where f and Γ are the cost and constraint vectors, respectively.

The optimization process starts from a random parameter set within the specified parameter boundaries and iterates until the pre-defined criteria which are to reach the maximum number of generations are satisfied. Hence, the design performance will be improved each time until achieving the best set of results, Pareto frontier [79].

The traditional MODE algorithm is not only meant for geometric motor optimization to obtain higher quality results in a computationally efficient way. Hence, some modifications are needed such as an improved Pareto front selection algorithm, variable population size, and scaling factors. These modifications are described in Section 4.3

4.3 Modifications on the Traditional MODE Algorithm

4.3.1 Modifications on the Pareto Front

The first insufficiency of the MODE Algorithm is related to its Pareto front approach. Generally, Pareto front takes the last generation of the optimization. However, this approach makes it harder to obtain a well-distributed candidates among various objectives. Usually, the optimization is dominated by only one objective. Consequently, the results of the last parent matrix are biased in favor of the first objective. Furthermore, since the comparison between the parent matrix and the child matrix is performed with respect to the same line, superior results can be omitted from the last parent. Therefore, considering that the first line of the parent matrix contains a high-quality result while the next line of the parent matrix does not have a desirable one. After obtaining the solution of the child matrix, better results accumulate in the first line. The DE algorithm continues with the first line as a new parent matrix rather than the second line. Furthermore, the higher quality result from the old parent is lost during the process. Therefore, a modified Pareto front algorithm is used to obtain a better distribution on the Pareto frontier solution set. Here, a resizable matrix is defined for the Pareto front. In every generation, all lines of the parent vector are checked if there is a better result exists in the Pareto front solutions. Since the Pareto front is re-sizable, a better distribution can be achieved.

4.3.2 Modifications on the Selection

As mentioned before, an optimization algorithm contains objectives and constraints. Having constraints significantly affects the selection process. Traditionally, the selection algorithm is set to check the constraints first followed by checking the objectives. This way selecting a candidate outside the limitations is avoided. Therefore, the selection algorithm is modified to have a strict rule for the constraints to be within their predefined limits. Such an approach becomes handy when eliminating unacceptable results among the candidates.

However, reviewing the objectives is a tedious process as the MODE consists of multiple objectives that have a trade-off between one another. In order to obtain a decent Pareto frontier distribution, the parent matrix should not be influenced by a specific objective. An easy solution may involve reviewing the objectives in a specific order. Hence, if the population in the child matrix has a better result for any of the objectives, it becomes a parent. On the other hand, reviewing the objectives in such an order may result in a dominance between the first reviewed objective and the last one. To avoid this phenomenon, the selection is done by splitting the parent matrix into two to perform the review from the first to the last objective. For the second side, the reviewing is done through the last one to the first one.

4.3.3 Modifications on the Population Size

The traditional DE algorithm has a fixed population size for all generations. However, the electric machine optimization has multiple constraints which would make most of the randomly selected candidate designs invalid. Hence, having a fixed large generation number affects the computation time and speed of the optimization. Therefore, a variable population size approach is used in this work. The optimization algorithm only attempts to meet constraint boundaries first; therefore, using a low number of populations becomes more effective. During the process, as each generation pass, the main goal becomes to obtain better distributed candidates; Hence, the population size is increased. Additionally, to achieve a reasonable computation time, a limit for the population size is added.

4.3.4 Modifications on the Scaling Factor

Keeping the scaling factor constant causes the optimization to chatter between similar results and makes it hard for the algorithm to seek better results in smaller steps. Especially through the end of the optimization, obtaining finely tuned parameters with a high scaling factor is a low probability. On the other hand, keeping the scaling factor small will not result in the desired response as the results will be distributed in a small area between the different objectives. Therefore, a variable scaling factor that is decreasing in each generation was found to be the viable option. This way, the optimization leads to a well-distributed parent sets in the first generations and higher quality results for the last generations.

4.3.5 Modifications on the Rectification

Another intrinsic problem of the MODE is the stuck parent matrix in a single place with a small distribution or jitter between the local optimal states. To avoid such a situation, the modified Pareto front approach is found to be helpful. As the candidates in the Pareto front solution set merely consist of the best results, it can be directly inserted as a new parent. To ensure a good distribution, a dominance filter is used. The dominance filter removes the candidates that are absolutely dominated by the other candidates in terms of all objectives. As a result, only the best results are kept in the Pareto front. However, using the dominance filter for each generation affects the distribution negatively; Hence, the dominance filter is applied with a certain number of generation periods.

4.4 Conclusions

In this chapter, the selected optimization method, MODE, is described and the process belongs the algorithm is provided. The traditional MODE algorithm’s ineffective sides are discussed and methods that provide improvements are presented.

Chapter 5

Oval Shaft Line-Start Synchronous Reluctance Machine for Submersible Water Pump Applications

5.1 Introduction

LS-SynRM starts as an IM due to the conductor bar structure inserted into the rotor and once catching the synchronous speed, it runs as a SynRM merely relying on saliency torque that is due to the flux barriers on the rotor. Therefore, L_d/L_q ratio is the main design parameter as the only torque provider is the reluctance and it depends on the number, position, and shape of the flux barriers. In this chapter, several oval shaft LS-SynRM rotors with several number of flux barriers along with the thicknesses of the barrier and carrier are designed and optimized to achieve high saliency, reluctance torque, and efficiency accordingly.

Since the submersible pump motors run inside a fluid-filled environment, the damping effect of the fluid has to be taken into account during the design process. Damping loss is investigated since the water is denser than the air and it causes more loss compared to the windage loss. Therefore, in this study, the fluid damping loss is estimated using computational fluid dynamics FEA.

In this thesis study, it is aimed to reduce the overall cost of the submersible water pump system by designing and optimizing a new oval shaft LS-SynRM as a submersible pump motor with higher efficiency compared to the conventional IMs. Moreover, it is aimed to prove that an appropriate optimization technique and several analyses must be included such as fluid damping loss, structural, thermal analyses, etc. to have proper machine design in contrast with the existing LS-SynRM studies. Here, the machine performance is improved by widening the flux path on the rotor by narrowing down the shaft on the q-axis. In this way, a wider d-axis flux path is obtained, and the d-axis inductance is increased. The structural properties of the rotor with an oval shaft structure are investigated during the design stage carefully. For the safe maximum shaft dimension limits, a series of structural analyses are performed using FEA. A comparison study is carried out to prove the superiorities of the proposed motor over IMs.

Furthermore, since air-gap flux with space harmonics induces excessive copper and core losses in addition to vibration and acoustic noise [78–80], a proper configuration of stator windings with reduced winding MMF space harmonic content which leads to improved machine performance is investigated.

Last but not least, the candidate machines' synchronization capabilities under several loading conditions are investigated and the thermal analysis of the candidate design is performed.

In summary, studies that aim to increase the efficiency of the pump motor throughout this thesis will improve the overall pump system performance. Accordingly, it will lower energy and maintenance costs, and easy process control will be achieved. All these will result in dramatic nationwide cost savings. This is a crucial strategy for any facilities management that wants to improve the sustainability, productivity, and cost management of the facilities.

5.2 Proposed Motor Structure and Optimization

The reluctance torque principle is based on the existence of a rotating magnetic field and an anisotropic rotor shape. To achieve an anisotropic rotor shape, the flux in the d-axis should experience a low reluctance, while the flux in the q-axis is constrained by introduced air barriers. The maximum torque produced by the machine depends on the inductance difference, whereby a high torque can be exploited if maximizing L_d and minimizing L_q. The ratio of the inductance in the d- and q-axis is called as saliency ratio. LS-SynRM starts as an IM due to the conductor bar structure inserted into the rotor and once catching the synchronous speed, it runs as a SynRM merely relying on saliency torque that is due to the flux barriers on the rotor. Therefore, L_d/L_q ratio is the main design parameter as the only torque provider is the reluctance and it depends on the number, position, and shape of the flux barriers. In an LS-SynRM, all the flux goes through the flux carriers. As the flux barriers have to exist and make space along the q-axis, they create a bottleneck in the main flux path. As a result, the d-axis inductance is affected negatively. To overcome this bottleneck and widen the flux carriers, the circular shaft structure is narrowed down on the q-axis.

5.2.1 Flux Barriers Design

Here, several oval shaft LS-SynRM rotors with 7 to 10 number of flux barriers along with the thicknesses of the barrier and carrier are designed and optimized to achieve high saliency, reluctance torque, and efficiency accordingly. Here, the effects of the different flux barriers on the performance of the LS-SynRM with an oval shaft are investigated. MODE algorithm is employed to find the optimum flux barrier number and thickness for both flux barriers and carriers for each rotor design [74].

5.2.2 Rotor Bar Thickness

To generate sufficient torque and start-up torque with the machine under the pump load, the rotor bar cross-sectional area should be selected appropriately. In this work, the rotor bar shape is selected as the circle for ease of manufacturing. The minimum diameter for a specific design is determined as follows [9]:

$$A_r = \frac{I_b}{\delta_r} \tag{5.1}$$

where A_r is the area of the rotor conductor bars in mm^2, δ_r is the current density in A/mm^2 and I_b is the rotor conductor bar current which is calculated as:

$$I_b = \frac{\left(K_{ws} S_s Z_s\right) I_r}{\left(K_{wr} S_r Z_r\right)} \tag{5.2}$$

where K_{ws} is the winding factor of the stator, S_s is the number of stator slots, Z_s is the number of conductors/stator slots, K_{wr} is the winding factor of the rotor, S_r number of rotor slots, Z_r is the number of conductors/rotor slots and I_r is equivalent rotor current in terms of stator current which is expressed as $I_r = 0.85 I_s$ where I_s is the stator phase current. Rotor also has 0.5 mm bridges on it to increase the strength of the structure.

5.2.3 Stator Winding Current Density

Since the motor is operating in a downhole filled with fluid, the range of current density can be higher than an air-cooled machine, and it is selected as between 3-10 A/mm^2 for this study [80].

5.2.4 Stator Geometry and Number of Turns

Parameters regarding the stator design are kept the same with a 4 kW, 6-inch commercial submersible pump IM where the related analysis is presented in Section 5.4 for a fair comparison. A 24-slot stator configuration is used for this study. The outer radius of the motor (r_{MO}) is specified as 68 mm whereas the stator's inner radius is 34 mm. The length of the tooth width (l_{TW}) is taken as 3.2 mm and the slot depth parameter (l_{SD}) is set to 20.5 mm. The air gap length (g) is fixed at 0.35 mm and the rotor outer clearance (l_{OC}) is predetermined as 0.5 mm based on the manufacturing limits.

Two dependent parameters are optimized directly. One of them is the stack length. Since the motor is expected to provide 4 kW output power with a rotation speed of 3000 rpm, 12.75 Nm torque is required to be generated. Here, the torque is calculated for 25 mm stack length for all the candidate designs, then, it is linearly scaled for providing 12.75 Nm torque. The second parameter is the number of turns of the coils. To get the highest torque possible, the number of turns, N_t, is calculated based on the RMS value of the current, I_{rms}, current density, J, and the slot area A_{slot} as follows:

$$N_t = \frac{JI_{rms}}{A_{slot}k_{fill}} \tag{5.3}$$

Due to manufacturing limitations, the fill factor, k_{fill}, is selected as 0.30, similar to the commercial IM.

5.2.5 Geometric Optimization Process

To perform geometric optimization, an FEA model is developed in ANSYS Maxwell 2D. For the initial model, many geometric definitions decrease the efficiency of the optimization. To increase the optimization efficiency, the number of geometric design parameters is reduced to eight parameters which are highly effective on the output parameters. This way, all the critical parameters are considered while making the optimization faster by using a limited number of parameters to optimize. Visual representations of these parameters are shown in Figure 5.1 and related explanations are given in Table 5.1. Furthermore, in order to find the best possible results with respect to the objectives, a variety of working conditions should be tested. For conducting such analysis, some non-geometric parameters such as current density and the maximum current are also added as a parameter to the optimization. Parameters regarding the stator shape are set to a fixed value for a direct comparison with the conventional structure. One of the crucial optimization parameters is the *Dos* which represents the measurement of circle shaft size reduction in q-axis in mm. This parameter will be handled in Section 5.3 deeply.

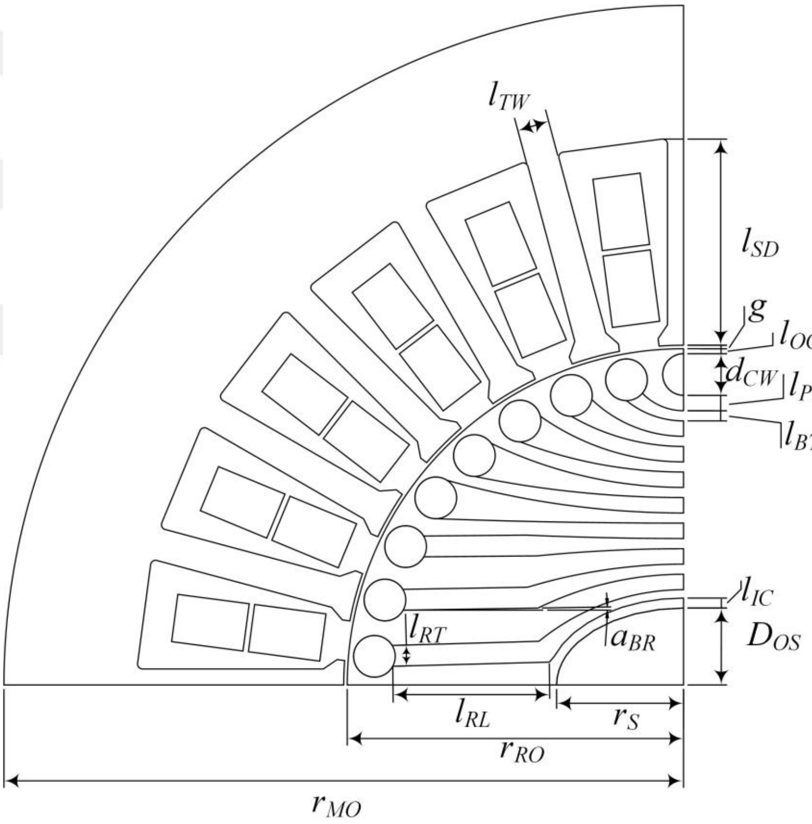

Figure 5.1 Visual representation of geometric design parameters

In this study, the MODE algorithm is implemented in MATLAB and all the FEA analyses are performed in Ansys Maxwell. Communication between these software is established through Windows ActiveX commands. The flowchart of this process is illustrated in Figure 5.2. The optimization is operated for 75 generations with a population number that varied between 16 and 64. A total of 2425 candidate designs are simulated for all the oval and circular shaft machines.

Table 5.1 Optimization Parameters

Parameter	Definition	Boundaries
a_{BR} [degree]	Bar rectangular section tilt angle	0 – 10
l_D [mm]	Shaft Radius (r_S) − Elliptic Shaft Radius (r_{ES})	0 – 5
l_{IC} [mm]	The distance between the shaft and the first flux barrier	1 – 5
k_B	$\frac{\text{MidPoint Barrier Thickness } (l_{BT})}{\text{MidPoint Plate Thickness } (l_{PT})}$	0.16 – 0.6
k_C	$\frac{\text{Rotor Conductor Diameter } (d_{CW})}{\text{Maximum Rotor Conductor Diameter}}$	0.67 – 0.85
k_R	$\frac{\text{Rectangular Barrier Length } (l_{RL})}{\text{Maximum Possible Length}}$	0.5 – 0.9
k_{REC}	$\frac{\text{Rectangular Barrier Thickness } (l_{RT})}{\text{Cage Cylinder Diameter } (d_{CW})}$	0.35 – 0.75
Dos [mm]	Measurement of circle shaft size reduction in q-axis	0-5
J [A/mm^2]	Peak current density	3 – 10
I_{peak} [A]	Peak phase current	5 – 15

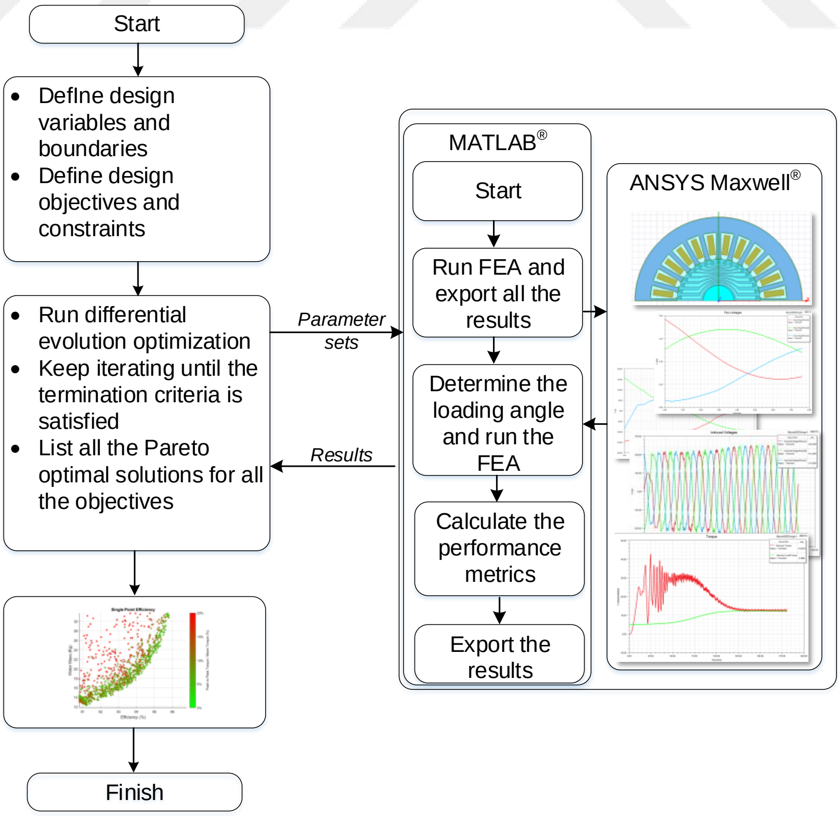

Figure 5.2 Workflow of the optimization process

MODE optimization algorithms work based on a cost definition that has several objectives and constraints. The efficiency and the torque density are selected as the objectives of this optimization. However, due to the fact that the average torque value is predetermined (12.75 Nm at a speed of 3000 rpm), the second objective is simplified to motor mass. Also, in order to be able to operate with the line voltage, the motor terminal voltage has to be within the 5% band of the actual line voltage amplitude. Hence, the motor terminal voltage and torque ripple are set as constraints. Furthermore, motor mass is also added among constraints to get more manufacturable results from the optimization. The objectives and constraints of the optimization, calculation methods, and the limits of the constraints are given in Table 5.2 and Table 5.3, respectively.

Table 5.2 Optimization Objectives

Design Objectives	**Calculation Method**
Efficiency	$\frac{\textbf{Output Power}}{\textbf{Output Power} + \textbf{Losses}}\,\mathbf{100}$
Motor Mass	(Area (Stator) + Area (Rotor)) Stack Length + Copper Mass

Table 5.3 Optimization Constraints

Design Constraints	**Calculation Method**	**Boundaries**
Line Voltage (V)	$\max(e\angle\emptyset^{\circ} + I\angle\delta^{\circ}(r_s + \mathrm{j}X_L))$	220 – 230
Torque Ripple (%)	$\frac{\text{Peak To Peak Torque}}{\text{Average Torque}}100$	0– 50
Motor Mass (kg)	$(A_{Stator} + A_{Rotor})L_{stack} + M_{Copper}$	0 – 25

Here, $e \angle\emptyset^{\circ}$ is the back emf voltage, $I \angle\delta^{\circ}$ is the phase current, r_s is the phase resistance, X_L is the leakage inductance reactance, A_{stator} and A_{rotor} are the stator and rotor areas, L_{stack} is the stack length, and M_{Copper} is the copper mass.

5.2.6 Analysis Results

The optimization study is performed at 3000 rpm while the machine is generating 12.75 Nm output torque. Synchronous performance analysis results in terms of mass, efficiency, and torque ripple for each design are presented in Figure 5.3. Here, the candidates that satisfy all the constraints are superior to the others in terms of efficiency, mass, and torque ripple. They are also called dominant results and are represented with diamond shapes.

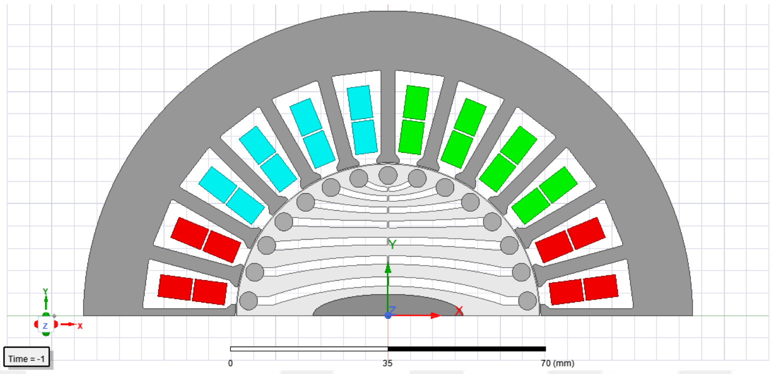

Figure 5.3 Proposed motor structure designed in ANSYS FEA software

According to the optimization results, LS-SynRM with D_{OS} = 5 mm candidates have the highest efficiency, lowest mass, and torque ripple. This result can be explained by the reduced saturation levels in the rotor flux carriers due to the widened flux paths. The structural limit regarding the *Dos* parameter will be investigated in detail in Section 5.3. Effects of the different number of flux barriers on the synchronous reluctance motor efficiency, mass, and torque ripple through the synchronous performance analysis results are provided in Figure 5.4.

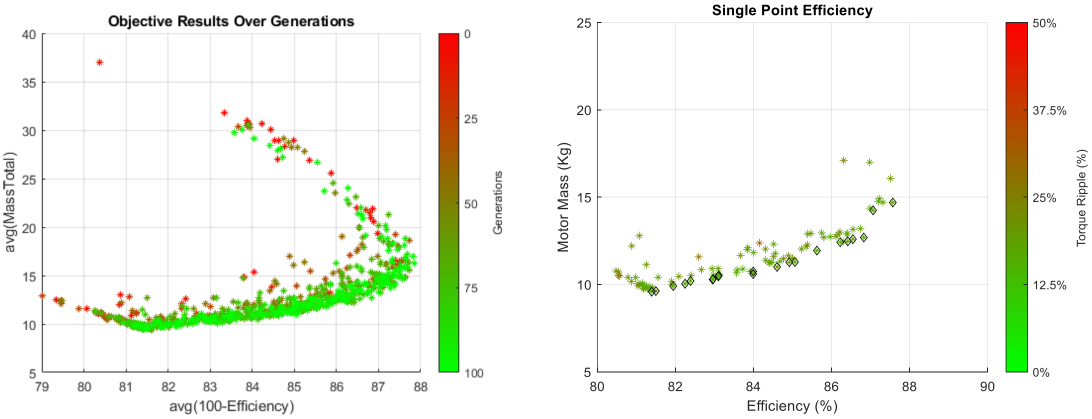

(a)

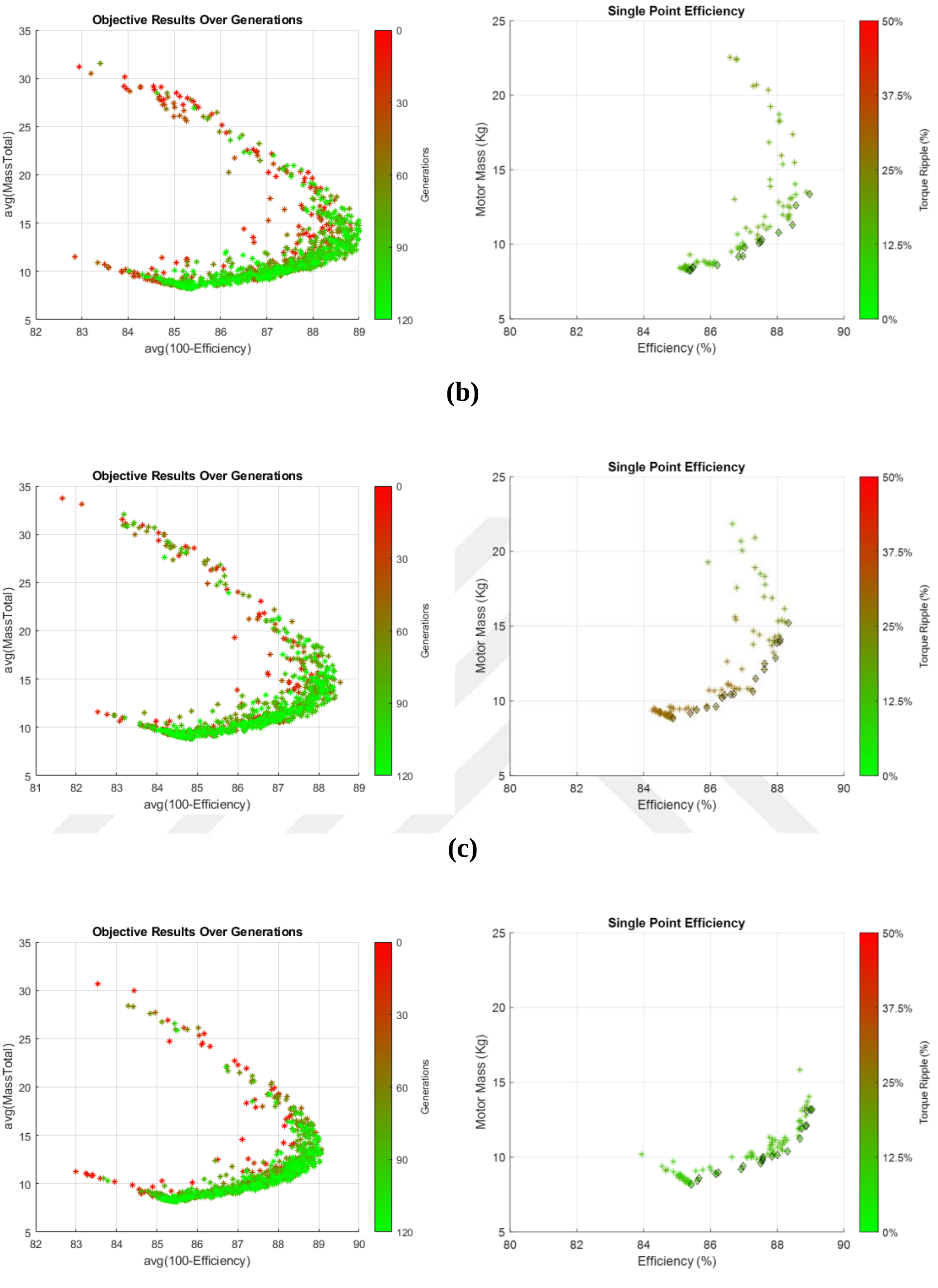

(b)

(c)

(d)

Figure 5.4 Pareto frontier solution sets of oval shaft with (a) 7, (b) 8, (c) 9, (d) 10 flux barriers

All selected candidates from the Pareto frontier are presented in Table 5.4 for comparison. It can be seen that the efficiency winner is the 8 flux barrier design with 89.692 % however, the stack length is observed as high as 185.1 mm. Another candidate is determined as 8 flux barrier design with 88.204 % 149.8 mm. On the other hand, the 7 Flux Barrier design efficiency is 89.240 % with a 158.7 mm stack length. The saliency ratio and the efficiency start to decrease while increasing the number of flux barriers to 9 and 10. Besides, manufacturing and structural integrity problems may occur when the number of flux barriers is increased.

Table 5.4 Performance Comparison

Flux Barrier Number	Efficiency (%)	Mass (kg)	Phase Voltage (V)	Torque Ripple (%)	Stack Length (mm)	Saliency
7	89.240	13.35	329.1	22.31	158.7	7.009
8	89.692	14.57	319.9	19.27	185.1	7.172
	88.204	12.03	332.4	16.88	149.8	6.667
9	88.558	13.25	317.8	17.87	169.2	6.465
10	88.557	12.81	329.3	15.21	159.3	5.999

The candidate motor selection is mainly based on the application. In this study, it is aimed to design an efficient and reduced-sized motor compared to IM for submersible pump applications. Therefore, according to the Pareto results taken from the optimization studies, the design with the 7-flux barrier is superior to the others in terms of efficiency and mass, and the torque ripple is reasonable as the pump motor while synchronous performance analysis.

According to the results obtained from the analysis given in this section, the rest of the study is performed using the design with 7 flux barriers.

5.3 Water Damping Effects

Submersible water pump motors have flooded stators and rotors where the fluid is usually a mixture of water and polypropylene glycol. Damping loss occurs while the rotor is rotating in the fluid like the windage losses in air-cooled motors. As the water mixture is denser than the air, it is expected to yield more loss compared to the windage loss. The related analytical calculations are as follows [72]:

$$P_w = C_d \rho \pi r^4 \omega^3 L \tag{5.4}$$

where P_w is the damping loss, C_d is the skin friction coefficient, ρ is the density of the fluid, r is the radius of the rotor, ω is the angular velocity and L is the rotor length. Here, C_d is calculated as:

$$C_d = \frac{F_d}{qA} = \frac{F_d}{\frac{1}{2}\rho v^2 A} \tag{5.5}$$

where F_d is the drag force, q is dynamic pressure, A is the projected area of the rotor, and v is the velocity of the fluid.

On the other hand, these properties can only be calculated numerically using Computational Fluid Dynamics (CFD) FEA. Considering the different types of slot opening structures, the analyses are carried out and details of the analyses are given in the following section.

5.3.1 Analysis with Different Slot Opening Structures

Since the submersible water pumps have fluid-filled structures, mostly, Polyvinyl Chloride (PVC) insulated magnet wire is preferred. PVC is suitable for applications where the cables expose fluids. Since its chemical stability is higher than the standard copper wire, it is safe and appropriate to use PVC wire in flooded environments. PVC wire diameters are usually larger than the standard magnet wires due to the thick insulation layer. Therefore, slot openings of the submersible pump motor stators are designed to be larger than standard industrial motor stators. Although standard wedges are inserted into the slot openings to keep the coils inside the slot during the operation, they create an indented surface on the airgap side of the stator. The structure with indents causes more liquid fluctuations as shown in Figure 5.5 at the surface and it ends up with dramatically increased damping loss accordingly.

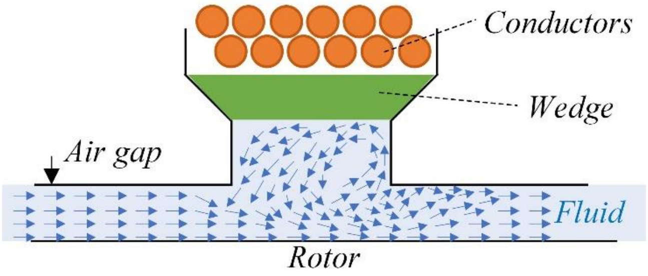

Figure 5.5 Liquid flow in the airgap cavity

In this chapter, damping loss is investigated through CFD analysis for designs with no wedge, standard wedge, and customized no-slotting wedge structures.

5.3.2 Analysis with No Wedge

In this structure, there is no wedge inserted in the slots, so, the liquid in the airgap can go through the windings from the slot openings as shown in Figure 5.5. In order to calculate the fluid damping loss using (5.1), two parameters are required to be obtained through CFD analysis, which are the drag force and dynamic pressure so that the skin friction coefficient can be calculated using (5.2). The 3D fluid body structure used in the CFD analysis is illustrated in Figure 5.6.

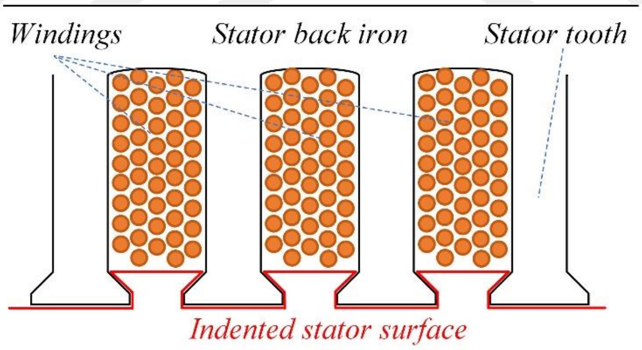

Figure 5.6 Indented stator surface with no wedge inserted into the stator slots

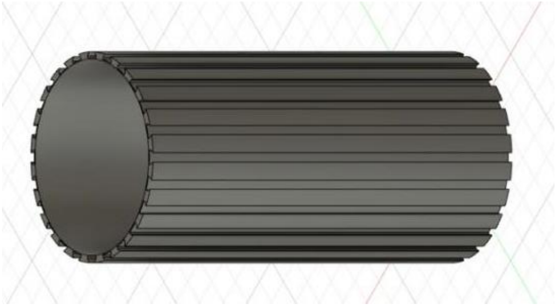

Figure 5.7 3D fluid body geometry with coil slot

According to the analysis results presented in [81], the damping loss varied between 0.155 W and 386.2 W, as the rotor speed varies between 500 rpm and 3000 rpm. It can be clear from the results that the damping loss increases exponentially with speed. Considering that the motor used in the case study has 4 kW output power, almost 10% loss is associated with the fluid damping loss.

Table 5.5 Fluent Analysis Results of the No Wedge Geometry

Speed (Rpm)	Skin Friction Coefficient (Cd)	Damping Loss (W)
500	0.0168	0.155
1000	0.0182	17.28
1500	0.0196	53.36
2000	0.0194	117.2
2500	0.0186	228.7
3000	0.0251	386.2

5.3.3 Analysis with Standard Wedge

Here, standard wedges are inserted into the stator slot openings to keep the coils inside the slot as shown in Figure 5.8. The 3D fluid body structure used in the CFD analysis for this slot opening structure is given in Figure 5.9. As it can be observed from these figures, the indents of the structure with standard wedges are smaller than the previously presented no-wedge structure. Hence, water fluctuation on the indents is less than in the no-wedge structure, and accordingly, the damping losses are smaller compared to the no-wedge form. CFD analysis results are listed in Table 5.6. According to the analysis results, the lowest loss is 0.138 W at 500 rpm and the highest loss is 362.0 W at 3000 rpm which is slightly better than the no-wedge structure.

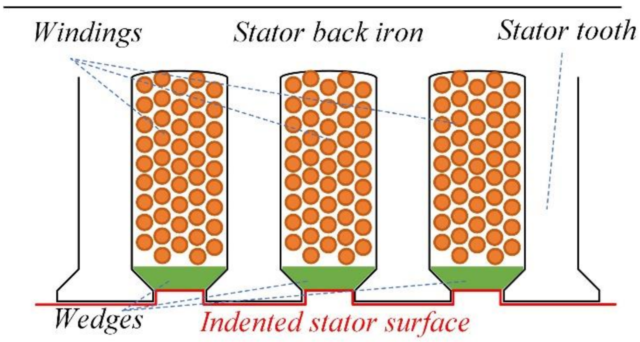

Figure 5.8 Indented stator surface with standard wedges inserted into stator slots

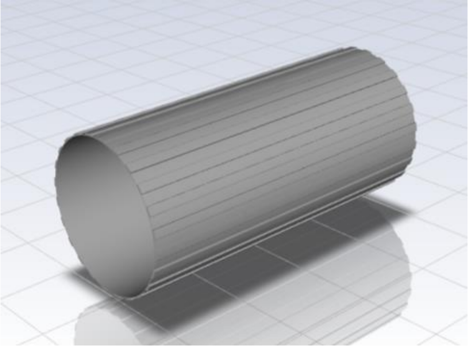

Figure 5.9 3D fluid body geometry with standard wedge structure

Table 5.6 Fluent Analysis Results of the Standard Wedge Geometry

Speed (Rpm)	Skin Friction Coefficient (Cd)	Damping Loss (W)
500	0.0176	0.138
1000	0.0196	13.33
1500	0.0201	46.15
2000	0.0194	105.6
2500	0.0194	206.2
3000	0.0190	362.0

5.3.4 Analysis with Custom No-Slotting Wedge

Here, it is aimed to close the slot openings completely with a customized wedge structure insertion as illustrated in Figure 5.10. The 3D fluid body structure used in the CFD analysis for the smooth slot surface structure is given in Figure 5.11. This way smoothness of the stator's inner surface is maximized and indents are disappeared. Hence, fluid surrounding the rotor structure slides on a smooth surface and this results in a significant reduction in damping loss [81]. Table 5.7 shows the results with a customized no-slotting wedge structure. According to the results, the lowest loss is recorded as 0.138 W at 500 rpm and the highest is 139.9 W at 3000 rpm which is almost 3 times better than the standard-wedge structure.

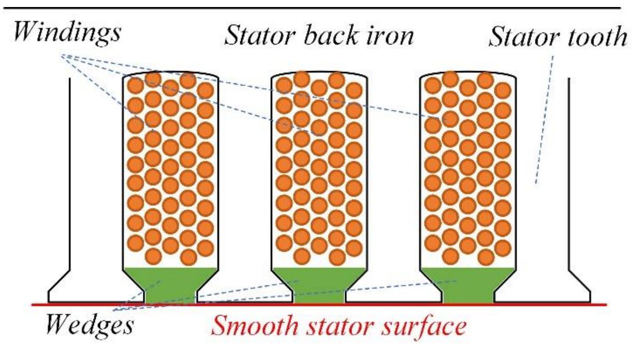

Figure 5.10 **Smooth stator surface with custom no-slotting wedges inserted into the stator slots**

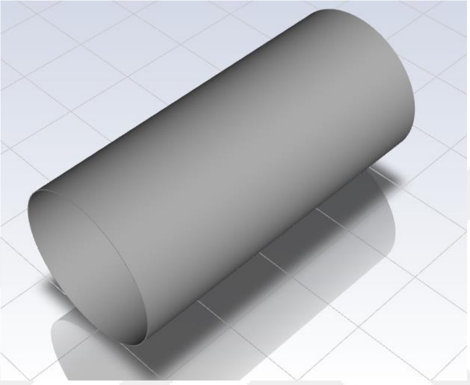

Figure 5. 11 3D fluid body geometry with custom no-slotting wedge structure

Table 5.7 Fluent Analysis Results of the No Slot Geometry

Speed (Rpm)	**Skin Friction Coefficient (Cd)**	**Damping Loss (W)**
500	0.0135	0.110
1000	0.0121	8.230
1500	0.0109	25.01
2000	0.00985	53.58
2500	0.00913	96.99
3000	0.00866	139.9

5.3.5 Comparison and Discussion

According to this analysis, one can conclude that the damping loss is at its minimum when there are no indents on the stator surface, and it increases dramatically even with small surface indents. The depth of the indents affects the damping loss, but the loss variation is slight compared with the loss on the smooth surface.

A summary and a comparison of the losses associated with the slot opening structures are presented in Table 5.8. Additionally, the scenario; which ignores the damping loss of the fluid-filled motor and assumes that the machine works as in the air; is analyzed and the results are included in the comparison given in Table 5.4. Since the density of the fluid (mixture of water and polypropylene glycol) filled inside the motor is 998.2 kg/m^3 while air density is 1.2250 kg/m^3, the difference between the losses is significant. According to the results, without inserting any wedge into the slot openings of the stator the damping loss is as high as 386.2 W while the windage loss is only 0.69 W; with the insertion of the standard wedge into the slots the damping loss is calculated as 362 W while the windage loss is 0.56 W. Hence, it can be concluded that there is a slight difference between the designs without the wedge and then with the standard wedge where the standard wedge design is slightly better. However, the creation of a smooth surface by designing a custom wedge that closes the openings and eliminates all the indents reduces the damping loss significantly to 139.9 W. Also, windage loss appears as only 0.33 W, which is the lowest windage loss compared to the other two structures.

Table 5.8 Different Slot Opening Structures Results at 3000 rpm

Geometry	Water		Air	
No Wedge	Skin Friction Coefficient (Cd)	0.0251	Skin Friction Coefficient (Cd)	0.0302
	Fluid Density (kg/m^3)	998.2	Air Density (kg/m^3)	1.2250
	Damping Loss (W)	386.2	Windage Loss (W)	0.6900
Standard Wedge	Skin Friction Coefficient (Cd)	0.019	Skin Friction Coefficient (Cd)	0.0245
	Fluid Density (kg/m^3)	998.2	Air Density (kg/m^3)	1.2250
	Damping Loss (W)	362.0	Windage Loss (W)	0.5600
Custom Wedge	Skin Friction Coefficient (Cd)	0.0087	Skin Friction Coefficient (Cd)	0.0142
	Fluid Density (kg/m^3)	998.20	Air Density (kg/m^3)	1.2250
	Damping Loss (W)	139.90	Windage Loss (W)	0.3300

The performed fluid damping loss analyses are done for a 2-pole, 4 kW LS-SynRM. It can be seen from the results that the damping loss has a significant impact on the efficiency as it may go as high as 10% of the machine`s output power. This loss component can be reduced significantly by providing a smooth surface for the fluid to slide between the rotor and stator surfaces. This can be done by customizing the slot wedge structures to avoid indentations on the stator surface. For any case, a CFD analysis should be performed to estimate this loss component for estimating the machine performance and machine dynamics accurately.

According to the results, the design with the custom wedge reduces the damping loss to 139.9 W. As a result of this investigation two important matter is pointed out:

- According to the analysis results it is observed that the damping loss is almost 420 to 650 times the windage loss for the cases with different stator slot structures investigated in this study. Therefore, the fluid damping effect cannot be assumed as windage loss like in the air-cooled motors in flooded motor structures and cannot be ignored for estimating the machine performance accurately.
- Since the exitance of the indents on the stator surface increases the damping loss extremely, making the stator inner surface as smooth as possible and eliminating the indents reduces the damping loss of the fluid-filled motors significantly.

5.4 Structural Analysis of the Oval Shaft

In this thesis study, a 2 pole, 4 kW, 6 inches diameter LS-SynRM as a submersible water pump motor is designed and optimized with a new oval shaft structure [82]. Here, it is aimed to improve the machine performance by widening the flux path on the rotor by narrowing down the shaft on the q-axis. In this way, a wider d-axis flux path is obtained, and the d-axis inductance is increased. Therefore, the saliency ratio L_d/L_q and the inductance difference L_d-L_q are increased. As a result, the saliency torque and efficiency are improved. However, at this point, it is important to consider the effects of the new shaft design on structural integrity, vibrations, and deformation of the rotor. Therefore, the structural properties of the rotor have to be investigated during the design stage carefully. In order to determine the safe maximum shaft dimension limits, a series of structural analyses are performed using FEA. Considering the manufacturing tolerances, an axial misalignment is defined to analyze the natural frequencies and vibration behavior of the rotor. Also, considering the initial torque being multiple times the rated torque, a shear stress analysis is conducted to verify the new shaft structure which will guarantee its structural integrity.

5.4.1 Structure of 2 pole LS-SynRM

LS-SynRM is a hybrid technology that combines the features of squirrel cage IM and SynRM. In the rotor, there are several flux barriers for the reluctance torque generation and conductor bars that are responsible for the induction torque production during the start-up. Considering the pump load has an exponential relationship with the speed, the submersible pump motor starts up with a light loading and reaches the rated loading condition as the speed reaches the synchronous speed. In order to generate enough torque and synchronize, the induction torque should be sufficient. The cross-sectional area of the rotor conductor bar has an effect on the synchronization; hence, it should be calculated carefully. Additionally, the distance between the bars and the airgap should be chosen to aid the synchronization [83]. Once the LS-SynRM reaches synchronous speed, the reluctance torque takes over the torque production and the machine operates as a synchronous motor in the steady state. The bar size required to generate enough startup torque makes it difficult to obtain decent $L_d - L_q$ and L_d/L_q since the flux paths are narrowed. Nevertheless, the flux carrier and barrier sizes should be optimized for the best performance.

When the flux barrier thickness is increased, the q-axis inductance will be reduced, accordingly, L_d/L_q and $L_d - L_q$ will increase. However, since the carrier thickness is reduced by increasing the flux barrier thickness the d-axis inductance will be decreased correspondingly. Therefore, there is a tradeoff between the thickness of the flux barriers and carriers. An optimization study should be made to find out the optimum thickness for both flux barriers and carriers. This process is even harder for designing 2 pole machines due to the limited space available on the q-axis of the rotor as shown in Figure 5.12a.

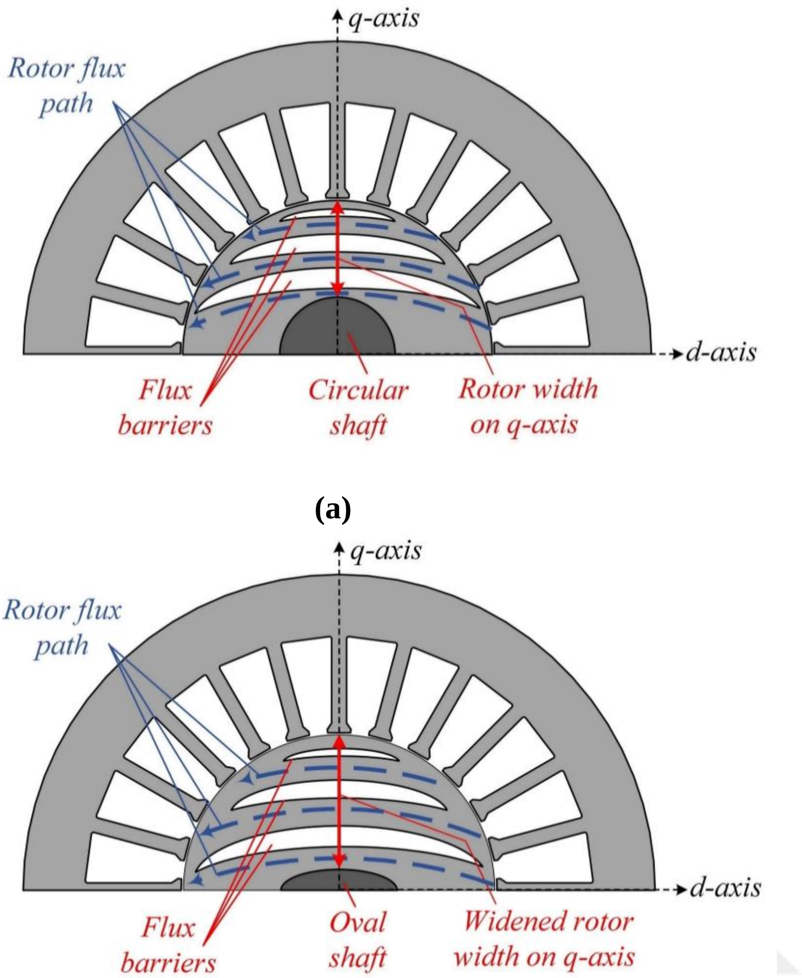

(a)

(b)

Figure 5.12 2 pole SynRM with (a) circular and (b) oval shaft

In this study, widened rotor width on the q-axis by narrowing down the shaft to its physically possible minimum size is proposed. This operation is illustrated in Figure 5.12b. This way, a larger path is provided for the rotor flux. Hence, a higher d-axis inductance, better saliency, and higher reluctance torque are obtained.

5.4.2 Rotor Dynamics of the Proposed Oval Shaft LS-SynRM

Here, the LS-SynRM with the proposed oval shaft is structurally analyzed while operating at the rated speed to determine the safe limits for the motor to operate without significant deformation or vibration. Structural analysis of the motor is carried out in 3 stages. First, modal analysis is performed to determine the first natural frequencies of different size shaft structures. This way, the safe limit for the shaft size reduction is determined to avoid undesired vibrations due to resonance. Second, harmonic analysis is made to determine the maximum stress and deformation considering the manufacturing nonidealities on the rotor geometry. Lastly, a static structural analysis is done to verify whether the shrank shaft geometry would maintain its integrity under the startup torque which is 3-5 times higher than the rated torque.

The first step in the analysis is to establish a 3D geometry. Then, the connections between parts are defined as well as the points that held this structure in place. This shape is composed of five parts, upper shaft (circular), lower shaft (circular), middle shaft (oval), squirrel cage rotor conductors, and the main rotor body as shown in Figure 5.13. The shaft parts are defined as welded together and have a high friction connection with the main rotor body. The cage is also fitting tightly to the main rotor body thus all these pieces are bonded to each other. Two sliding bearings are holding the rotor in place. These bearings are connected to the fixed motor housing.

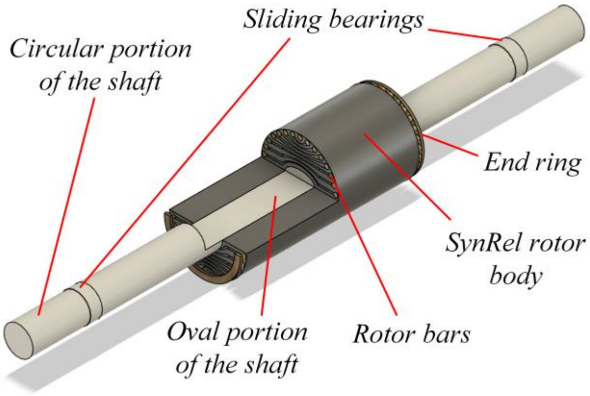

Figure 5.13 Structure of the rotor geometry

The modal analysis is performed to find the natural vibration modes of the rotor geometry [84]. According to the modal analysis, it is possible to see how the material behaves at different excitation frequencies. Since the main purpose is to explore how much the shaft can be reduced, analyses are done for D_{OS} (measurement of circle shaft size reduction in q-axis) between 0 and 10 mm. Here, possible axis misalignment due to the manufacturing process is also considered and included in the analysis. Although the maximum excitation frequency can be 60 Hz for a line start machine, the analysis is performed up to 70 Hz. The modal analysis results are presented in Table 5.9 with 0.1 mm misalignment at 70 Hz. According to the results, the first natural frequency (1NF) occurs at 259 Hz while the shaft is a regular 25 mm diameter circle. When D_{OS} is increased with 2 mm steps, the 1NF of the rotor tends to decrease.

Table 5.9 Modal Analyses Results

D_{OS} (mm)	First Natural Frequency (1NF) (Hz)
0	259.07
2	239.08
4	213.75
6	183.56
8	146.60
10	99.82

In this study, the safe operating limit for the 1NF is assumed as two times the excitation frequency, i.e., if the 1NF is above two times the excitation frequency, excessive vibrations and deformations can be avoided. When the D_{OS} is taken as 10 mm, 1NF of the rotor is observed as 99.82 Hz which is less than two times the excitation frequency. Based on these results, D_{OS} limit is decided to be 8 mm as the 1NF occurs at 146.6 Hz.

Later, the harmonic analysis is carried out to determine the maximum stress and deformation of the rotor. Here, the possible undesired effects of the manufacturing process are also considered axis misalignment. Hence, the analysis is performed for a range of axial misalignment values. In this analysis, a rotational movement is defined to the rotor body. Using the centrifugal force, axial misalignment, and center of gravity, the software calculates the stress and deformation of the matter in the given excitation frequencies. According to the results given in Table 5.10, as D_{OS} increases the equivalent stress and the maximum deformation increases exponentially. When it is increased from 8 mm to 10 mm, an excessive increase is recorded both on the equivalent stress and the maximum deformation. Hence, D_{OS} = 8 mm is selected as the acceptable limit as the calculated maximum deformation is 0.0389 mm as shown in Figure 5.14, which is not getting anywhere near the airgap length of the motor which is 0.35 mm. Figure 5.15 shows that maximum stress occurs at the junction of the circular and the oval shaft region for D_{OS} = 8 mm.

In order to operate without losing structural integrity, the maximum stress on the geometry should not exceed the yield stress of a certain type of material. Since the rotor body is made from a type of electric steel, the maximum stress should not be exceeding 350 MPa [85]. The results show that the equivalent stress on the rotor when D_{OS} is equal to 8 mm is only 9.031 MPa which also supports that the design with D_{OS} = 8 mm is safe and acceptable.

Table 5.10 Harmonic Analyses Results

D_{OS} (mm)	Equivalent Stress (MPa)	Maximum Deformation (mm)
0	2.717	0.0074
2	4.945	0.0122
4	5.457	0.0159
6	6.708	0.0225
8	9.031	0.0389
10	26.776	0.1196

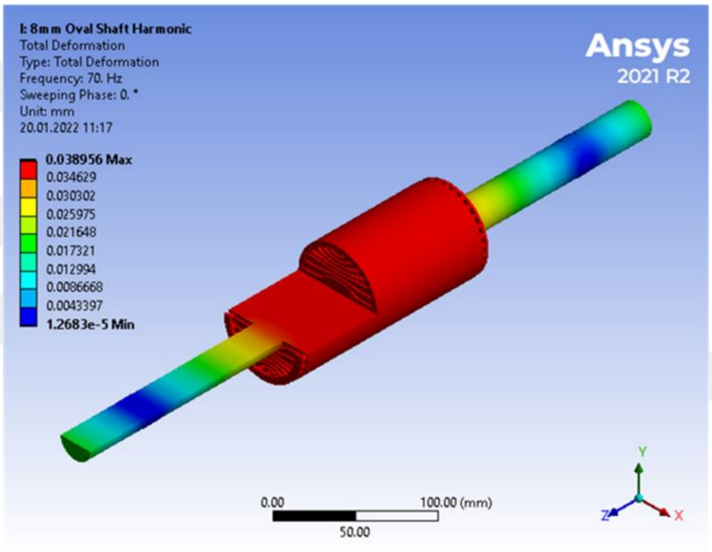

Figure 5.14 Total deformation of the proposed LS-SynRM with D_{OS} = 8 mm

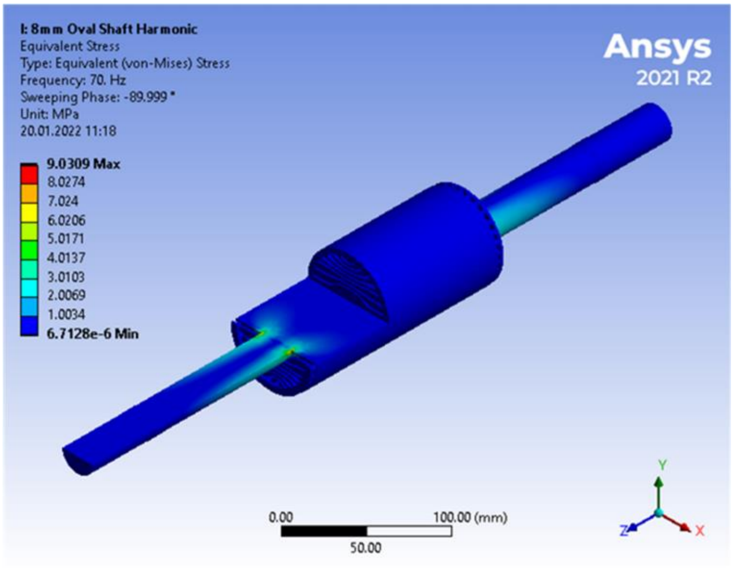

Figure 5.15 Equivalent stress of the proposed LS-SynRM with D_{OS} = 8 mm

Lastly, the shear stress analysis is performed under 5 times the rated torque condition while the shaft is motionless. Although the previous analysis results show that shrinking the shaft by 8 mm is acceptable, the shear stress analysis is done for the D_{OS} values of 0, 5, and 8 mm to see the effects of the shaft size reduction. According to the analysis results, the shear stress increases gradually while D_{OS} is increased. Here, the maximum shear stress is recorded as 104.47 MPa while the equivalent stress is 182.02 MPa, and total deformation is 0.2 mm for D_{OS} =8 mm. Therefore, the results are again in acceptable boundaries even under 5 times the rated torque applied to the shaft. The related analysis results are tabulated in Table 5.11, where the total deformation and equivalent stress along with the shear stress are presented.

Table 5.11 Analyses Results under Five-Times of the Rated Torque

Analysis Type D_{OS} (mm)	Maximum shear stress (MPa)	Equivalent stress (MPa)	Total deformation (mm)
0	49.970	86.555	0.0224
5	50.363	87.232	0.0227
8	104.470	182.020	0.2000

As a result of the structural analyses, it can be concluded that it is acceptable and safe to narrow down the shaft on the q-axis up to 8 mm.

5.5 Induction Machine Analysis

Due to the features like robustness, low cost, and line start capability, Induction Machine (IM) are generally the first choice for pump applications. However, the major issue with the IMs is they work with low efficiency, especially at low and medium power levels in submersible pump applications. Here, the FEA of a 4 kW, 6-inch diameter commercial submersible water pump IM which has the same frame size as the proposed oval shaft LS-SynRM is performed. The geometric quantities of the mentioned IM that are required for the analysis are measured manually in addition to the gathered available information in the datasheet. Specifications of the IM are given in Table 5.12. The mass of the machine is calculated as 14.8 kg. According to the analysis results, the efficiency of the commercial IM is recorded as 70%, 68%, 61%, and 45% when the loading is 100%, 75%, 50%, and 25%, respectively.

Table 5.12 Specifications of the Commercial IM

Design Parameter	Value	Units
Number of phases	3	-
Output power	4	kW
Number of poles	2	-
Number of stator slots	24	-
Number of rotor bars	18	-
Line-to-line voltage	400	V
Speed	2792	rpm
Stator outer diameter	136	mm
Number of stator slots	24	-
Rotor outer diameter	67.8	mm
Stack length	150	mm
Airgap length	0.6	mm

5.6 Motor Optimization Including New Findings and Performance Comparison Results

In this section, the proposed oval shaft LS-SynRM optimization is updated by including the damping effect and structural integrity results. According to the ANSYS CFD analysis, the water damping losses are changing depending on the stator indent openings and the stack length. Also, the number of flux barriers is determined as 7 depending on the synchronous analysis results. Moreover, based on the structural analysis, shaft size can be reduced up to 8 mm, therefore, *Dos* is selected as 8 mm for further electromechanical analyses of the motor. The proposed MODE optimization steps including geometric parameters, objectives, and constraints that are given in Section 5.1, are performed with new findings and the results are updated accordingly.

Here, the geometric optimization of the motor with 7 flux barriers is carried out with D_{OS} being 0 mm (circular), 5 mm (oval), and 8 mm (oval) to see the advantage of the proposed structure. The steady-state operations are performed at 3000 rpm while the machine is generating 12.75 Nm output torque. Then, the candidate motor designs in the Pareto frontier are tested for their synchronization capability under the rated loading condition. Finally, these results are compared with the classical, same size, 4-kW IM used in submersible water pump applications.

5.6.1 Steady State Synchronous Operation

The optimization study is performed at 3000 rpm while the machine is generating 12.75 Nm output torque. The optimization results are presented in Figure 5.16. Here, the candidates that satisfy all the constraints are superior to the others in terms of efficiency, mass, and torque ripple. They are also called dominant results that are represented with diamond shapes.

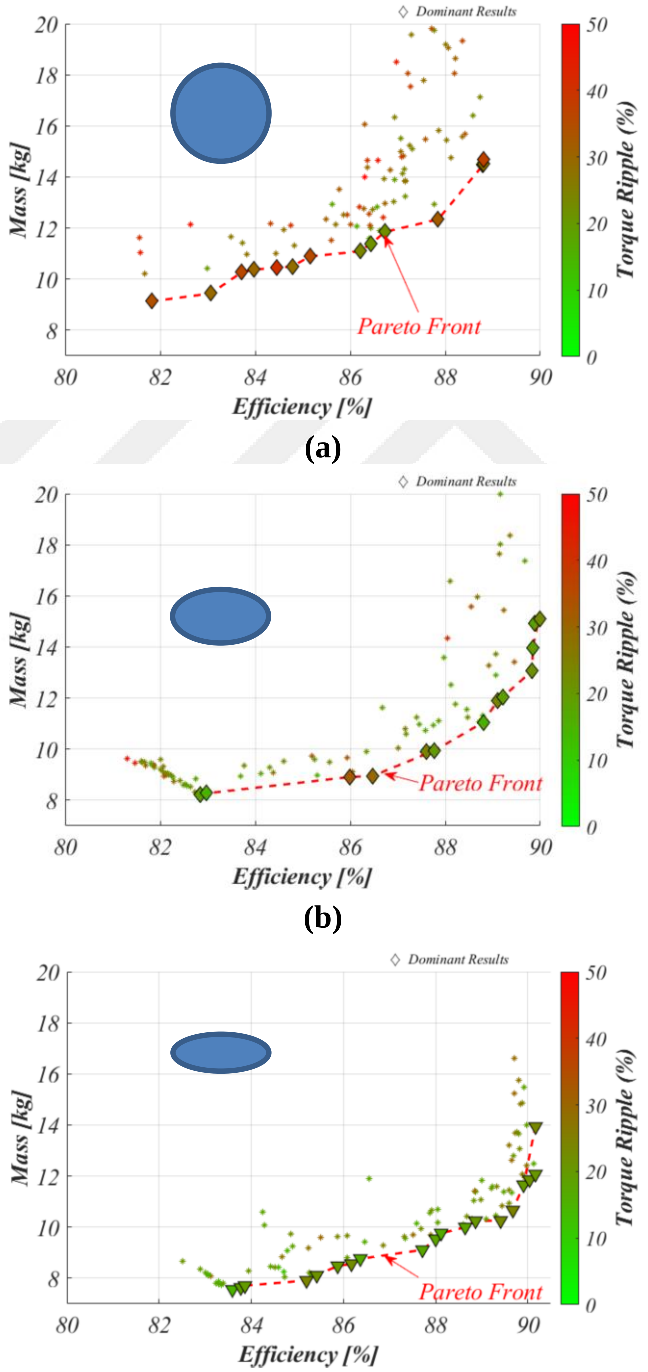

(a)

(b)

(c)

Figure 5.16 Pareto frontier solution sets of (a) circular shaft, (b) oval shaft with D_{OS} = 5 mm, and (c) oval shaft with D_{OS} = 8 mm designs

The results for the regular circular shaft are shown in Figure 5.16a where the maximum efficiency is recorded as 85.81 % with a motor mass of 14.68 kg. The lightest candidate is 9.13 kg and has 81.82 % efficiency. The minimum and maximum torque ripple are recorded as 21.7%, and 40.4%, respectively.

The results for the new oval shaft structure with D_{OS} = 5 mm are given in Figure 5.16b. Here, the maximum efficiency is recorded as 86.65 % with a motor mass of 14.9 kg. The lightest candidate is 8.24 kg and has 82.83 % efficiency. The minimum and maximum torque ripple are recorded as 15.1%, and 32.0%, respectively. As it can be seen from the figure, not only the Pareto front has moved to the right lower corner compared to the circular shaft Pareto front but also the torque ripple is reduced.

The results when the D_{OS} is increased to 8 mm are given in Figure 5.16c. The maximum efficiency reaches up to 87.06 % with a motor mass of 14.24 kg. The lightest candidate is 7.56 kg and has 83.59 % efficiency. The minimum and maximum torque ripples are recorded as 15.0%, and 24.3%, respectively. It can be observed from this figure that the Pareto front has further moved to the right lower corner and the maximum torque ripple is reduced. This proves that the candidates in this condition have better performance than the candidates that have D_{OS} = 5 mm or circular shafts.

Figure 5.17 shows the difference in the quality of the Pareto frontier solution sets clearly.

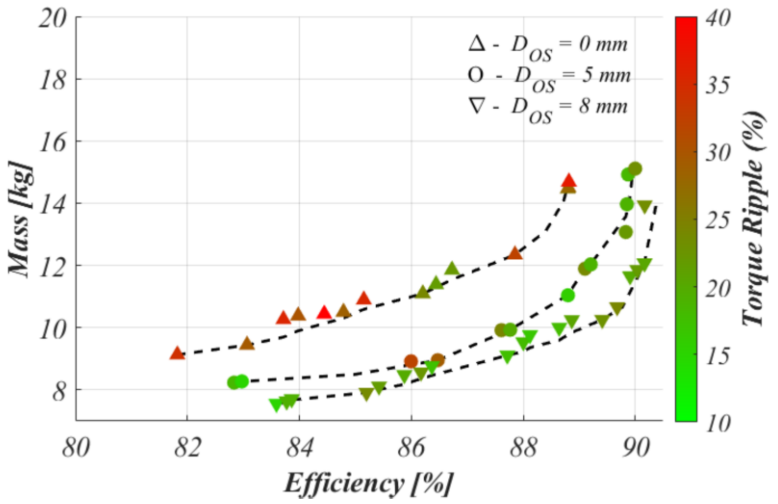

Figure 5.17 The comparison of the circular and oval shaft designs

According to these results, including the water damping effect (170 W for the stack length is around 150 mm) LS-SynRM with D_{OS} = 8 mm candidates have the highest efficiency, lowest mass, and reasonable torque ripple.

5.6.2 Synchronization Capability

The start-up and synchronization capability of the candidate motor designs are investigated to make sure that they can start up and synchronize under the pump load. Figure 5.18 shows the acceleration plots of all the candidate designs. These acceleration curves are obtained with the corresponding damping and inertia values. The inertia of the candidate designs is calculated by considering the rotor is a solid cylindrical mass [80].

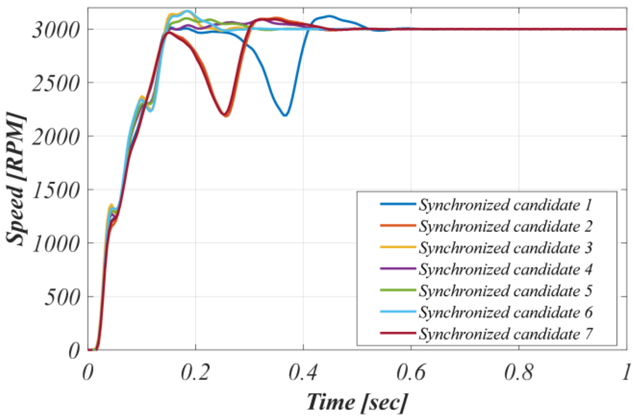

Figure 5.18 Start-up and Synchronization capability of the proposed or candidate LS-SynRM design(s)

After eliminating the candidates that cannot synchronize under loaded conditions, the results as given in Table 5.13 show that the proposed oval shaft LS-SynRM efficiency can go up to 87.06 % when D_{OS} is selected as 8mm.

Table 5.13 Optimized parameters for synchronized candidates

Optimized Parameters	Synchronized Design #						
	1	2	3	4	5	6	7
a_{BR}	0.00	0.00	0.42	0.00	0.79	2.19	4.29
l_{IC}	1.00	1.75	1.99	1.80	1.71	2.62	2.41
k_B	0.49	0.51	0.41	0.55	0.44	0.48	0.44
k_C	0.68	0.67	0.68	0.67	0.69	0.68	0.70
k_R	0.73	0.81	0.90	0.90	0.61	0.90	0.90
k_{REC}	0.71	0.71	0.75	0.59	0.72	0.73	0.72

***J* [A/mm2]**	5.77	6.07	4.88	5.00	5.15	5.28	6.37
I_{peak} [A]	13.76	13.96	13.10	13.51	13.73	13.91	14.30
η [%]	86.68	86.41	87.06	87.00	86.94	86.01	85.87
Mass [kg]	13.67	13.26	14.24	14.96	13.86	13.66	13.25
Torque Ripple [%]	24.29	22.82	23.47	20.47	21.72	20.03	20.59

5.6.3 Comparison

In the case that D_{OS} is 8 mm, the damping losses are calculated as around 170 W for 150 mm stack length, the copper loss is calculated as 378 W (while *Rph* is 1.47 ohm) and the core losses and stray losses are assumed as 50 W. Therefore, the total loss is calculated as 598 W. The total loss was calculated as 384 W while assuming the damping loss is negligible like the windage loss and Dos was 5 mm. In that case, the efficiency was calculated as 89.24 %. Later, the efficiency dropped to 86.95 W.

Being different than the machines having 4 or more poles, the rotor flux path is disturbed by the shaft in the 2 pole machine structure. To improve the 2 pole LS-SynRM performance, the circular shaft is replaced with an oval shaft structure by narrowing down the shaft on the q-axis. This way, it is aimed to widen the flux paths to improve motor performance. In order to find the safe dimensional limits and avoid undesired deformations and vibrations, a set of structural analyses is carried out. Later, an optimization study is done targeting the highest efficiency and minimum motor mass via MODE algorithm for the regular circular shaft, 5 and 8 mm narrower oval shaft structures. The resulting candidate designs are then tested for their synchronization capabilities and the ones that cannot synchronize are eliminated. Results show that candidate machines with 8 mm narrowed oval shaft is superior to ones with 5 mm narrowed oval shaft and regular circular shaft in terms of efficiency, motor mass, and torque ripple. The maximum efficiency for the 8 mm narrowed oval shaft design is recorded as 87.06 % with a motor mass of 14.24 kg, and torque ripples between 15.0% and 24.3% whereas the maximum efficiency for the 5 mm narrowed oval shaft design is recorded as 86.95 % with a motor mass of 14.9 kg and torque ripples between 15.1%, and 32.0% and the maximum efficiency for the circular shaft design is recorded as 85.81 % with a motor mass of 14.68 kg and torque ripples between 21.7%, and 40.4%. When the proposed LS-SynRM is compared to the same size commercial IM for the same submersible pump motor applications, it not only makes a difference of more than 15 points betterment in efficiency but also challenges the position of IM that holds in the market. On the other hand, PMSMs are almost 3 times more costly than the LS-SynRM with a questionable couple of points improvement on the efficiency while requiring dependency on permanent magnets and a motor driver which comes at an additional cost and complexity. Therefore, this study proves that the proposed LS-SynRM is a new rival for all types of motors in the submersible pump market because of its high efficiency, lightweight, simplicity, ruggedness, driverless/line start property, no permanent magnet requiring structure, and low investment and running costs.

5.7 Stator Windings

In this section, an investigation of the synchronous performance of a 2 pole, 4 kW, LS-SynRM with various winding structures is investigated. Single-layer, several versions of double-layer, and triple-layer winding structures with an uneven number of turns on each coil are applied to a 24-slot stator [86].

5.7.1 End Winding Length and Magneto-Motive Force THD Investigation

The negative influence of air-gap Magneto-Motive Force (MMF) harmonics in an electrical machine has been covered in the literature. The harmonics in the air-gap MMF are called space harmonics. Air-gap flux with space harmonics induces excessive copper and core losses in addition to vibration and acoustic noise [87–89]. A proper configuration of stator windings with reduced winding MMF space harmonic content leads to improve overall machine performance significantly [90–93]. Since the space harmonics are inherently caused by the harmonic distortion of a specific winding distribution, having more sinusoidal winding MMF provides less torque ripple and a higher power factor. In the literature, reducing the MMF harmonics is subject to the optimization problems of the two major winding types; distributed windings [90,94], and fractional-slot concentrated windings (FSCWs) [93,95]. Some topologies of FSCW are being developed to reduce or even cancel dominant harmonics, including multilayer structures [96], dual multiphase winding configurations [97], and unequal turns per coil winding configurations [96,98]. Moreover, FSCW design optimizations are integrated the some of the winding studies to maximize the airgap MMF fundamental term and minimize the MMF Total Harmonic Distortion (THD) [99–101].

Recently, researchers have reported several studies on SynRMs with concentrated windings [102]. Non-overlapping, short end-turn length, high slot fill factor, and easier manufacturing are the important advantages of concentrated windings. However, existing works on concentrated windings reveal that air-gap MMF harmonics are increased in these winding structures. These space harmonics lead to a higher torque ripple, reduced power factor, increased core and copper losses, and accordingly lower efficiency [102,103]. To obtain reduced space harmonics a variety of three-phase winding configurations are proposed in [96,104,105]. Although the 5th order harmonic helps improve the torque production, additional 7th, 17th, and 19th order harmonics that appear degrade the performance of the machine. Therefore, the machine pole number and number of stator slots had to be increased [96], [105]. However, the fundamental frequency and the core loss increase while the power factor reduces with an increased number of poles accordingly [106]. In addition to distributed windings and FSCWs, another type of multi-layer (ML) winding configuration for SynRM is reported in [107], which reduces torque ripple and improves the power factor compared to the conventional winding structure. This winding scheme provides shorter end winding lengths and provides a low MMF THD while keeping the same four-pole structure as in the single layer windings. However, there is only triple layer winding structure where all the slots contain all three phase windings is investigated, while the double-layer configurations that may be favorable are not considered.

A two-step optimization study is performed namely winding optimization and geometry optimization. First, the THD and end winding scores (EWS) of all the winding structures are calculated and optimized with the MODE algorithm to get Pareto frontier designs. The EWS is an indicator that quantifies the end winding length of the initial designs. The result of this optimization provides a Pareto front solution set showing the tradeoff between the THD and the EWS for each winding configuration by distributing the coil number of turns in different percentages. Later, three different designs are selected from the obtained Pareto front for each winding structure and a geometric rotor optimization is performed for a seven-flux barrier rotor structure. Here, maximum efficiency and minimum motor mass are selected as objectives. Following the rotor optimizations, a new set of Pareto frontier designs are obtained, which are provided insights into how the machine efficiency and motor mass are affected by the MMF harmonics and shorter end windings. However, it is a tedious process to distinguish the quality of each design`s Pareto frontier solution set without quantifying them. Therefore, a score-based quality assessment method is proposed to quantify the quality of the Pareto frontiers. Hence, a score-based comparison is provided with two scores; one of them is the average of overall efficiency per mass and the other is the average of inverse torque ripple for each Pareto frontier. The results show that for all winding configurations, rather than reducing the end winding length reducing the THD of the MMF leads to higher quality Pareto fronts, and although the triple-layer winding has the best results, from the manufacturing standpoint, it is more practical to use a double-layer version which has a similar performance to the triple-layer winding structure. As a result, the efficiency of the SynRM can go up to 88%, and 87% with triple and double-layer windings, respectively. The machine efficiency class is improved from standard efficiency IE1 to premium efficiency IE3 compared with the conventional IMs at the same power level.

5.7.2 Multi-Level Winding Concepts

In 2-pole AC machines, the standard winding structure has a long throw that causes a high end winding resistance and has a high harmonic content on the winding MMF. It is possible to improve the machine efficiency by reducing the harmonic contents of the stator field, but this may lead to an increased end winding resistance and cancel out all the benefits gained through THD improvement. This is a tradeoff and needs to be analyzed further. In order to generate an MMF that has low harmonic distortion, while shortening the end winding conductor length, the uneven number of turns method is introduced in [96,98]. However, for a 24-slot, single-layer winding configuration, there are only 2 coils in a pole that does not have enough freedom to adjust the number of turns and slot locations for each coil to improve the THD and the end winding resistance.

At this point, double-layer and triple-layer configurations come into the scene as it is possible to distribute the coils and vary the number of turns to decrease the winding MMF harmonics and end winding resistances [86]. In this study, the conventional even number of turn single-layer, 4 different versions of double-layer, and a triple-layer uneven number of turn winding configurations are considered for a 24-slot stator as presented in Figure 5.19.

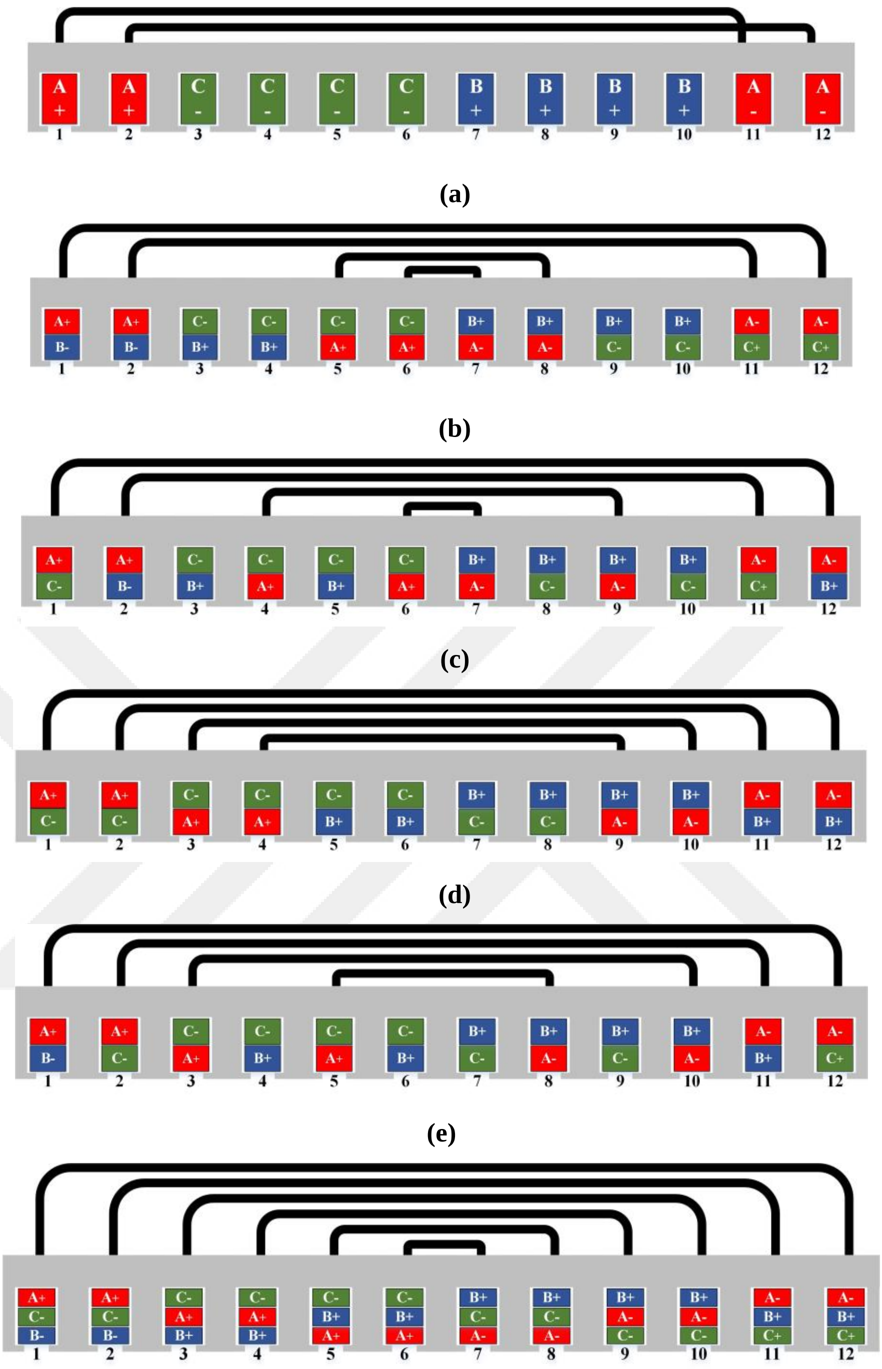

(f)

Figure 5.19 Winding layout of the (a) single-layer, (b) double-layer version 1, (c) version 2, (d) version 3, (e) version 4, and (f) triple-layer windings

5.7.3 Winding Function Analysis

AC winding factor, k_{wv}, is expressed as the product of the winding distribution factor, k_{dv}, and the pitch factor, k_{pv}, for the v^{th} harmonics. Fluxes of distributed and same pitch coils do not intersect directly but intersect indirectly with a phase shift as in (5.6) for a single-phase. Here, α is the phase shift angle ($\alpha = \pi/mq$, where m is machine phase number), q is the number of slots, W is the coil span and τ_p is the pole pitch. (5.7) shows the total number of turns per phase which is expressed as N_{ph}. The winding factor k_{wv} in (5.8) describes the stator MMF harmonics and MMF expression can be written as in (5.9). When the MMFs from all coil sets are in phase, k_{dv} will be counted as 1 for each harmonic. Hence, the peak harmonics generated by three phases can be represented in (5.10) and (5.11).

Here, v is the harmonic order number that is equal to (1 ± 6c), where c is a natural number for the MMF distribution of a balanced three-phase machine, n is the number of coils, N_n is the number of turns for the coil group, q_n is the coil groups per pole pair, p is the number of pole pairs, i_s is the peak value of the winding current.

$$k_{dv} = \frac{\sin\,(v\frac{q\,\alpha}{2})}{q\,\sin\,(v\frac{\alpha}{2})} \tag{5.6}$$

$$N_{ph} = \sum_{n} N_n q_n \tag{5.7}$$

$$k_{pv} = \frac{1}{N_{ph}} \sum_{n} N_n q_n \sin\,(v\,\frac{2n-1}{\tau_p}\frac{\pi}{2}) \tag{5.8}$$

$$k_{wv} = k_{pv} k_{dv} \tag{5.9}$$

$$F_{st}^{v} = \frac{3}{\pi v}\frac{N_n}{p} k_{wv} i_s \tag{5.10}$$

$$F_{st}^{v} = \frac{3}{\pi v}\frac{N_{ph}}{p} k_{pv} i_s \tag{5.11}$$

5.7.4 Harmonic Analysis

As mentioned before, achieving a low THD winding MMF with single-layer winding is a quite challenging task as there are only two coils in a 24-slot 2-pole configuration. In Figure 5.20a, the winding MMF distribution and its Fourier transform along with the related THD value are provided for a single layer winding configuration and an even number of turns. As the layer count increase, there is more freedom for adjusting the coil positions and the number of turns to get a low THD. For the same slot-pole configuration, there are 4 coils in a pole that reaches the peak MMF value in four steps. Taking the uneven number of turns into account, the MMF distribution can even have a less harmonic content. In figures, 5.20b, 5.20c, 5.20d, and 5.20e, different double-layer winding configurations' MMF distributions, Fourier transforms, and THDs are provided. It can be seen that the THD values are lower compared with the single-layer configuration. In Figure 5.20f, the results of the triple-layer configuration are presented where the best THD value is achieved. However, having a low harmonic content stator field may not be the optimal solution as having multiple layers may lead to longer end winding conductor length and higher phase resistance. This could result in lower efficiency. It is clear that there is a tradeoff between the MMF THD and end winding resistance. There should be an optimization process to analyze this phenomenon.

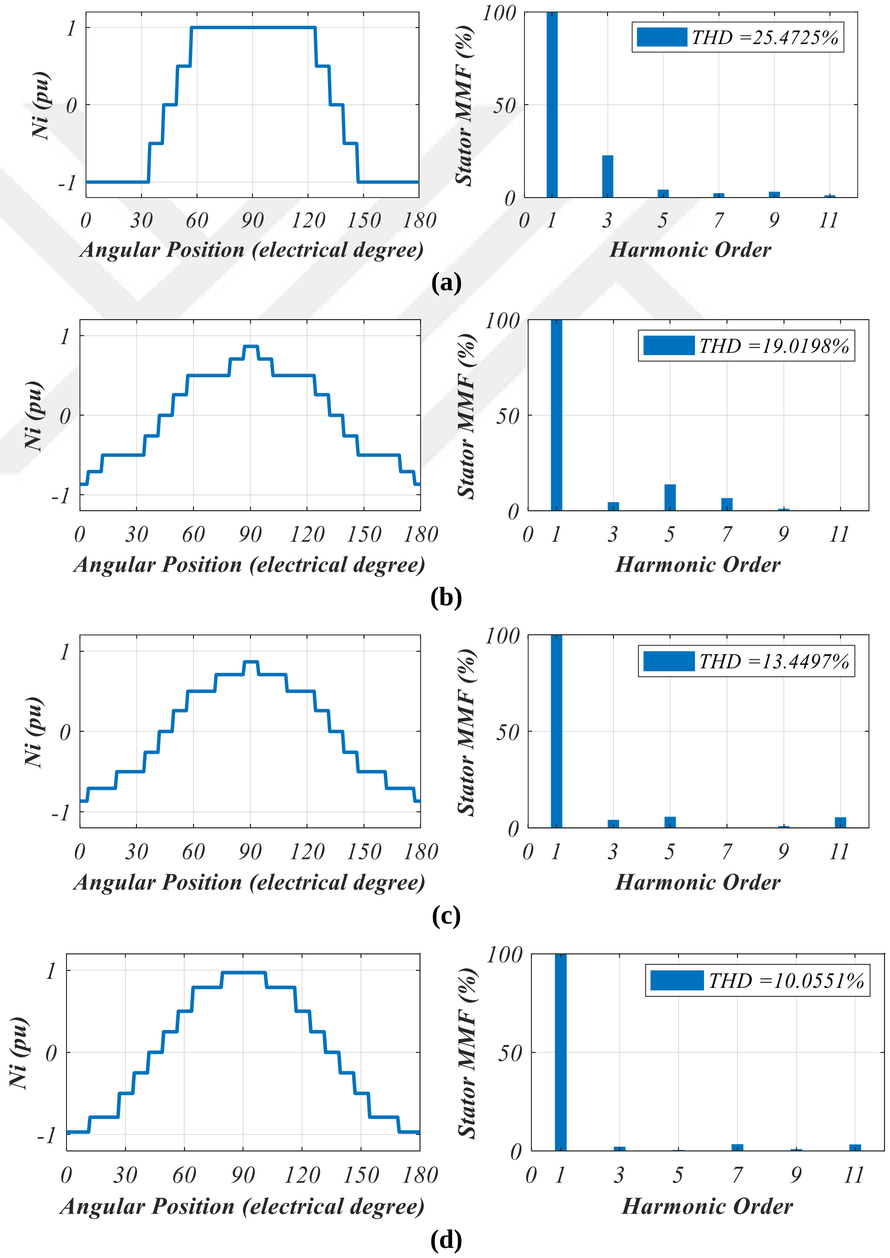

(a)

(b)

(c)

(d)

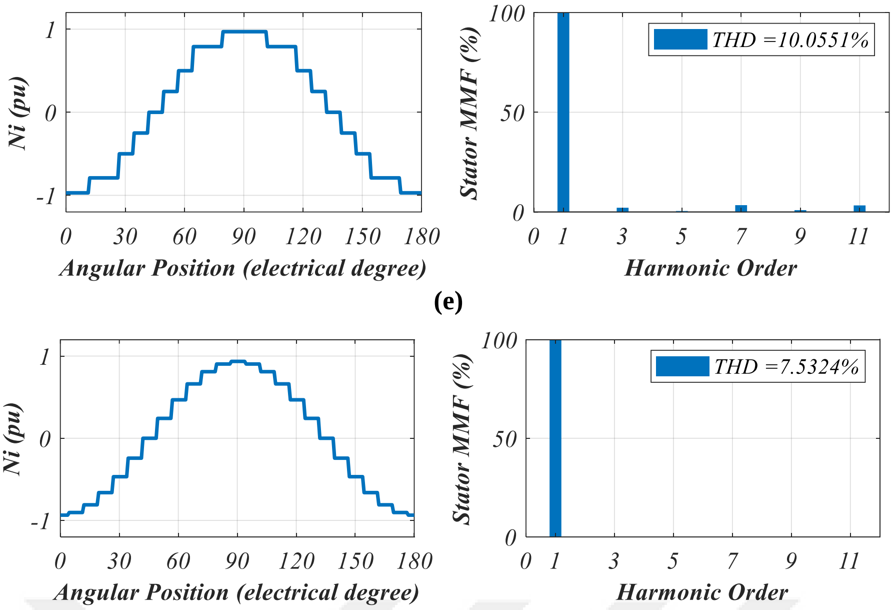

(e)

(f)

Figure 5.20 MMF distributions and the FFT of the (a) single-layer, (b) double-layer version 1, (c) version 2, (d) version 3, (e) version 4, and (f) triple-layer winding configurations

5.7.5 Design Optimization

In this section, a series of MODE optimization studies are presented. First, the general structure of the MODE algorithm is explained. Then, a series of winding optimization studies are carried out while using the proposed MODE that determines each coil group’s number of turns ratio to the total number of turns per phase with the objectives of minimizing the THD of the winding MMF and a score that indicates the total end winding length, EWS. At the end of this process, six Pareto front sets are obtained. Later a geometric optimization is performed using three results from each Pareto frontier set which are having the minimum THD, minimum EWS at a maximum of 20 % THD, and a point in between these two. The reason for selecting these results is to distinguish the effects of the MMF harmonics and the end winding length on the performance of the machine. While employing the maximum efficiency and minimum motor mass as the objectives, rotor geometry optimization is performed under specified conditions and Pareto optimal designs are determined and compared in terms of efficiency, mass, and torque ripple.

5.7.5.1 Winding Optimization

A 2-pole structure of LS-SynRM is required to be able to operate at 3000 rpm with a 50 Hz frequency and direct line voltage. However, a single-layer winding configuration increases both the length of the end winding and the THD, especially in a 2-pole motor structure. In this paper, various multiple-level winding configurations are analyzed and compared to reduce the THD and decrease the total winding length. Here, a single-layer, four different double-layers, and a triple-layer winding configuration are investigated. An optimization problem is created to determine the number of turns for each coil in a phase using MODE.

Optimization parameters are chosen to have individual weights of less than one, but sum up to the one in total for each coil in order to make the number of turns proportional to the total number of turns explained in the geometric optimization.

The optimization has two objectives which are THD and EWS, the calculations of these values are formulated in (5.12) and (5.13) [108].

$$THD = \frac{\sqrt{\left({F_{st}}^{5}\right)^2 + \left({F_{st}}^{7}\right)^2 + \left({F_{st}}^{11}\right)^2 + \left({F_{st}}^{13}\right)^2 + \cdots}}{{F_{st}}^{1}} = \frac{\sqrt{(\sum_{m=1}^{6}).({F_{st}}^{6m\pm1})^2}}{{F_{st}}^{1}} \tag{5.12}$$

$$EWS = \sum_{n} \frac{l_{arc,n}}{l_{WP}} k_n \tag{5.13}$$

Here, $l_{arc,n}$ is the arc length of the n^{th} coil group, l_{WP} is the perimeter of the circle that passes through the mid-points of the stator slots, and k_n is the proportional coefficient of the n^{th} coil group as shown in Figure 5.21.

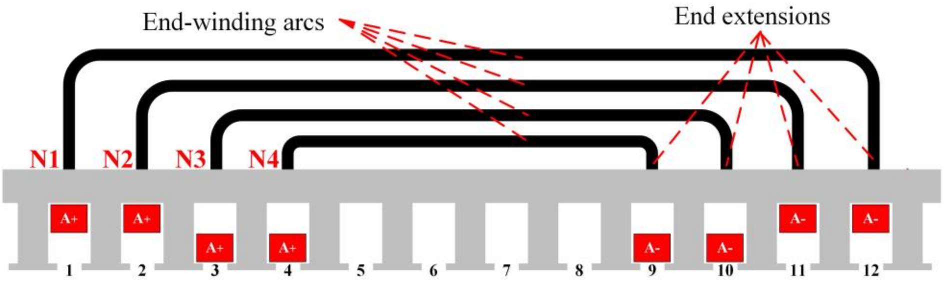

Figure 5.21 End winding illustration of a double layer winding configuration

5.7.5.2 Rotor Design Optimization

Although conducting a winding optimization based on analytical calculation gives some intuition about the outcomes, a geometric optimization based on FEA analysis is also required for acquiring more accurate results. Since conducting a geometric optimization takes quite computational work, three variations are selected for each winding configuration which represents minimum THD, minimum EWS, and a middle point between these two objectives. In order to perform a geometric optimization, an FEA model is developed in ANSYS Maxwell 2D. For the initial model, many geometric definitions decrease the efficiency of the optimization. To increase the optimization efficiency, the number of geometric design parameters is reduced to seven parameters which are highly effective on the output parameters. Visual representations of these parameters are shown in Figure 5.1 and related explanations are given in Section 5.1.5 Table 5.1. The rotor optimization process is repeated for each of the six different winding configurations using the same objectives and constraints which are given in detail in Section 5.1 above.

5.7.6 Analysis Results

In this study, six different winding configurations are tested for their harmonic distribution and end winding length. Since both of these parameters are quite effective on motor performance, a distribution is found considering these parameters using a MODE algorithm. The results of winding optimization with different winding configurations are presented in Figure 5.22.

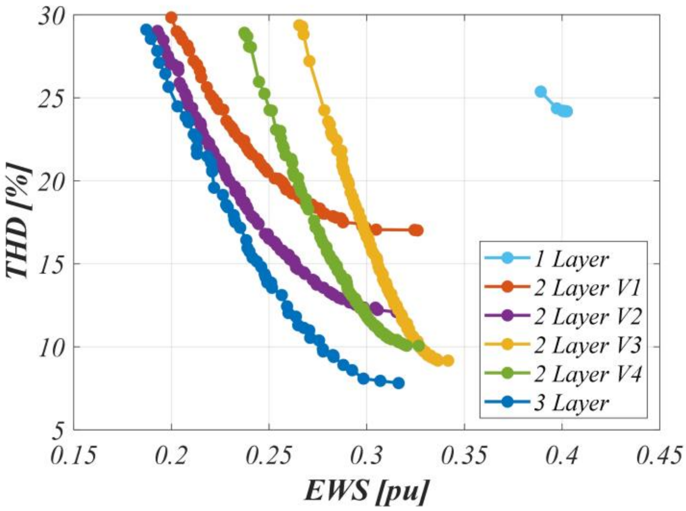

Figure 5.22 THD and EWS result in different winding configurations

The results indicate that there is a trade-off between THD and EWS. However, motor geometry is also an important determinant factor in machine performance. Therefore, three results from each winding configuration are selected where the THD is minimum, EWS is minimum at 20 % THD limit, and a mid-point between these points in terms of geometric optimization. The reason for these selections is to distinguish the effects of the harmonic reduction and end winding length reduction on the machine efficiency, mass, and torque ripple.

The geometric optimization results of the single-layer, double-layer versions 1, 2, 3, and 4, and triple-layer winding configurations are presented in Figure 5.23a, Figure 5.23b, Figure 5.23c, Figure 5.23d, Figure 5.23e, and Figure 5.23f, respectively.

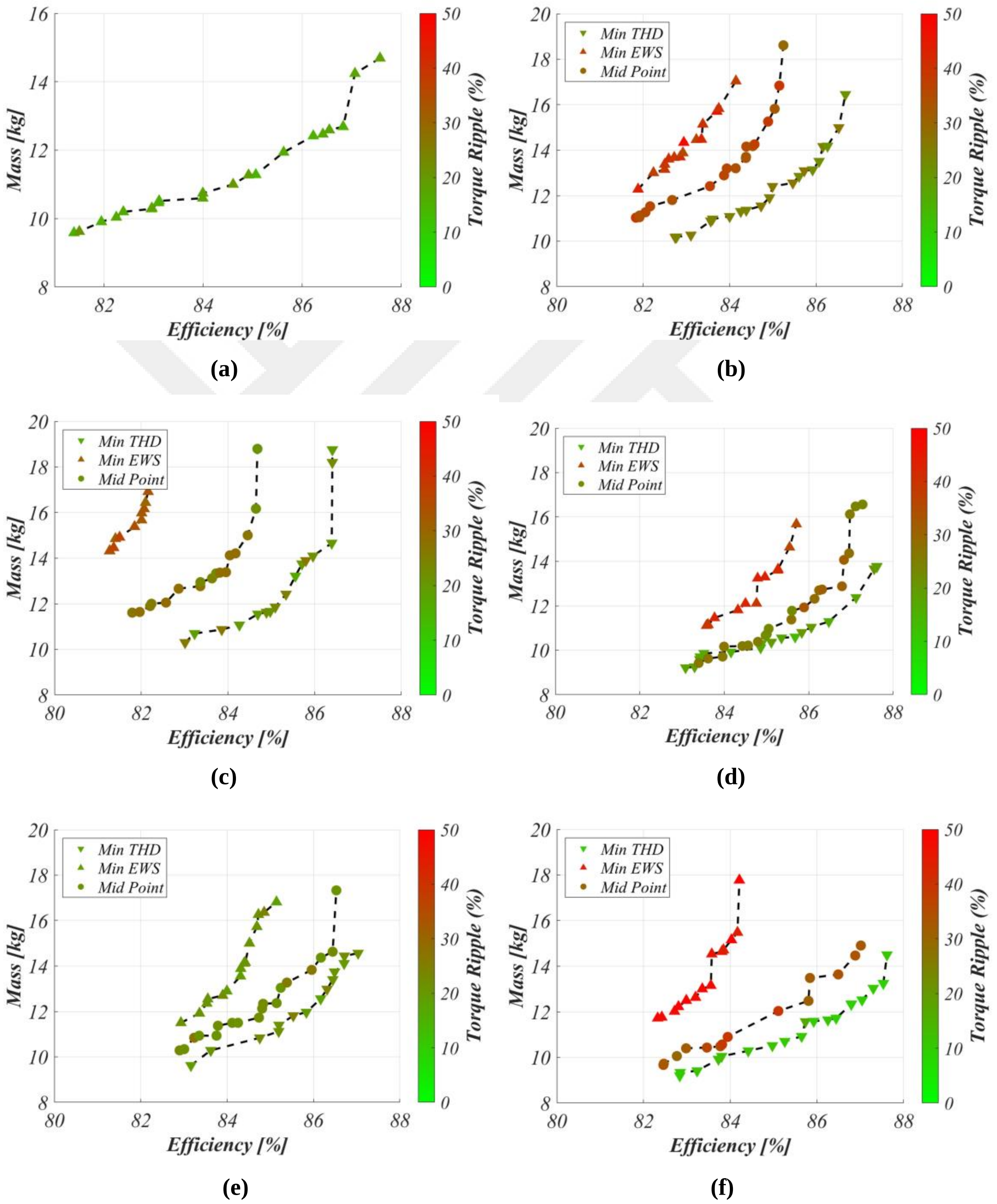

(a) (b)

(c) (d)

(e) (f)

Figure 5.23 Optimization results of the (a) single-layer, double-layer (b) version 1, (c) version 2, (d) version 3, (e) version 4 and (f) triple-layer windings

When the results of these different winding configurations are compared, it can be seen that the double-layer version 3 and triple-layer configurations have better results than the single-layer base configuration for the whole distribution. Fig. 5.24 demonstrates that some winding configurations can provide up to 2-points efficiency improvement. Also, a significant decrease in the torque ripple is observed, which is around 2-points for the double-layer version 3 and 7-points for the triple-layer configurations. This outcome is also effective in the noise and vibration performance of the machine which leads to improved reliability and life cycle of the machine. The results show that minimizing THD yields higher efficiency, lower torque ripple, and lower motor mass. On the other hand, reducing the end winding length provides copper loss reduction up to a point where the THD levels exceed a certain level which results in a decrease in torque production. From the results shown in Figure 5.23, it can be concluded that winding configurations that favor for minimization of THD yield better results in comparison with the configurations that minimize EWS.

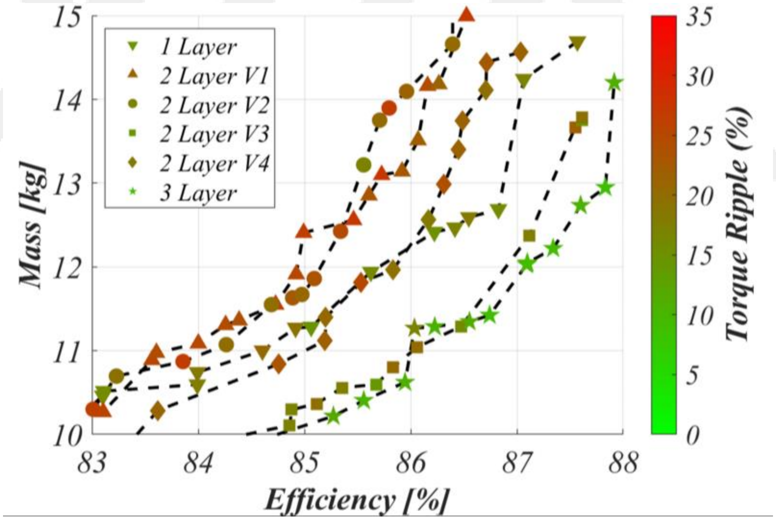

Figure 5.24 Comparison of Pareto front solutions of the considered winding configurations

This finding is parallel with the expectations since SynRM is highly affected by the magnetic field distribution. Minimum THD configurations for every winding scheme are given in Figure 5.24 as they have higher quality Pareto frontiers than others. When the results of the different winding configurations are compared, it is observed that the triple-layer and the 3rd version of the double-layer configurations have higher quality results than the other configurations for the whole distribution.

5.7.7 Pareto Front Quality Method

After obtaining the Pareto frontier solutions for all the winding structures are considered, a quality assessment method is used to quantify the quality of the Pareto front results. Since the optimization objective can be summarized as maximizing the efficiency while minimizing the mass and the torque ripple, assessment scores are proposed as follows:

$$S_1 = \frac{1}{n}\sum_{k=1}^{n}\left(\frac{Efficiency_k}{Mass_k}\right) \tag{5.14}$$

$$S_2 = \frac{1}{n}\sum_{k=1}^{n}\left(\frac{1}{\Delta T_k}\right) \tag{5.15}$$

The primary score, S_1, is the average value of the efficiency over the mass of a specific winding configuration Pareto frontier solutions while the secondary score, S_2, is the average value of the inverse of the torque ripple, ΔT^{-1}, where k is the number of the candidate designs in the specific winding configuration Pareto frontier solution set. Due to the way that these assessment scores are defined, a higher score means a better winding configuration. The reason the scores are named as primary and secondary is to highlight the importance of the score, the efficiency over the mass ratio is more important than the inverse of the torque ripple for the specific application. In order to distinguish the variation of the scores over the considered winding configurations and compare them easily, the calculated scores are normalized and plotted as shown in Figure 5.25.

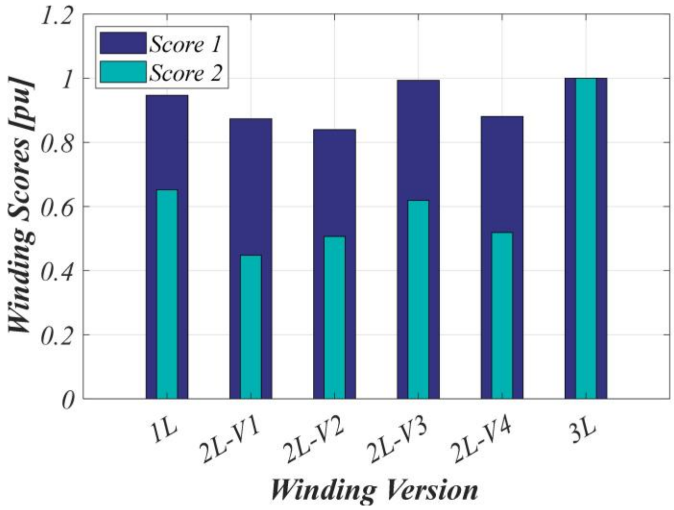

Figure 5.25 Score-based quality comparison of the considered winding configurations' Pareto fronts

In terms of the primary score, the triple-layer winding performed the best followed by the double-layer V3 and single-layer winding configurations. Similarly, the best-performed configuration is the triple-layer configuration in terms of the secondary score which is followed by the single-layer and double-layer V3 ones. At this point, prioritizing the scores helps one to assess the goodness of the various winding configurations. Hence, the triple-layer winding configuration performs the best among others and the double-layer V3 configuration comes next. Although the secondary score of the single-layer winding yields a higher score, the primary score of the double-layer V3 winding is better than the single-layer one. This result can also be reached by observing the Pareto frontier solutions sets given in Figure 5.23, the best-performed configuration is placed close to the right bottom corner. The Pareto front solutions of the other configurations move to the upper left corner as the performance is degraded. However, it is hard to distinguish the quality of the multiple Pareto front solutions when they get close to each other. Thanks to the score-based comparison, a clear assessment can be made.

5.7.8 Conclusions

In this part of the research, a 2-pole LS-SynRM with several multilayer (ML) winding configurations that have an uneven number of turns on each coil group on various performance parameters is provided. Single-layer, four different versions of double-layer, and triple-layer winding structures are considered for a 24-slot stator. The analysis is performed in two stages. First, a winding optimization that determines each coil group’s number of turns ratio to the total number of turns per phase with respect to the objectives of minimizing the winding MMF THD and a score that indicates the total end winding length, EWS. This process is done with the MODE algorithm for all the winding configurations. Later a geometric optimization is performed using three of the winding optimization results which are having the minimum THD, minimum end winding score at a maximum of 20 % THD, and a point in between these two from each winding configuration. The reason for selecting these three results is to distinguish the effects of the MMF harmonics and the end winding length on the performance of the machine. The second optimization is performed for the determined conditions and Pareto optimal designs are determined and compared in terms of efficiency, mass, and torque ripple. A score-based Pareto front quality assessment method is proposed to quantify and select the best winding configuration. Based on the results, it is concluded that:

- Among all the winding structures, the triple-layer winding structure yielded the highest quality results.
- Considering the manufacturing complexity and cost, the double-layer, version 3 winding configuration that has a similar score to triple-layer winding came forward as a better alternative.
- Better MMF distribution leads to higher torque production, smaller machine size, and lower torque ripple.
- Score-based comparison made it easy to distinguish the quality of the Pareto front solution sets.
- Compared with the single-layer configuration, up to 2 points of efficiency improvement and a significant torque ripple reduction are achieved.

5.8 Designs with Double Layer and Comparison

The 2-pole, 4 kW, LS-SynRM analyses are performed according to the previously obtained results and the results are updated accordingly. The results are given as a comparison in this part of the thesis study. Starting from the 4-flux barrier design analysis with single and the previously selected double layer stator winding are provided in Figure 26. The optimization process including parameters, objectives, and constraints is the same as in Section 5.1. Here, the aim is analysis the single-layer and double-layer designs including damping effects while the D_{OS} is 8 mm.

According to the analysis results, the performance of the designs with 7, 8, and 9 flux barriers came very similar and efficiency slightly increased at the 9 flux barrier design while others are cannot handle the constraints properly. However, the thickness of the barrier and the carrier did not seem reasonable at 9 FB it was very thin. Hence, the 7 flux barrier design both with a single layer and double layer structures is determined as the best optimum candidate design compared to the others. Further analyses are carried out to for determining the best candidate for LS-SynRM for manufacturing.

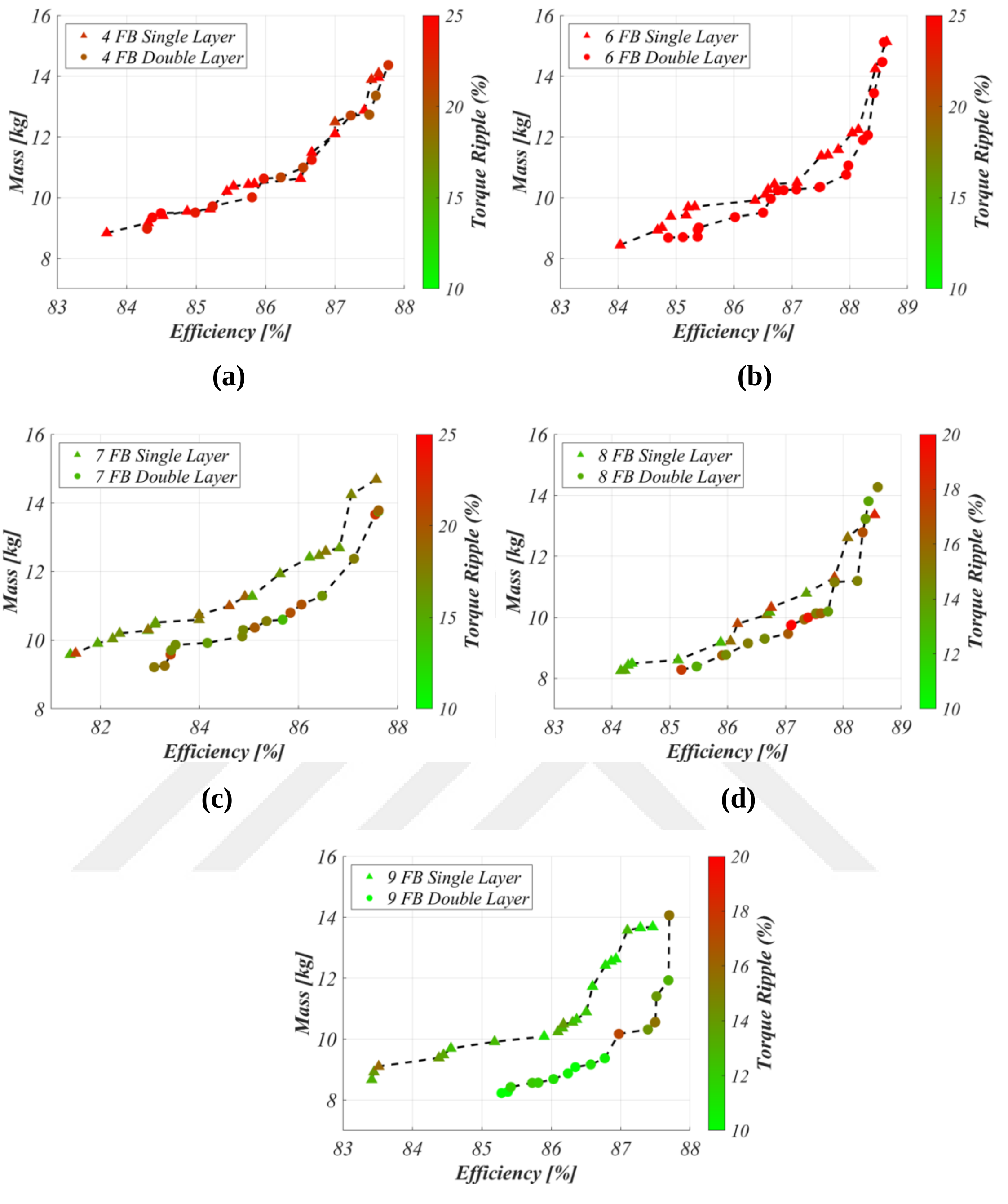

(a) (b)

(c) (d)

(e)

Figure 5.26 Analysis results with single layer and selected double layer winding structures for (a) 4, (b) 6, (c) 7, (d) 8, (e) 9 flux barrier design

5.9 Synchronization Capability and Performance Analysis of the Selected Candidates

In this section, the best designs from the Pareto Frontier are collected and the synchronization performance of each design is tested and the results are provided in

Figure 5.27 and Figure 5.28 with single-layer winding and double-layer winding structures, respectively.

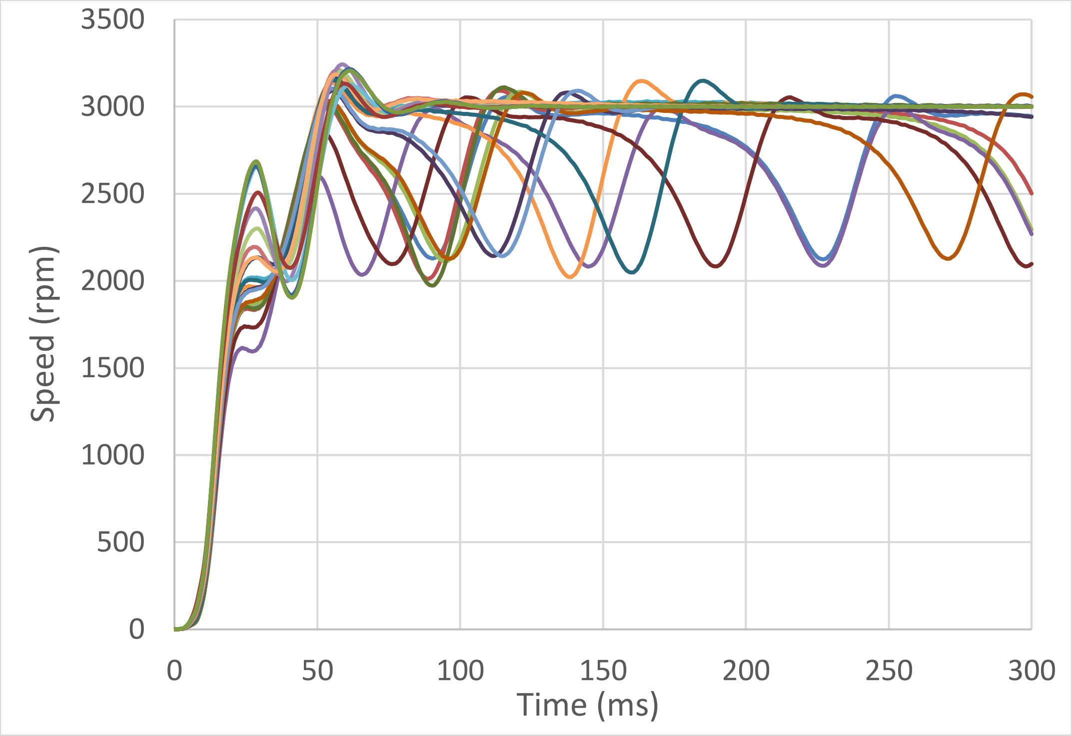

Figure 5.27 Single layer candidate designs synchronization performances

21 candidates could handle the constraints while providing the objectives requirements for 7 flux barrier, single layer winding LS-SynRM. 15 of them can be synchronized while 6 of them failed.

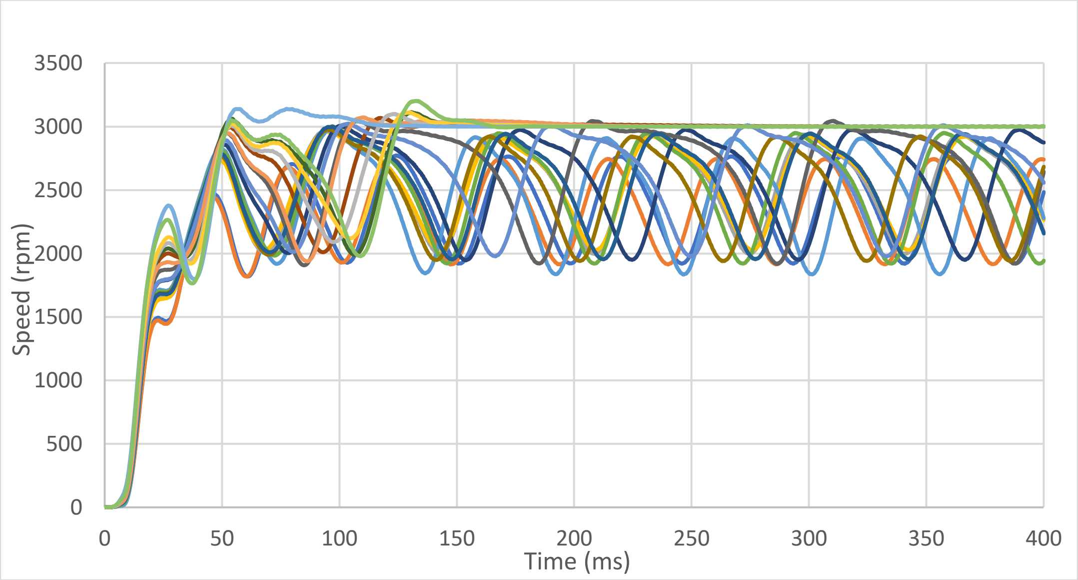

Figure 5.28 Double layer candidate designs synchronization performances

Here, 18 candidates could handle the constraints while providing the objectives requirements for 7 flux barrier, double layer winding LS-SynRM. 7 of them can be synchronized while 11 of them failed.

The best two designs are selected from the synchronized candidates' designs one with single-layer and another with double-layer winding structures. All the parameters belonging to these designs are listed below to be used for performance analysis.

Table 5.14 Performance analysis results of the highest efficiency designs with single and double-layer structures

Layer Type	**Eff. (%)**	**Mass (kg)**	**Torque Ripple (%)**	**Stack Length (mm)**	**L_d/L_q**	**R_{ph} (ohm)**	**L_{leak} (mH)**	**CD (A/mm^2)**	**I_{peak} (A)**	**PF**
SL	87.06	14.24	17.22	149.41	6.15	1.47	5.8	6.095	13.10	0.72
DL	87.54	13.67	22.00	148.21	7.13	1.37	6.5	6.070	12.33	0.75

Considering the very similar performance results of these two designs and manufacturing complexity and the design with the single layer is selected for manufacturing.

5.10 Thermal Analysis

Submersible water pumps run inside the water and the stator is filled with fluid to avoid water intake and fluctuation inside the machine. The fluid inside usually is chosen as a mixture of water and polypropylene glycol due to its anti-freeze structure Therefore, since both the stator and the rotor are flooded at this type of motor the thermal analysis should be done accordingly.

LS-SynRM has an advantage over the wound rotor IM since they do not have any winding on the rotor in terms of thermal conditions. The submersible version of the IM usually consists squirrel cage rotor. The cage inserted into the rotor helps the machine to run into synchronization in the prototyped LS-SynRM. After the synchronism, there exists no induced voltage in the cage, therefore, the losses will be reduced. In other words, no current will be induced through the bars after the synchronism, and this will turn back as an advantage to lower the copper loss and the temperature accordingly. Therefore LS-SynRM provides better thermal performance compared to both cases; wound rotor IM and squirrel cage IM.

Here, the general operating conditions of the pump system are considered, and the fluid is introduced both inside (domain) and outside the pump motor using the ANSYS program (Figure 5.29). Then, an outer surface with a constant temperature of 20°Celsius is assigned. The fluid inside the motor is assumed as stable since it is almost completely filled with a mixture of liquid. Here, since the copper losses of the stator winding are determined previously, these losses are assigned to the winding and then the volume of 12 coils in the stator is calculated and integrated into the ANSYS/ CFD program as W/m^3.

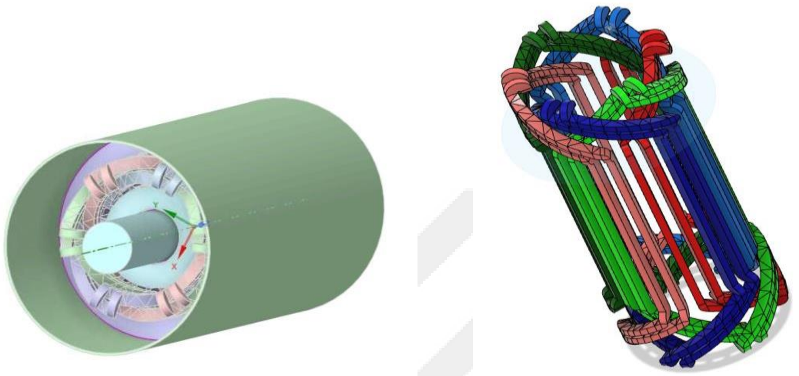

(a) **(b)**

Figure 5.29 (a) LS-SynRM with liquid filled domain (b) LS-SynRM stator windings introduction for ANSYS thermal analyze

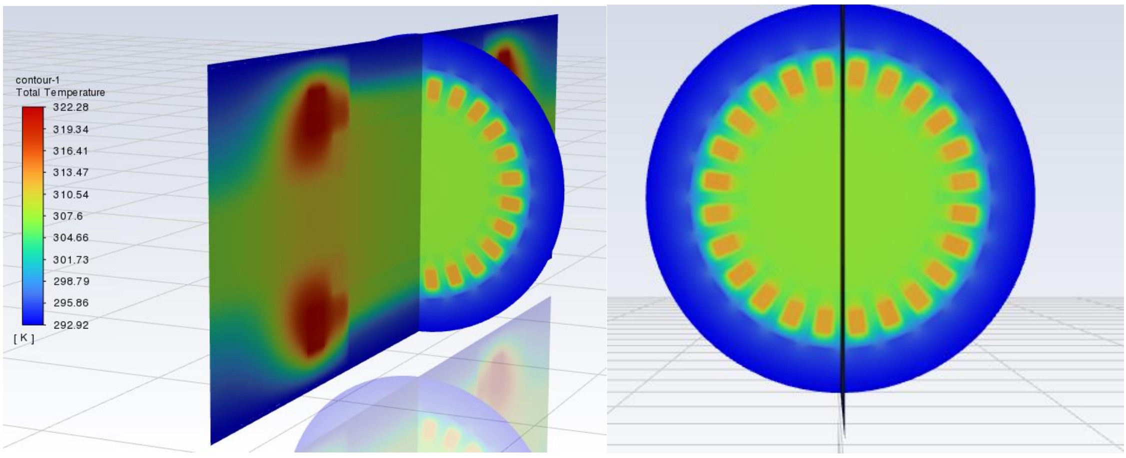

(a) **(b)**

Figure 5.30 Thermal analysis (a) side view, (b) front view of the LS-SynRM

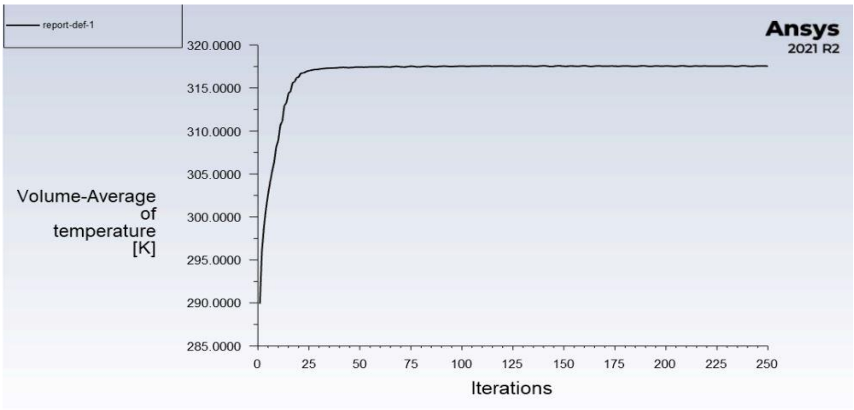

Figure 5.31 Temperature rise of the LS-SynRM with respect to iterations (time)

According to the thermal analysis results of the proposed submersible water pump motor (LS-SynRM) the average temperature of the motor is determined as 317°Kelvin which corresponds to 44°C. Results obtained from the ANSYS thermal analysis are given in Figure 5.30 and Figure 5.31 shows the temperature rise of the proposed motor with time. The maximum temperature rise is determined as 49°C which is obtained from the end windings as expected. The magnet wire insulation starts to degrade and melt at around 180°C. Therefore, it can be concluded that the thermal analysis results came within acceptable boundaries.

5.11 Conclusions

In Chapter 5, the whole design and optimization steps and their simulation results are presented as illustrated in Figure 5.32.

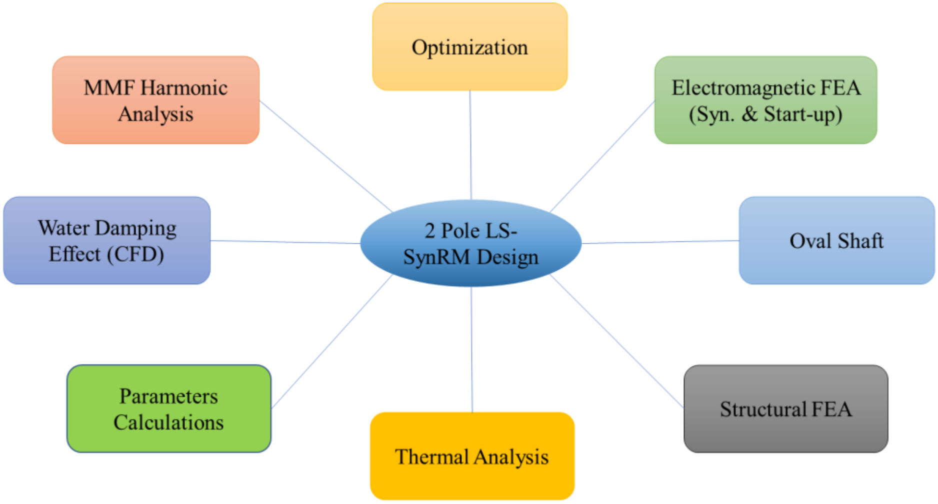

Figure 5.32 A summary of the works has been done throughout the thesis study

In this thesis study, a 2 pole, 4 kW, 6 inches diameter LS-SynRM as a submersible water pump motor is designed and optimized with a new oval shaft structure. Here, it is aimed to improve the machine performance by widening the flux path on the rotor by narrowing down the shaft on the q-axis. Initially, necessary motor design parameters such as the number of flux barriers, stator winding current density, number of turns, and geometric optimization of the rotor are investigated using MODE and maximum shaft reduction is taken as 5 mm. The objectives of the optimizations are to increase efficiency while minimizing the motor mass. Line voltage, torque ripple, and motor mass are selected as constraints and certain boundaries are assigned. According to the results obtained from the analysis given in this section, the rest of the study is performed using the design with 7 flux barriers. Here, the efficiency is recorded as 89.240 %, and the motor mass is obtained as 13.35 kg while the shaft size reduction is kept coming as 5 mm and damping loss is assumed as 100 W.

Since the submersible pump motors run inside a fluid-filled environment, the damping effect of the fluid has to be taken into account during the design process. In the literature, damping loss is assumed as windage loss in most of the studies related to the water pump system’s motor design. Here, the damping loss is investigated using computational fluid dynamics FEA since the water is denser than the air and it causes more loss compared to the windage loss. Analyzes are done for three different stator slot opening structures. Damping loss came up around 362 W with the standard wedge while the loss belongs to the design with custom wedge structure obtained as 139.9 W where the windage loss under the same condition is 0.33 W. Therefore, fluid damping effect cannot be assumed as windage loss like in the air-cooled motors in flooded motor structures and cannot be ignored for estimating the machine performance accurately and making the stator inner surface as smooth as possible and eliminating the indents reduces the damping loss of the fluid-filled motors significantly.

Previous analysis showed that the shaft size reduction gave positive results in terms of motor performance improvement and the reduction size was assigned up to 5 mm. However, at this point, it is important to consider the effects of the new shaft design on structural integrity, vibrations, and deformation of the rotor. In order to determine the safe maximum shaft dimension limits, a series of structural analyses are performed using FEA. After performing the stress, deformation, and vibration analysis it is observed that narrowing down the shaft on the q-axis up to 8 mm is acceptable and safe.

After including the damping loss and taking the shaft size 8 mm smaller than the original circular shaft, the motor optimization was reperformed using MODE. The maximum efficiency for the 8 mm narrowed oval shaft design is recorded as 87.06 % with a motor mass of 14.24 kg, and torque ripples between 15.0% and 24.3% whereas the maximum efficiency for the 5 mm narrowed oval shaft design is recorded as 86.95 % with a motor mass of 14.9 kg and torque ripples between 15.1%, and 32.0% and the maximum efficiency for the circular shaft design is recorded as 85.81 % with a motor mass of 14.68 kg and torque ripples between 21.7%, and 40.4%. When the proposed LS-SynRM is compared to the same size commercial IM for the same submersible pump motor applications, it not only makes a difference of more than 15 points betterment in efficiency but also challenges the position of IM that holds in the market. The machine efficiency class is improved from standard efficiency IE1 to premium efficiency IE2 compared with the conventional IMs at the same power level. On the other hand, PMSMs are almost 3 times more costly than the LS-SynRM with a questionable couple of points of improvements in efficiency while requiring dependency on permanent magnets and a motor driver which comes at an additional cost and complexity.

Therefore, this study proves that the proposed LS-SynRM is a new rival for all types of motors in the submersible pump market because of its high efficiency, lightweight, simplicity, ruggedness, driverless/line start property, no permanent magnet requiring structure, and low investment and running costs.

Furthermore, since air-gap flux with space harmonics induces excessive copper and core losses in addition to vibration and acoustic noise, a proper configuration of stator windings with reduced winding MMF space harmonic content which leads to improved machine performance is investigated. Single-layer, several versions of double-layer, and triple-layer winding structures with an uneven number of turns on each coil are applied to a 24-slot stator. Among all the winding structures, the triple-layer winding structure yielded the highest quality results. Considering the manufacturing complexity and cost, the double-layer, version 3 winding configuration that has a similar score to triple-layer winding came forward as a better alternative. Best designs from the Pareto Frontier are collected and the synchronization performance of each design is tested. The best two designs are selected from the synchronized candidates' designs one with single layer and another with double layer winding structures. The design with single layer has 87.06 %

efficiency with 14.24 kg while the one with double layer has 87.54 % and 13.64 kg which is slightly better.

Considering very similar performance results of these two designs and manufacturing complexity and the design with the single layer is selected for manufacturing. The manufacturing process and the parameters of the built machine are presented in Chapter 6.

Chapter 6

Prototyping and Test Results

6.1 Introduction

The 2 pole, 4 kW, 6 inches diameter LS-SynRM for downhole submersible water pump applications presented in this dissertation has been prototyped for proof of concept. This chapter presents the process for building the prototype machine and testing it.

6.2 Manufacturing

The manufacturing of the machine is tedious work as it includes multiple stages being completed in different workstations and even different places. The stator of the machine and final assembly of the machine is completed in Mutlusu Pumps and Motors factory while the rotor parts are manufactured in different facilities. The manufacturing process is detailed below.

The stator stack is built with the punched laminations used in the commercial 6-inch IM stator laminations. The laminations are welded and inserted into the stainless-steel motor housing before winding as shown in Fig. 6.1.

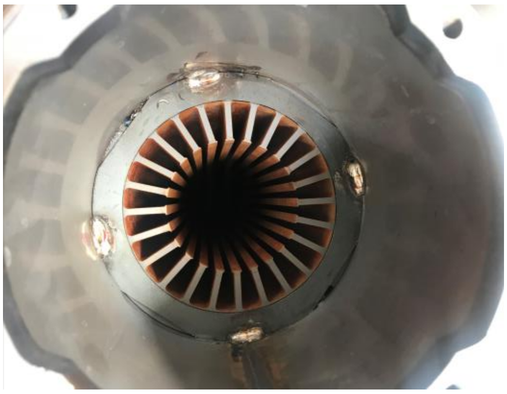

Figure 6.1 Stacked stator laminations inserted into a stainless-steel housing

After preparing the stator body, the windings are placed into the stator slots as presented in Fig 6.2.a. It should be noted that the submersible motor stator stacks are placed into the motor housing before windings are placed. Therefore, the winding procedure becomes a challenging task as the winding area is limited. Moreover, the windings should be carefully placed without damaging the isolation as the motor is filled with water in regular operation. Also, the submersible pump motor cables are double isolated with enamel coating and PVC (Polyvinyl chloride) that are harder to handle.

(a) **(b)**

Figure 6.2 (a) Winding insertion into the stator slots and (b) inside the stator

The stator windings are stabilized with wedges that are specially designed to generate a smooth airgap surface for reducing the water damping loss. The wedges are 3D printed with ABS (acrylonitrile butadiene styrene) filament as ABS can preserve its shape at the temperatures that the prototype machine works. The smooth stator surface can be seen in Fig. 6.2.b and the 3D printed wedge is shown in Fig 6.3.

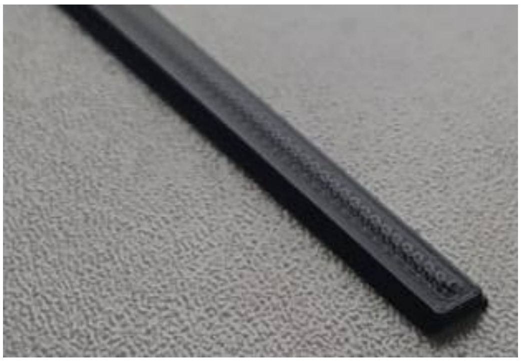

Figure 6.3 Specially designed, 3D printed wedge for smooth airgap surface

After the winding, the stator is made ready by connecting the stator coils and making the connections waterproof.

The rotor manufacturing process includes:

- Rotor lamination cutting,
- Oval shaft machining,
- Rotor bars and end rings manufacturing,
- Rotor stacking,
- Insertion of the rotor bars,
- Soldering the end rings,
- Machining and longitudinal turning,
- Bearing insertion.

The rotor laminations are prepared for the laser cut process by extending their outer diameter to provide extra room for the final surface smoothing process.

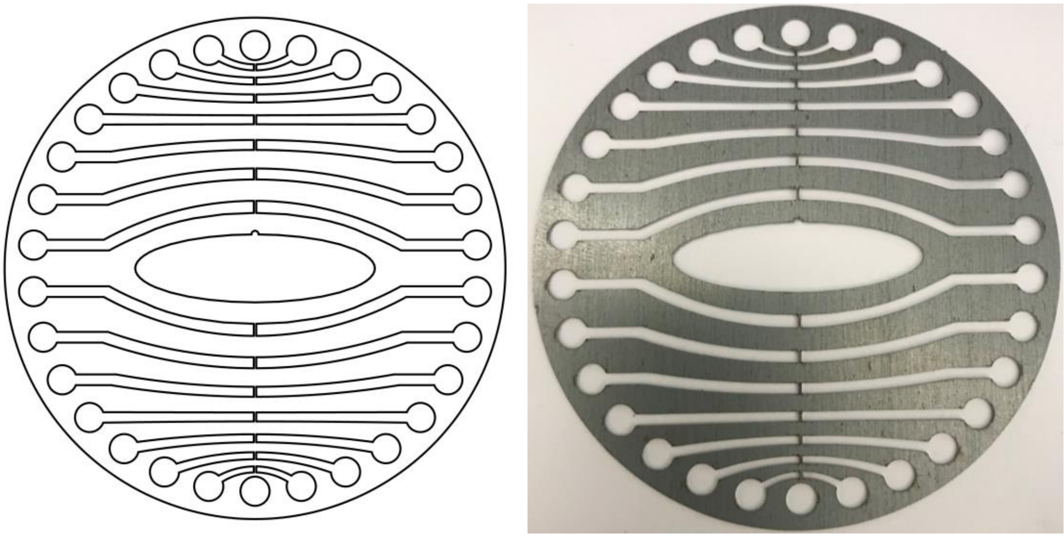

(a) (b)

Figure 6.4 (a) Rotor lamination CAD drawing and (b) laser cut lamination

The shaft of the motor has a unique cross sectional shape that needs to be carefully manufactured using automated machining tools. As the rest of the shaft is circular, the rotor laminations cannot be inserted due to their cross section being oval. Therefore, the shaft is manufactured as two pieces and connected together after laminations are stacked onto it as shown in Fig. 6.5.

Figure 6.5 Manufactured shaft pieces

The rotor bars and end rings are made out of copper and manufactured as shown in Fig. 6.6.

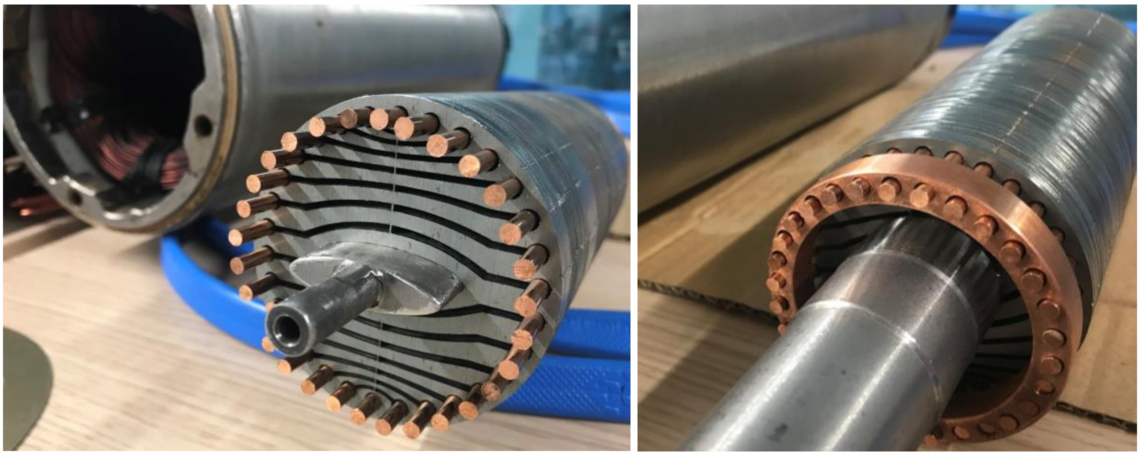

(a) (b)

Figure 6.6 (a) Copper rotor bars and (b) end rings

After all the parts are separately manufactured, the rotor stack is ready to be assembled. The laminations are inserted onto the oval part of the shaft as presented in Fig.

6.7. The designed rotor stack is placed next to the commercial IM rotor stack for comparison.

Figure 6.7 Stacked rotor laminations onto the oval shaft

The laminations needed to be pressed and welded to the shaft for tight assembly. The pressing process and welded laminations are shown in Fig. 6.8.

(a) (b)

Figure 6.8 (a) Rotor stack pressed together and (b) welded to the shaft

The end rings and the rotor bars are soldered together, then, the second piece of the shaft is connected to the main piece and welded together as shown in Fig. 6.9. Here, since the rotor bars' thickness is lower than IM's bar, extensions of the rotor bars are left as shown in Fig. 6.9. It should be noted that since the pump system is running inside the water, the extensions of the bars will have effect as in fans, and it will result in slightly reduced efficiency.

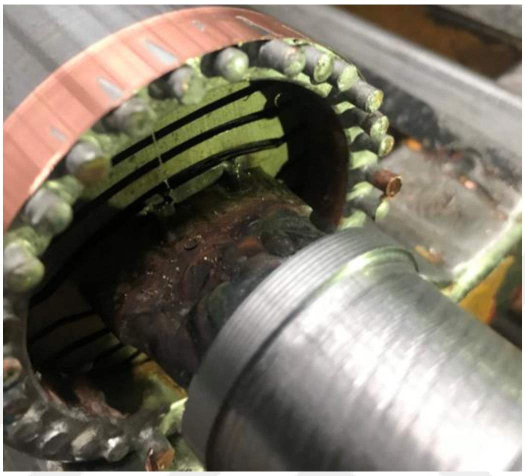

Figure 6.9 End rings are soldered to the rotor bars and shaft pieces are welded

Hence, the rotor has become a single piece of equipment after this step. However, it is still in its coarse form. Its outer diameter should be adjusted with longitudinal turning and balanced. So, the next step is the turning station for all these adjustments as shown in Fig. 6.10.

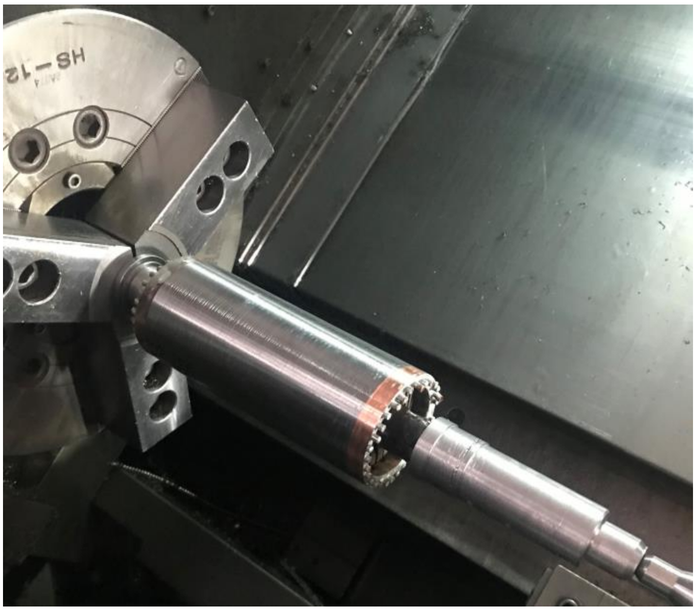

Figure 6.10 Rotor being ground and balanced in longitudinal turning station

After the final machining, the rotor surface is smooth, its diameter is adjusted to 67.3 mm, and balanced as shown in Fig. 6.11.

Figure 6.11 Finished rotor

As a last step, the rotor bearings are inserted into the shaft by benefiting the heating expansion with induction heating as shown in Fig. 6.12.

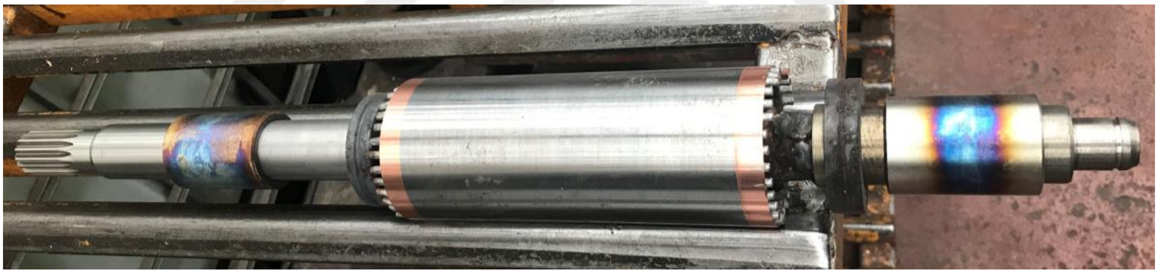

Figure 6.12 Finished rotor after bearings are inserted

The final assembly of the machine is done by adding the peripheral equipment such as the thrust bearings, cable connections, flange, etc., and inserting the rotor into the stator as shown in Fig. 6.13.

Figure 6.13. Assembled motor

6.3 Test Setup

The motor performance tests are made at Mutlusu Motor and Pump Test Center which is accredited by TÜRKAK (Turkish Accreditation Agency). The test setup and testing procedure are explained below.

The test system is built for motor, pump, and complete system testing. Hence, the motor testing is not done with a dynamometer but with a water pump inside a water tank. In other words, the motor is not loaded with another motor, it is coupled with a water pump through a torque sensor.

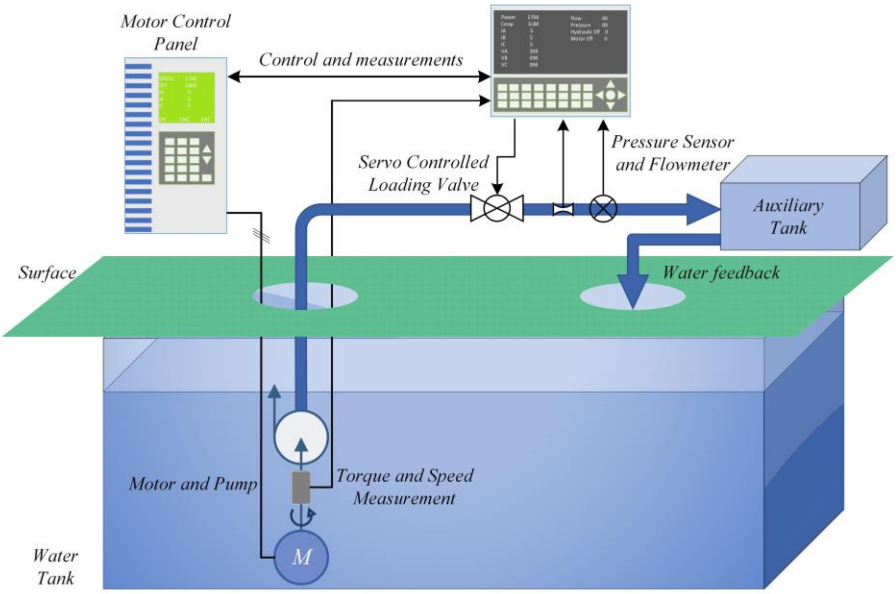

Figure 6.14 Motor and pump test system

An illustration explaining the motor test system is provided in Fig 6.14. Here, the motor is coupled with a torque sensor chamber which is pressurized with air to prevent water from leaking inside the chamber. The torque sensor can measure the shaft torque and the speed which are fed to the test control system to calculate the output power. Then the other side of the torque sensor chamber is coupled with the appropriate water pump and the pipes that carry the water out of the pump as shown in Fig 6.15. Water then passes through a servo-controlled valve. The use of this valve is to adjust the amount of water coming out of the pump. If the valve is fully closed, there is not any water flow through the pump; hence, the loading is adjusted to its minimum value. As the valve is opened there is water flowing through the pump. The required torque to operate the pump at a certain speed is higher when there is a water flow, i.e., the amount of water flowing through the pump increases the required torque and the pump motor loading is adjusted. Therefore, the loading is controlled by adjusting the valve.

Figure 6.15 Motor under test, torque sensor, and pump assembly

Figure 6.16 Servo-controlled valve, pressure sensor, flowmeter, and auxiliary tank arrangement

After the valve, a pressure sensor and a flowmeter are placed on the water pipe for calculating the hydraulic output power. After passing through the sensors, the water goes into the auxiliary tank that feeds the water back to the main tank. This way the water level in the main water tank is not disturbed during the test. The servo-controlled valve, pressure sensor, flowmeter, and auxiliary tank arrangement are shown in Fig. 6.16. All the measurement data is fed back to the computer for various calculations.

6.4 Experimental Study

After preparing the test arrangement, the motor is tested at various loading conditions. The synchronization is achieved when the machine started with the line voltage. Then, the servo-controlled valve is adjusted to control the water coming out of the water pipe, i.e., to control the motor loading. Depending on the water amount passing through the valve, shaft torque is varied, more water caused higher torque output. The test system is limited with the pump coupled to the motor and the servo-controlled valve system; hence, the loading cannot be started from zero torque conditions. Considering the machine coupled with a water pump never operates without loading, the test reflects the real working conditions.

6.4.1 Manufacturing Challenges

The SynRM performance is highly dependent of the final manufactured rotor geometry and magnetic properties of the electric steel as it does not contain permanent magnets. Although the machine is optimized for its best performance for the given objectives and constraints, the manufactured motor may behave differently than the original design. The major reasons for that are the manufacturing tolerances and magnetic material degradation due to the mechanical processes such as cutting, punching, pressing, welding, etc. However, the effects cannot be accurately estimated without a statistical analysis which can only be performed with mass produced batches of motors. Therefore, such an analysis cannot be performed on a prototype motor where there are only one or two samples manufactured. A reasonable approach would be measuring the B-H curve of the welded stator stack. Section 6.4.2 explores and explains the magnetic degradation of the electric steel stack after stacking and welding. Moreover, the quality of the material is another important issue to consider. Depending on the manufacturer, some of the imported materials do not have enough material quality which results in a low quality B-H curve.

Further uncertainties also exist in electric machine manufacturing such as winding problems as prototyped machines often hand wound where the quality may change from person to person. Even making the winding connections and taking the terminal cables outside the motor housing causes additional resistive effects. As a result, the winding impedances may vary and even impedance balance is lost in some cases. In such a scenario, the machine will not perform the way it is designed for.

In this study, above mentioned problems were also faced. The machine is wound with a reduced size magnet wire as the originally selected cable size did not fit into the slots, when attempted, winding isolation was damaged. Hence, the winding resistance is increased by about 25% which degraded the machine efficiency. In addition to this, the end winding length becomes slightly larger; hence, increasing the leakage inductance value.

In summary, prototype machine manufacturing is a big challenge as it involves many people who are experts in their regular work but when they are asked to build something new, they have to gain experience before they can build the prototype properly.

In this study, the prototype machine was built by sixteen different people in four different cities. One complete rotor and two stators are ruined before building the final prototype.

6.4.2 Magnetic Degradation of the Electric Steel

The magnetic degradation of electric steel is a known phenomenon and explored deeply in the literature [70,109]. Mechanical stresses caused by cutting, punching, stacking, welding, and even the press fitting processes degrade the magnetic properties of the magnetic materials [110]. In this study, the stator laminations are the commercial machine laminations used in the 6-inch motors which are made of 0.5 mm thickness M400 electrical steel. These laminations are punched, stacked, and welded together. All these processes caused the material to change its B-H curve slightly and increase its core losses. Unfortunately, there is not any known method to directly estimate the degradation but to test the material. The most famous method to measure the B-H curve is the four-wire method [70,109].

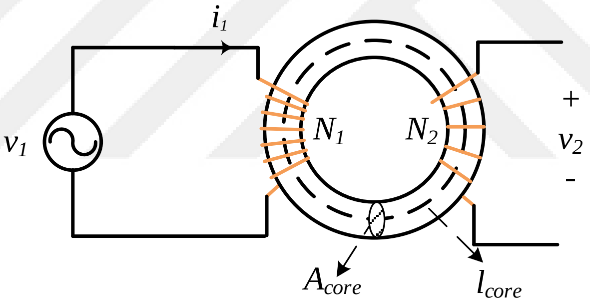

Figure 6.17 Four-wire B-H loop measurement test

Here, the primary winding is excited to generate flux through the magnetic core. The voltage of the secondary winding is then integrated for flux and flux density calculation. The magnetic field intensity is calculated as;

$$H(t)=\frac{N_1 i_1(t)}{l_{core}} \tag{6.1}$$

where, N_1 is the primary winding number of turns, i_1 is the primary winding current, and l_{core} is the active length of the core under test. The induced voltage is expressed with the following expression.

$$v_2(t)=N_2\frac{d\phi(t)}{dt}=N_2 A_{core}\frac{dB(t)}{dt} \tag{6.2}$$

where N_2 is the secondary winding number of turns, ϕ is the flux passing through the core, A_{core} is the cross-sectional area of the core, and B is the magnetic flux density.

Then, the flux density can be calculated as;

$$B(t)=\frac{1}{A_{core}N_2}\int v_2(t)dt=\frac{1}{A_{core}N_2}\lambda_2(t) \tag{6.3}$$

where λ_2 is the flux linkage of the secondary winding.

The welded stator laminations are wound with two windings as shown in Fig. 6.18 and 50 Hz excitation is used to excite the core through the primary windings. The primary winding current and secondary winding voltages are measured with the hall effect current probe and differential voltage probe. The B-H curve measurement setup is shown in Fig. 6.19. The measured data is then recorded and required calculations are carried out in MATLAB.

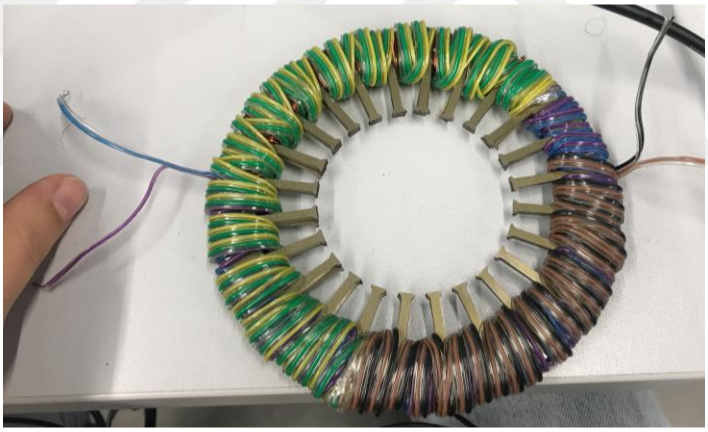

Figure 6.18 The toroid core under test

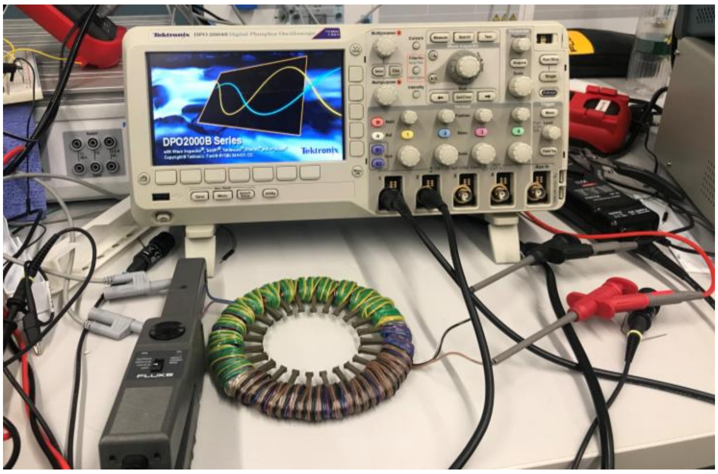

Figure 6.19 B-H loop measurement setup

The procedure is repeated for various voltage levels and B-H loops that are nested together are obtained. The corner points of these loops are then connected to obtain the static B-H curve of the material.

The measured and expected material B-H curves are shown in Fig. 6.20. It is observed that there is a slightly over 6% discrepancy between the expected and measured results.

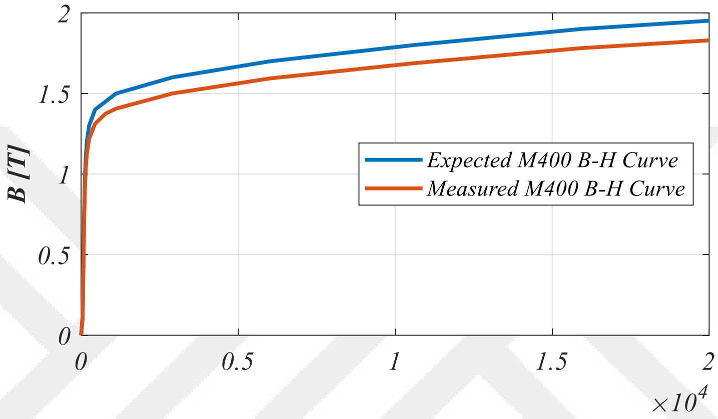

Figure 6.20 Measured and expected static B-H curves comparison

After obtaining the actual B-H curve, the FEA of the manufactured machine is performed again to distinguish the discrepancies between the designed and built machines. The comparison of the rated operating point results is provided in Table 6.1.

Table 6.1 Initial and Prototyped Machine FEA Results Comparison

Parameter	Designed Machine	Prototype Machine
P_{in} (W)	4598	4441
$P_{out, rated}$ (W)	4000	3740
I_{rms} (A)	9.26	9.33
Torque (Nm)	12.75	11.9
R_{ph} (ohm)	1.47	1.75
L_{leak} (mH)	5.8	7.1
L_d/L_q	6.15	5.45
Power Factor	0.72	0.69
Efficiency (%)	87.06	84.2

6.4.3 Test Results

The motor performance tests are performed with the 4-kW commercial IM and the prototyped machine. The performance test results are presented in Table 6.2 and Table 6.3 for IM and prototype machine, respectively. It should be noted that the efficiency comparison is made with respect to the output power as the IM’s speed varies with the loading while the LS-SynRM rotates at 3000 rpm. Consequently, for the same output power level IM’s speed and torque are different than the prototype machine’s speed and torque. Thus, different water pumps are used for IM and prototype machine while loading the machines. The pump coupled with IM can load the machine at 4 kW output power at 2820 rpm, while the other pump coupled with the prototype machine can load the machine to 4 kW at 3000 rpm.

Table 6.2 Commercial IM Performance Test Results

P_{in} (W)	P_{out} (W)	Speed (RPM)	I_{rms} (A)	Torque (Nm)	Power Factor	Efficiency (%)
3820	2680	2887	7.45	8.89	0.77	70.03
4260	3000	2871	7.98	10.00	0.78	70.42
4440	3130	2865	8.22	10.53	0.79	70.49
4720	3350	2854	8.56	11.20	0.80	70.97
5170	3670	2836	9.21	12.34	0.81	70.98
5530	3900	2823	9.68	13.18	0.82	70.52
5730	4004	2821	9.97	13.67	0.82	69.98

Table 6.3 Prototyped Motor Performance Test Results

P_{in} (W)	P_{out} (W)	Speed (RPM)	I_{rms} (A)	Torque (Nm)	Power Factor	Efficiency (%)
2342	1860	3000	6.50	6.73	0.51	79.40
2858	2330	3000	7.10	8.23	0.57	81.52
3276	2702	3000	7.68	9.38	0.60	82.43
3824	3174	3000	8.53	10.90	0.63	83.00
4110	3420	3000	9.10	11.49	0.64	83.20
4244	3542	3000	9.30	11.63	0.65	83.46
4396	3680	3000	9.56	11.71	0.67	83.60

Tests are started with the minimum torque possible, i.e., the servo-controlled valve is fully closed and there is no water flowing from the outlet. Then, the valve is gradually opened to let the water flow and load the machine. The IM machine is tested first. For the minimum loading condition, the load torque is recorded as 8.89 Nm at 2887 rpm with 70.03 % efficiency. The IM is loaded up to 13.67 Nm at 2821 rpm and maximum efficiency is recorded as 70.98 %.

The prototype machine testing is started with 6.73 Nm torque at 3000 rpm, 1860 W output power, and the efficiency is recorded as 79.4%. As the loading increased, the efficiency increased gradually and went up to 83.60% at 11.71 Nm, 3680 W output power. Compared to the commercial IM counterpart, the prototyped machine performed better in terms of efficiency over the full operation region. The efficiency improvement varies between 12 to 12.7 points for the same output power levels.

As expected, the LS-SynRM PF was much lower than the IM PF. At the low loading conditions, LS-SynRM PF is recorded as low as 0.51 while the IM PF was 0.77. The highest recorded PF was 0.67 and 0.82 for the LS-SynRM and IM, respectively.

6.5 Conclusions

In this chapter, the experimental prototyping steps, test setup, testing procedure, and the experimental results of the proof-of-concept motor are presented. Additionally, the challenges that are faced during the manufacturing process and the discrepancies between the designed and the prototyped motors are discussed. The prototype is built at the Mutlusu Pumps and Motors factory. The motor is coupled with a water pump through a torque sensor for loading the machine. The experimental results are found to be in good agreement with the FEA results considering the manufacturing effects.

Chapter 7

Conclusions and Future Prospects

7.1 Conclusions

Within the frame of this thesis, systematic design optimization and implementation of a 2 pole, 4 kW, 6 inches diameter LS-SynRM for downhole submersible water pump applications are studied. Around the world, a significant amount of electricity is consumed by various sectors such as agriculture, industrial, household appliances, etc. The demands of energy saving direct the machine designers' attention to finding compact and robust motors with high efficiency, especially in the low and middle power ranges. Motors in this power range are mainly used for industrial, domestic, and irrigation water pumping systems. Addressing the challenges related to asynchronous and LS-PMSM motors, a new hybrid technology called line-start SynRM has evolved. LS-SynRM is a reliable, high-efficiency and low-cost solution compared to high-cost PMSM and low-efficiency asynchronous motors. Each design step of the proposed LS-SynRM is investigated carefully. Working conditions of the LS-SynRM as a down-hole water pump motor are determined and included in the design process. Then, a simulation model is built and performed through an appropriate optimization. Finally, the best candidate is implemented and a test setup for the prototype product is prepared.

The results and conclusions have been presented at the end of each chapter. A summary that belongs to the chapters is provided to show the achievement of this thesis study clearly as follows.

Current problems related to the existing pump systems and research motivations are provided in Chapter 1. Chapter 2 presents a detailed review of existing motor types mainly used as submersible water pump motors. Here, it is observed that LS-SynRM is a strong alternative to the IM and LS-PMSM due to its efficient, low-cost, and rare-earth material-free structure. Before starting the proposed LS-SynRM design steps, the basic working principle of SynRM is explained in Chapter 3. Moreover, the basic insight to calculate the electrical parameters and loss mechanism of the reluctance concept is given. Since designing a motor manually using only a trial-and-error method will not be satisfactory to determine the most optimum design parameters, an appropriate optimization algorithm is also investigated in Chapter 4. Accordingly, it is concluded that the DE algorithm has great potential for solving a wide range of difficult problems and offers better performance in terms of convergence speed and quality of the final Pareto solution set compared to the others. Therefore, it is decided to use the Multi-Objective Differential Evolution (MODE) algorithm at several stages of this study to find the best design for LS-SynRM. A detailed explanation of the MODE is presented in Chapter 4.

The proposed motor design and optimization steps and their simulation results are presented in Chapter 5. In this thesis study, a 2 pole, 4 kW, 6 inches diameter LS-SynRM as a submersible water pump motor is designed and optimized with a new oval shaft structure. Here, it is aimed to improve the machine performance by widening the flux path on the rotor by narrowing down the shaft on the q-axis. Necessary motor design parameters such as the number of flux barriers, stator winding current density, number of turns, and geometric optimization of the rotor are investigated using the MODE and maximum shaft reduction is taken as 5 mm and design with 7 flux barriers gave the best results in terms of efficiency and mass. Here, the efficiency is recorded as 89.240 %, and the motor mass is obtained as 13.35 kg while the shaft size reduction is kept coming as 5 mm. Then, the water damping effect is investigated since the submersible pump motors run inside a fluid-filled environment. Since the water is denser than the air and it causes more loss compared to the windage loss. Analyses are done for three different stator slot opening structures. The results show that the fluid damping effect cannot be assumed as windage loss as in the air-cooled motors in flooded motor structures and cannot be ignored for estimating the machine performance accurately. Moreover, making the stator inner surface as smooth as possible and eliminating the indents reduces the damping loss of the fluid-filled motors significantly. Later, a series of structural analyses are performed to determine the safe maximum shaft dimension limits. After performing the stress, deformation, and vibration analysis it is observed that narrowing down the shaft on the q-axis up to 8 mm is found to be acceptable and safe.

Then, including new findings, the motor optimization was reperformed. The maximum efficiency for the 8 mm narrowed oval shaft design is recorded as 87.06 % with a motor mass of 14.24 kg, and torque ripples between 15.0% and 24.3%. When the proposed LS-SynRM is compared to the same size commercial IM for the same submersible pump motor applications, it not only makes a difference of more than 15 points betterment in efficiency but also challenges the position of IM which exists in the market.

Further, a proper configuration of stator windings with reduced winding MMF space harmonic content which leads to improved machine performance is investigated. It is found that among all the winding structures, the triple-layer winding structure yielded the highest quality results. Considering the manufacturing complexity and cost, the double-layer, version 3 winding configuration that has a similar score to triple-layer winding came forward as a better alternative. The best two designs are selected from among the synchronized candidates' designs one with single layer and another with double layer winding structures. The design with the double layer has 87.54 % and 13.64 kg which is slightly better than the single layer. Considering the very similar performance results of these two designs and manufacturing complexity, the design with the single layer is selected for manufacturing.

The experimental prototyping steps, test setup, testing procedure, and the experimental results of the proof-of-concept motor are presented in Chapter 6. There, the challenges that are faced during the manufacturing process and the discrepancies of the designed and the prototyped motors are discussed. The stator of the machine and final assembly of the machine is completed in Mutlusu Pumps and Motors factory while the rotor parts are manufactured in different facilities. After preparing the test arrangement, the motor is tested at various loading conditions. The prototype motor can go up to 3680 W output power and the efficiency is recorded as 83.6 at this level.

The machine is wound with a reduced size magnet wire as the originally selected cable size did not fit into the slots, when it is attempted, winding isolation was damaged. Hence, the winding resistance increased by about 25% which degraded the machine efficiency. In addition to this, the end winding length becomes slightly larger; hence, increasing the leakage inductance value. Furthermore, all these processes caused the material to change its B-H curve slightly and increase its core losses. Then, stator laminations’ B-H curves are measured and compared to the expected design. It is observed that there is over a 6% discrepancy between the expected and measured results. Hence, all these causes reduced efficiency than desired.

Tests are performed to validate the results. The IM machine is tested first. For the minimum loading condition, the load torque is recorded as 8.89 Nm at 2887 rpm with 70.03 % efficiency. The IM is loaded up to 13.67 Nm at 2821 rpm and maximum efficiency is recorded as 70.98 %. The prototype machine testing started with 6.73 Nm torque at 3000 rpm, 1860 W output power, and the efficiency is recorded as 79.4%. As the loading increased, the efficiency increased gradually and went up to 83.60% at 11.71 Nm, 3680 W output power. Compared to the commercial IM counterpart, the prototyped machine performed better in terms of efficiency over the full operation region. The efficiency improvement varies between 12 to 12.7 points for the same output power levels. As expected, the LS-SynRM PF was much lower than the IM PF. At the low loading conditions, LS-SynRM PF is recorded as low as 0.51 while the IM PF was 0.77. The highest recorded PF was 0.67 and 0.82 for the LS-SynRM and IM, respectively. The experimental results are found to be in good agreement with the FEA results considering the manufacturing effects.

7.2 Societal Impact and Contribution to Global Sustainability

The demands of energy saving direct the machine designers' attention to finding compact and robust motors with high efficiency, especially in the low and middle power ranges. Motors in this power range are mainly used for industrial, domestic, and irrigation water pumping systems.

The primary purpose of this thesis study is to come up with higher efficiency, lower cost, and less permanent magnet-dependent motor solution which will not require an inverter drive besides, it will simply line start. Coming up with a higher efficiency motor will save the country and the world a lot of energy and operating costs. When motor usage becomes widespread around the country and the world this will mean a lot of energy savings as well as less environmental pollution which means a better environmentally friendly motor design. Besides a less costly submersible water pump system will be achieved both in terms of initial costs and in terms of running costs by designing and optimizing an LS-SynRM as a submersible pump motor without windings on rotor design, a line start capability that does not require motor drive and a higher efficiency compared to the conventional IMs. Increasing the efficiency of the pump motor used in industry will improve the overall system performance. Additionally, LS-SynRMs get rid of high cost and rare earth magnet dependency requirements and the degradation of rare earth magnets. Accordingly, it will lower energy consumption, and operating and maintenance costs. As a scientific impact, it is expected that the LS-SynRM will gain more attention as an alternative with higher efficiency, lower manufacturing and operating cost motor for low and middle power range, constant speed applications in related fields of research and accordingly in industry.

All these will result in dramatic nationwide and worldwide cost savings when the designed motor usage becomes widespread. This is a crucial strategy for any facilities management that wants to improve sustainability, productivity, and cost management.

7.3 Future Prospects

This dissertation presented a new oval shaft line start synchronous reluctance machine that is capable of achieving high efficiency with non-rare earth magnets. The research presents a host of different options for future work. They are listed as:

- Material degradation statistical analysis should be done.
- An experimental comparison study in terms of thermal conditions of LS-SynRM and IM can be done.
- Prototype with different types of winding configurations.
- Prototype using ferrite PM to improve the power factor.
- Investigate the parameter sensitivity due to the tolerance of manufacturing on the proposed machine with respect to performance.
- Adapting the prototype machine to several different applications (by designing a new rotor structure based on the application).

BIBLIOGRAPHY

[1] A. T. De Almeida, F. J. T. E. Ferreira, and G. Baoming, “Beyond induction motors - Technology trends to move up efficiency,” *IEEE Trans. Ind. Appl.* 50, 2103–2114 (2014).

[2] K. Tang, L. Zhou, J. Wang, Y. Xiao, and S. Wang, “Rotor design and optimization of the single-phase line-start synchronous reluctance motor,” in *2017 20th Int. Conf. Electr. Mach. Syst.*, (IEEE, 2017).

[3] A. U. Ganesan and L. N. Chokkalingam, “Review on the evolution of technology advancements and applications of line-start synchronous machines,” *IET Electr. Power Appl.* 13, 1–16 (2019).

[4] D. Mingardi and N. Bianchi, “Line-Start PM-Assisted Synchronous Motor Design, Optimization, and Tests,” *IEEE Trans. Ind. Electron.* 64, 9739–9747 (2017).

[5] D. Mingardi, N. Bianchi, and M. D. Pre, “Geometry of Line Start Synchronous Motors Suitable for Various Pole Combinations,” *IEEE Trans. Ind. Appl.* 53, 4360–4367 (2017).

[6] B. Boazzo, A. Vagati, G. Pellegrino, E. Armando, and P. Guglielmi, “Multipolar ferrite-assisted synchronous reluctance machines: A general design approach,” *IEEE Trans. Ind. Electron.* 62, 832–845 (IEEE, 2015).

[7] Mike Pemberton, “Focus on efficiency drives savings in energy consumption,” *Pump Syst. Effic.*, 2012, <https://www.pumpsandsystems.com/topics/pumps/pump-system-efficiency>.

[8] B. Stoffel, “The Role of Pumps for Energy Consumption and Energy Saving,” *Assess. Energy Effic. Pumps Pump Units*, 1–24 (Elsevier, 2015).

[9] T. A. Lipo, *Introduction to AC Machine Design*, Tariq Samad, Ed. (IEEE Press (2017) 193-250).

[10] D. Mingardi and N. Bianchi, “Line-Start PM-Assisted Synchronous Motor Design, Optimization, and Tests,” *IEEE Trans. Ind. Electron.* 64 (2017).

[11] J. J. Lee, S. H. Rhyu, I. S. Jung, and Y. W. Kim, “Design of high efficiency line start permanent magnet motor for submersible pumps,” *EEEIC 2016 - Int. Conf. Environ. Electr. Eng.*, 0–3 (IEEE, 2016).

[12] J. Li, J. Song, and Y. Cho, “High performance line start permanent magnet synchronous motor for pumping system,” *IEEE Int. Symp. Ind. Electron.*, 1308–1313 (IEEE, 2010).

[13] W. Lyskawinski, C. Jedryczka, and W. Szelag, “Influence of magnet and cage shape on properties of the line start synchronous motor with powder hybrid rotor,” *2017 Int. Symp. Electr. Mach. SME 2017*, 1–6 (IEEE, 2017).

[14] A. Takahashi, S. Kikuchi, H. Mikami, K. Ide, and A. Binder, “Reluctance torque utility for line-starting permanent magnet motors,” *IEEE Trans. Energy Convers.* 28, 805–814 (IEEE, 2013).

[15] R. T. Ugale and B. N. Chaudhari, “A new rotor structure for line start permanent magnet synchronous motor,” *Proc. 2013 IEEE Int. Electr. Mach. Drives Conf. IEMDC 2013*, 1436–1442 (IEEE, 2013).

[16] R. T. Ugale, B. N. Chaudhari, S. Baka, S. S. Dambhare, and A. Pramanik, “Induced pole rotor structure for line start permanent magnet synchronous motors,” *IET Electr. Power Appl.* 8, 131–140 (2014).

[17] S. Shamlou and M. Mirsalim, “Design, optimisation, analysis and experimental verification of a new line-start permanent magnet synchronous shaded-pole

motor," *IET Electr. Power Appl.* 7, 16–26 (2013).

[18] W. N. Fu and Y. Chen, "A Post-Assembly Magnetization Method for a Line-Start Permanent-Magnet Motor," *IEEE Trans. Appl. Supercond.* 26, 11–14 (2016).

[19] M. A. Rahman, A. M. Osheiba, K. Kurihara, M. A. Jabbar, H. W. Ping, K. Wang, and H. M. Zubayer, "Advances on single-phase line-start high efficiency interior permanent magnet motors," *IEEE Trans. Ind. Electron.* 59, 1333–1345 (IEEE, 2012).

[20] M. N. Azari and M. Mirsalim, "Line-start permanent-magnet motor synchronisation capability improvement using slotted solid rotor," *IET Electr. Power Appl.* 7, 462–469 (2013).

[21] M. J. Melfi, S. D. Umans, and J. E. Atem, "Viability of highly efficient multi-horsepower line-start permanent-magnet motors," *IEEE Trans. Ind. Appl.* 51, 120–128 (IEEE, 2015).

[22] J. J. Lee, Y. K. Kim, S. H. Rhyu, and I. S. Jung, "Magnet shape design of 3-phase line-start permanent magnet motor for high efficiency," *2013 Int. Conf. Electr. Mach. Syst. ICEMS 2013*, 125–128 (2013).

[23] H. Saikusa, S. Arikawa, T. Higuchi, Y. Yokoi, and T. Abe, "Efficiency improvement of a self-start type permanent magnet synchronous motor," *2014 Int. Power Electron. Conf. IPEC-Hiroshima - ECCE Asia 2014*, 3007–3011 (IEEE, 2014).

[24] A. Mahmoudi, S. Kahourzade, N. A. Rahim, and W. P. Hew, "Design, Analysis, and Prototyping of an Axial-Flux Permanent Magnet Motor Based on Genetic Algorithm and Finite-Element Analysis," *IEEE Trans. Magn.* 49, 1479–1492 (IEEE, 2013).

[25] M. Tian, X. Wang, D. Wang, W. Zhao, and C. Li, "A Novel Line-Start Permanent Magnet Synchronous Motor with 6/8 Pole Changing Stator Winding," *IEEE Trans. Energy Convers.* 33, 1064–1074 (IEEE, 2018).

[26] B. Yan, X. Wang, and Y. Yang, "Starting performance improvement of line-start permanent-magnet synchronous motor using composite solid rotor," *IEEE Trans. Magn.* 54, 2018–2021 (IEEE, 2018).

[27] B. Yan, X. Wang, and Y. Yang, "Comparative Parameters Investigation of Composite Solid Rotor Applied to Line-Start Permanent-Magnet Synchronous Motors," *IEEE Trans. Magn.* 54, 2–6 (IEEE, 2018).

[28] R. T. Ugale and B. N. Chaudhari, "Rotor Configurations for Improved Starting and Synchronous Performance of Line Start Permanent-Magnet Synchronous Motor," *IEEE Trans. Ind. Electron.* 64, 138–148 (IEEE, 2017).

[29] M. Gwozdziewicz and J. Zawilak, "Induced pole permanent magnet synchronous motor," *2017 Int. Symp. Electr. Mach. SME 2017*, 45–48 (IEEE, 2017).

[30] B. H. Lee, J. W. Jung, and J. P. Hong, "An improved analysis method of irreversible demagnetization for a single-phase line-start permanent magnet motor," *IEEE Trans. Magn.* 54 (IEEE, 2018).

[31] A. Alidousti, A. Sadoughi, H. Behbahanifard, and Y. Raeisi, "A new rotor prototype for single phase line start permanent magnet synchronous motor based on amendments to a small industrial shaded pole induction motor," *9th Annu. Int. Power Electron. Drive Syst. Technol. Conf. PEDSTC 2018* 2018-Janua, 218–223 (IEEE, 2018).

[32] J. K. Kostko, "Polyphase reaction synchronous motors," *J. Am. Inst. Electr. Eng.* 42, 1162–1168 (The American Institute of Electrical Engineers, 1923).

[33] C. E. G. Martins, P. Kuo-Peng, and N. Sadowski, "Design of synchronous reluctance motors with flux barriers using 2D-FEM," *IEMDC 2003 - IEEE Int.*

Electr. Mach. Drives Conf. 3, 1669–1674 (2003).

[34] H. Nam, S. B. Park, G. H. Kang, J. P. Hong, J. B. Eom, and T. U. Jung, "Design to improve starting performance of line-start synchronous reluctance motor for household appliances," *Conf. Rec. - IAS Annu. Meet. (IEEE Ind. Appl. Soc.* 1, 79–85 (IEEE, 2004).

[35] T. U. Jung, C. H. Yun, H. R. Cha, H. M. Kim, H. Nam, and J. P. Hong, "The rotor conductor design for starting stability of line-start synchronous reluctance motor," *IECON Proc. (Industrial Electron. Conf.*, 1107–1112 (2006).

[36] A. Kersten, Y. Liu, D. Pehrman, and T. Thiringer, "Rotor design of line-start synchronous reluctance machine with round bars," *IEEE Trans. Ind. Appl.* 55, 3685–3696 (IEEE, 2019).

[37] Y. Hu, B. Chen, Y. Xiao, J. Shi, and L. Li, "Study on the Influence of Design and Optimization of Rotor Bars on Parameters of a Line-Start Synchronous Reluctance Motor," *IEEE Trans. Ind. Appl.* 56, 1368–1376 (IEEE, 2020).

[38] S. Baka, S. Sashidhar, and B. G. Fernandes, "Multi-barrier two-pole line-start synchronous reluctance motor with high saliency for a bore-well submersible pump," *Proc. IEEE Int. Conf. Ind. Technol.* 2018-Febru, 475–480 (IEEE, 2018).

[39] M. Villani, M. Santececca, and F. Parasiliti, "High-Efficiency Line-Start Synchronous Reluctance Motor for Fan and Pump Applications," *Proc. - 2018 23rd Int. Conf. Electr. Mach. ICEM 2018,* 2178–2184 (IEEE, 2018).

[40] S. Baka, S. Sashidhar, and B. G. Fernandes, "Design and Optimization of a Two-Pole Line-Start Ferrite Assisted Synchronous Reluctance Motor," *Proc. - 2018 23rd Int. Conf. Electr. Mach. ICEM 2018,* 131–137 (IEEE, 2018).

[41] Y. Hu, Y. Xiao, B. Chen, and J. Shi, "Effect of Direction and Shape of Rotor Conductor Bars on Parameters of Line-Start Synchronous Reluctance Motor," *ICEMS 2018 - 2018 21st Int. Conf. Electr. Mach. Syst.*, 634–639 (KIEE EMECS (KIEE Electrical Machinery and Energy Conversion Systems), 2018).

[42] A. J. Sorgdrager and R. Wang, "Design and optimisation of a line-start synchronous reluctance motor" (2016).

[43] J. Tampio, T. Kansakangas, S. Suuriniemi, J. Kolehmainen, L. Kettunen, and J. Ikaheimo, "Analysis of Direct-On-Line Synchronous Reluctance Machine Start-Up Using a Magnetic Field Decomposition," *IEEE Trans. Ind. Appl.* 53, 1852–1859 (IEEE, 2017).

[44] H. C. Liu, H. S. Hong, S. Cho, J. Lee, and C. S. Jin, "Bubbles and Blisters Impact on Diecasting Cage to the Designs and Operations of Line-Start Synchronous Reluctance Motors," *IEEE Trans. Magn.* 53, 2–5 (IEEE, 2017).

[45] H. C. Liu and J. Lee, "Optimum Design of an IE4 Line-Start Synchronous Reluctance Motor Considering Manufacturing Process Loss Effect," *IEEE Trans. Ind. Electron.* 65, 3104–3114 (2018).

[46] M. Gamba, G. Pellegrino, A. Vagati, and F. Villata, "Design of a line-start synchronous reluctance motor," in *2013 Int. Electr. Mach. Drives Conf.,* (IEEE, 2013).

[47] M. Gamba, E. Armando, G. Pellegrino, A. Vagati, B. Janjic, and J. Schaab, "Line-start synchronous reluctance motors: Design guidelines and testing via active inertia emulation," *2015 IEEE Energy Convers. Congr. Expo. ECCE 2015,* 4820–4827 (IEEE, 2015).

[48] S. T. Boroujeni, M. Haghparast, and N. Bianchi, "Optimization of flux barriers of line-start synchronous reluctance motors for transient- and steady-state operation," *Electr. Power Components Syst.* 43, 594–606 (2015).

[49] G. Electric, "Synchronization of Line-Start Permanent-Magnet AC Motors

Analysis of the Magnetic Field in Rotating Armature Electronically Commutated DC Machines by Finite Elements," 57–58 (1984).

[50] S. T. Boroujeni, N. Bianchi, and L. Alberti, "Fast estimation of line-start reluctance machine parameters by finite element analysis," *IEEE Trans. Energy Convers.* 26, 1–8 (2011).

[51] J. L. Yeswanth, G. A. Uvaraj, and N. C. Lenin, "A novel line start synchronous reluctance motor," *2015 IEEE Int. Magn. Conf. INTERMAG 2015,* 2020 (IEEE, 2015).

[52] Z. Gmyrek, M. Lefik, A. Cavagnino, and L. Ferraris, "Comparison of the fractional power LSSR motor with cores made of various magnetic materials," *2017 18th Int. Symp. Electromagn. Fields Mechatronics, Electr. Electron. Eng. ISEF 2017,* 2–3 (2017).

[53] K. Smolka and Z. Gmyrek, "Dynamics of the line-start reluctance motor with SMC rotor," *2017 18th Int. Symp. Electromagn. Fields Mechatronics, Electr. Electron. Eng. ISEF 2017* (2017).

[54] H. Parveen, U. Sharma, B. Singh, M. Modi, D. Dudharejiya, and C. Jain, "Conversion of Motor Technology for Economical Solar PV fed Water Pumping System; Conversion of Motor Technology for Economical Solar PV fed Water Pumping System," *2020 Int. Conf. Power, Instrumentation, Control Comput.* (2020).

[55] S. Baka, S. Sashidhar, and B. G. Fernandes, "Design of an Energy Efficient Line-Start Two-Pole Ferrite Assisted Synchronous Reluctance Motor for Water Pumps; Design of an Energy Efficient Line-Start Two-Pole Ferrite Assisted Synchronous Reluctance Motor for Water Pumps," *IEEE Trans. Energy Convers.* 36 (2021).

[56] M. Ruba, F. Jurca, L. Czumbil, D. D. Micu, C. Martis, A. Polycarpou, and R. Rizzo, "Synchronous reluctance machine geometry optimisation through a genetic algorithm based technique," *IET Electr. Power Appl.* 12, 431–438 (The Institution of Engineering and Technology, 2018).

[57] A. Credo, G. Fabri, M. Villani, and M. Popescu, "High speed synchronous reluctance motors for electric vehicles: A focus on rotor mechanical design," *2019 IEEE Int. Electr. Mach. Drives Conf. IEMDC 2019,* 165–171 (Institute of Electrical and Electronics Engineers Inc., 2019).

[58] E. Howard, M. J. Kamper, and S. Gerber, "Asymmetric Flux Barrier and Skew Design Optimization of Reluctance Synchronous Machines," *IEEE Trans. Ind. Appl.* 51, 3751–3760 (Institute of Electrical and Electronics Engineers Inc., 2015).

[59] M. Di Nardo, G. Lo Calzo, M. Galea, and C. Gerada, "Design Optimization of a High-Speed Synchronous Reluctance Machine," *IEEE Trans. Ind. Appl.* 54, 233–243 (Institute of Electrical and Electronics Engineers Inc., 2018).

[60] C. Babetto, G. Bacco, and N. Bianchi, "Synchronous Reluctance Machine Optimization for High-Speed Applications," *IEEE Trans. Energy Convers.* 33, 1266–1273 (Institute of Electrical and Electronics Engineers Inc., 2018).

[61] K. Chen, W. Yu, and C. Wen, "Rotor optimization for synchronous reluctance motors," *CES Trans. Electr. Mach. Syst.* 3, 279–284 (Electrical Engineering Press Co. Ltd., 2019).

[62] J. Zhang, H. Wang, L. Chen, C. Tan, and Y. Wang, "Multi-objective optimal design of bearingless switched reluctance motor based on multi-objective genetic particle swarm optimizer," *IEEE Trans. Magn.* 54 (IEEE, 2018).

[63] R. Benlamine, F. Dubas, S. A. Randi, D. Lhotellier, and C. Espanet, "Design by optimization of an axial-flux permanent-magnet synchronous motor using genetic algorithms," *2013 Int. Conf. Electr. Mach. Syst. ICEMS 2013*, 13–17 (2013).

[64] N. Bianchi and S. Bolognani, “Design optimisation of electric motors by genetic algorithms,” *IEE Proc. - Electr. Power Appl.* 145, 475 (1998).

[65] Z. Michalewicz and M. Schoenauer, “Evolutionary Algorithms for Constrained Parameter Optimization Problems,” *Evol. Comput.* 4, 1–32 (1996).

[66] R. Storn and K. Price, “Differential Evolution - A simple and Efficient Adaptive Scheme for Global Optimization over Continuous Spaces,” *Tech. Rep. TR-95-012, Int. Comput. Sci. Berkeley, Calif.*, 1–12 (1995).

[67] S. Zhang, S. Li, R. G. Harley, and T. G. Habetler, “Performance Evaluation and Comparison of Multi-Objective Optimization Algorithms for the Analytical Design of Switched Reluctance Machines,” *CES Trans. Electr. Mach. Syst.* 1, 58–65 (2017).

[68] R. R. Moghaddam, *Synchronous Reluctance Machine (SynRM) in Variable Speed Drives (VSD) Applications* (2011).

[69] J. F. Gieras, *Permanent magnet motor technology: design and applications* (2009).

[70] B. Tekgun, “Analysis, Measurement and Estimation of the Core Losses in Electrical Machines” (2016).

[71] B. Tekgun, Y. Sozer, and I. Tsukerman, “Core Loss in Electric Machines,” 175–210 (2020).

[72] B. Sarlioglu, “Understanding Electric Motors and Loss Mechanisms Wisconsin Electric Machines and Power Electronics Consortium.”

[73] J. E. Vrancik, “Prediction of windage power loss in alternators - NASA Technical Reports Server (NTRS),” Cleveland, Ohio, 1968.

[74] R. Storn and K. Price, “Differential Evolution - A simple evolution strategy for fast optimization,” *Dr. Dobb’s J.* 22, 18–24 (1997).

[75] X. D. Xue, K. W. E. Cheng, T. W. Ng, and N. C. Cheung, “Multi-Objective Optimization Design of In-Wheel Switched Reluctance Motors in Electric Vehicles,” *IEEE Trans. Ind. Electron.* 57, 2980–2987 (2010).

[76] P. Zhang, G. Y. Sizov, D. M. Ionel, and N. A. O. Demerdash, “Design Optimization of Spoke-Type Ferrite Magnet Machines by Combined Design of Experiments and Differential Evolution Algorithms,” *2013 Int. Electr. Mach. Drives Conf.*, 892–898 (IEEE, 2013).

[77] J. Lampinen, “A constraint handling approach for the differential evolution algorithm,” in *Proc. 2002 Congr. Evol. Comput. CEC’02 (Cat. No.02TH8600)* 2, (IEEE, 2002).

[78] R. Storn, “Differential Evolution – A Simple and Efficient Heuristic for Global Optimization over Continuous Spaces,” *J. Glob. Optim.* 76, 341–359 (1997).

[79] D. Tekgun, B. Tekgun, and I. Alan, “FEA based fast topology optimization method for switched reluctance machines,” *Electr. Eng.*, 1–11 (Springer Science and Business Media Deutschland GmbH, 2022).

[80] “Hendershot J.R. Jr., Miller T.J.E. - Design of Brushless Permanent-Magnet Motors.”

[81] D. Tekgun, M. Muhsin Cosdu, B. Tekgun, and I. Alan, “Effect of the Stator Slot Indents on Fluid Damping Loss in Submersible Pump Applications; Effect of the Stator Slot Indents on Fluid Damping Loss in Submersible Pump Applications,” *2022 4th Glob. Power, Energy Commun. Conf.* (2022).

[82] D. Tekgun and I. Alan, “A new oval shaft, high performance, 2 pole line start synchronous reluctance machine for submersible pump applications,” *Int. J. Appl. Electromagn. Mech.* 70.1, 73-93, (IOS Press, 2022).

[83] A. Kersten, S. Member, Y. Liu, S. Member, D. Pehrman, and T. Thiringer, “Rotor Design of Line-Start Synchronous Reluctance Machine With Round Bars,” *IEEE*

Trans. Ind. Appl. 55, 3685.

[84] Anup Kumar Dey, “What Is Modal Analysis and Why Is It Necessary? (With PDF) – What Is Piping,” <https://whatispiping.com/modal-analysis/> (29 December 2022).

[85] E. C. Lovelace, T. M. Jahns, T. A. Keim, and J. H. Lang, “Mechanical design considerations for conventionally laminated, high-speed, interior PM synchronous machine rotors,” *IEEE Trans. Ind. Appl.* 40, 806–812 (2004).

[86] D. Tekgun, M. Muhsin Cosdu, B. Tekgun, and I. Alan, “Investigation of the Effects of Multi-Layer Winding Structures in Two Pole Synchronous Reluctance Machines,” *Proc. - 2021 IEEE 3rd Glob. Power, Energy Commun. Conf. GPECOM 2021*, 120–125 (Institute of Electrical and Electronics Engineers Inc., 2021).

[87] K. Kurihara, G. Wakui, and T. Kubota, “Steady-State Performance Analysis of Permanent I ",” *IEEE Trans. Magn.* 30, 1306–1315 (1994).

[88] G. Dajaku, W. Xie, and D. Gerling, “Reduction of low space harmonics for the fractional slot concentrated windings using a novel stator design,” *IEEE Trans. Magn.* 50 (IEEE, 2014).

[89] G. Dajaku, S. Spas, and D. Gerling, “Advanced optimization methods for fractional slot concentrated windings,” *Electr. Eng.* 101, 103–120 (Springer Berlin Heidelberg, 2019).

[90] D. A. Kocabas, “Novel winding and core design for maximum reduction of harmonic magnetomotive force in AC motors,” *IEEE Trans. Magn.* 45, 735–746 (2009).

[91] T. Gundogdu and G. Komurgoz, “Investigation of winding MMF harmonic reduction methods in IPM machines equipped with FSCWs,” *Int. Trans. Electr. Energy Syst.* 29, 1–27 (2019).

[92] I. Petrov, P. Ponomarev, Y. Alexandrova, and J. Pyrhonen, “Unequal Teeth Widths for Torque Ripple Reduction in Permanent Magnet Synchronous Machines With Fractional-Slot Non-Overlapping Windings,” *IEEE Trans. Magn.* 51 (2015).

[93] A. M. EL-Refaie, “Fractional-slot concentrated-windings synchronous permanent magnet machines: Opportunities and challenges,” *IEEE Trans. Ind. Electron.* 57, 107–121 (IEEE, 2010).

[94] T. Hamiti, T. Lubin, L. Baghli, and A. Rezzoug, “Modeling of a synchronous reluctance machine accounting for space harmonics in view of torque ripple minimization,” *Math. Comput. Simul.* 81, 354–366 (International Association for Mathematics and Computers in Simulation (IMACS), 2010).

[95] G. Dajaku and D. Gerling, “Different novel methods for reduction of low space harmonics for the fractional slot concentrated windings,” *ICEMS 2012 - Proc. 15th Int. Conf. Electr. Mach. Syst.* (IEEE, 2012).

[96] M. V. Cistelecan, F. J. T. E. Ferreira, and M. Popescu, “Three phase tooth-concentrated multiple-layer fractional windings with low space harmonic content,” *2010 IEEE Energy Convers. Congr. Expo. ECCE 2010 - Proc.*, 1399–1405 (IEEE, 2010).

[97] A. S. Abdel-Khalik, S. Ahmed, and A. M. Massoud, “Low space harmonics cancelation in double-layer fractional slot winding using dual multiphase winding,” *IEEE Trans. Magn.* 51 (Institute of Electrical and Electronics Engineers Inc., 2015).

[98] A. Tessarolo, M. Mezzarobba, and N. Barbini, “Improved four-layer winding design for a 12-slot 10-pole permanent magnet machine using unequal tooth coils,” *IECON Proc. (Industrial Electron. Conf.*, 1686–1691 (IEEE Computer Society,

2016).
[99] N. Bekka, M. E. H. Zaim, N. Bernard, and D. Trichet, “A Novel Methodology for Optimal Design of Fractional Slot with Concentrated Windings,” *IEEE Trans. Energy Convers.* 31, 1153–1160 (Institute of Electrical and Electronics Engineers Inc., 2016).
[100] B. Tekgun, D. Tekgun, I. Alan, and M. Badawy, “Design and Control of a Single Phase DC/Rectified AC/AC Inverter for low THD Applications,” *7th Int. IEEE Conf. Renew. Energy Res. Appl. ICRERA 2018*, 424–430 (Institute of Electrical and Electronics Engineers Inc., 2018).
[101] A. Tessarolo, “A Quadratic-Programming Approach to the Design Optimization of Fractional-Slot Concentrated Windings for Surface Permanent-Magnet Machines,” *IEEE Trans. Energy Convers.* 33, 442–452 (Institute of Electrical and Electronics Engineers Inc., 2018).
[102] C. M. Spargo, B. C. Mecrow, and J. D. Widmer, “Application of fractional slot concentrated windings to synchronous reluctance machines,” *Proc. 2013 IEEE Int. Electr. Mach. Drives Conf. IEMDC 2013*, 618–625 (IEEE, 2013).
[103] M. Gamba, G. Pellegrino, and A. Vagati, “A new PM-assisted synchronous reluctance machine with a nonconventional fractional slot per pole combination,” *J. Electr. Eng.* 15, 97–104 (IEEE, 2015).
[104] A. Vagati, M. Pastorelli, G. Franceschini, and S. C. Petrache, “Design of low-torque-ripple synchronous reluctance motors,” *IEEE Trans. Ind. Appl.* 34, 758–765 (1998).
[105] G. Dajaku and D. Gerling, “A Novel 24-Slots/10-Poles Winding Topology for Electric Machines,” *2011 IEEE Int. Electr. Mach. Drives Conf. IEMDC 2011*, 65–70 (IEEE, 2011).
[106] M. A. Kabir and I. Husain, “New multilayer winding configuration for distributed MMF in AC machines with shorter end-turn length,” *IEEE Power Energy Soc. Gen. Meet.* 2016-Novem, 0–4 (IEEE, 2016).
[107] M. A. Kabir and I. Husain, “Application of a Multilayer AC Winding to Design Synchronous Reluctance Motors,” *IEEE Trans. Ind. Appl.* 54, 5941–5953 (2018).
[108] J. Pyrhönen, T. Jokinen, and V. Hrabovcová, *Design of Rotating Electrical Machines*, in *Des. Rotating Electr. Mach.* (2008).
[109] T. Burak and I. Tsukerman, “Measurement of Core Losses in Electrical Steel in the Saturation Region under DC Bias Conditions,” *IEEE Trans. Ind. Appl.* 53 (2017).
[110] A. Credo, G. Fabri, M. Villani, and M. Popescu, “A Robust Design Methodology for Synchronous Reluctance Motors,” *IEEE Trans. Energy Convers.* 35, 2095–2105 (Institute of Electrical and Electronics Engineers Inc., 2020).

CURRICULUM VITAE

2008 – 2012	B.Sc., Electrical - Electronics Engineering, Inonu University, Malatya, TÜRKİYE
2014 – 2017	M.Sc., Electrical Engineering, University of Akron, Akron, Ohio, USA
2017 – 2022	Ph.D., Electrical and Computer Engineering, Abdullah Gül University, Kayseri, TÜRKİYE
2017 – 2022	Research Assistant, Electrical - Electronics Engineering, Abdullah Gül University, Kayseri, TÜRKİYE

SELECTED PUBLICATIONS AND PRESENTATION

J1) D. Tekgun and I. Alan, A New Oval Shaft, High Performance, 2 Pole Line Start Synchronous Reluctance Machine for Submersible Pump Applications, published in International Journal of Applied Electromagnetics and Mechanics (June 2022).

J2) D. Tekgun, B. Tekgun & I. Alan, FEA based fast topology optimization method for switched reluctance machines, published in Springer Electrical Engineering (Jan. 2022).

J3) D. Tekgun, W. Uddin, Y. Sozer, K. S. Lee, Real Time High Frequency Impedance Monitoring of Human Skin Through Magnetic Coupling, published in IEEE Sensors Journal (Aug. 2017).

C1) D. Tekgun, M. M. Cosdu, B. Tekgun and I. Alan, Effect of the Stator Slot Indents on Fluid Damping Loss in Submersible Pump Applications, in 2022 4th Global Power, Energy and Communication Conference (GPECOM) (June 2022).

C2) D. Tekgun, M. Muhsin Cosdu, B. Tekgun and I. Alan, Investigation of the Effects of Multi-Layer Winding Structures in Two Pole Synchronous Reluctance Machines, in 2021 3rd Global Power, Energy and Communication Conference (GPECOM) (Oct. 2021).

C3) D. Tekgun, B. Tekgun and I. Alan, A Modular Three-Phase Buck-Boost Motor Drive Topology, in 2020 6th International Conference on Electric Power and Energy Conversion Systems (EPECS), (Oct. 2020).

C4) B. Tekgun, D. Tekgun, I. Alan and M. Badawy, Design and Control of a Single Phase DC/Rectified AC/AC Inverter for low THD Applications, in 2018 7th International Conference on Renewable Energy Research and Applications (ICRERA), (Dec. 2018).

C5) Y. Yasa, D. Tekgun, Y. Sozer, J. Kutz, J. Tylenda, Effect of Distributed Airgap in the Stator for Acoustic Noise Reduction in Switched Reluctance Motors, in IEEE Applied Power Electronics Conference, Tampa, FL (March 2017).